(67)

Surge Dynamics of a Helicopter Engine Gas Generator

by

Brian A. Corn

B.S. Aerospace Engineering
Virginia Polytechnic Institute and State University, 1994

Submitted to the Department of Aeronautics and Astronautics
in Partial Fulfillment of the Requirements for the Degree of

Master of Science in Aeronautics and Astronautics

at the

Massachusetts Institute of Technology
February 1998

Signature of Author_____
Department of Aeronautics and Astronautics
February 9, 1998

Certified by_____
Professor Alan H. Epstein
R. C. MacLaurin Professor of Aeronautics and Astronautics
Thesis Supervisor

Accepted by_____
Professor Jaime Peraire
Associate Professor of Aeronautics and Astronautics
Chair, Graduate Office

Surge Dynamics of a Helicopter Engine Gas Generator

by

Brian A. Corn

Submitted to the Department of Aeronautics and Astronautics
on February 9, 1998, in Partial Fulfillment of the
Requirements for the Degree of Master of Science in
Aeronautics and Astronautics

Abstract

The surge dynamics of an AlliedSignal LTS-101 gas producer were examined experimentally. Tests were performed on the standard producer configuration and with modifications for control implementation. Diffuser throat air injection was employed as an actuator, and the modified system dynamics were investigated with a mean level of injection. Steady injection stabilized the system (in the sense of surge) to lower turbine corrected flow and created a large, surge-free region of near zero characteristic slope at the speedline peak. This region also included operating points with slightly positive compressor characteristic slope.

Low levels of unsteadiness below 100 Hz were observed prior to surge in the standard configuration. The system including injection exhibited prominent 27 Hz mild surge and 68 Hz modal behavior with spectral power levels an order of magnitude greater than the unsteadiness without injection. The modes were 1-D, with no evidence of rotating stall present. Growth and decay of these peaks occurred in a random fashion, but their average magnitude increased as the gas producer was throttled. Steady growth into deep surge was not observed, but unsteady mass flow estimates indicated that large displacement mild surge oscillations preceded the event. Using a non-linear system simulation with empirically determined speedlines, the existence of this dynamic instability was attributed to positive compressor characteristic slope found in the mean injection case. A linear, lumped-parameter model attributed the 68 Hz mode to influence of the injection plenum on the system dynamics.

Near surge, open-loop, forced-response experiments were conducted to determine sinusoidal transfer functions of injection command signals to engine pressures. An estimate of the pole and zero locations, suitable for control law design, was formulated for the inlet static pressure taps. Preliminary closed-loop experiments were executed with four linear control laws. Although no significant stability enhancement was realized, actuator power was sufficient to modify the damping and frequencies of the modal behavior. The identification of the observed modes' physical mechanisms and the closed-loop results suggest future control activity be limited to the 27 and 68 Hz modes.

Thesis Supervisor: Alan H. Epstein
Title: R. C. MacLaurin Professor of Aeronautics and Astronautics

Acknowledgments

The opportunity to study with the outstanding faculty and students at the Massachusetts Institute of Technology has been a very enlightening, if at times quite humbling, experience. I would like to thank the many individuals at the Gas Turbine Laboratory who have contributed to the completion of my research and to making my time in Cambridge enjoyable.

I am deeply indebted to Professor Alan Epstein, my thesis supervisor, for the opportunity to "bang my head against the wall" on some of the finest experimental facilities in academia. His wealth of experimental knowledge and advice contributed to the progress of this project. I also appreciate his flexibility with the conditions under which this thesis was completed. I express my sincere gratitude to Professor James D. Paduano for his patience and advice on controls topics. I also acknowledge the assistance of Dr. Gerald Guenette and Professor Edward Greitzer for advice on computer and fluid dynamic topics, respectively.

Few experimental projects at the Gas Turbine Laboratory would ever get off the ground without the assistance of the exceptional technical staff. Thanks goes out to Victor Dubrowski, James Letendre, Bill Ames, and Mariano Hellwig for not only project assistance but taking the time to teach, augmenting academia with doses of practicality.

I wish to thank the administrative and support staff for their behind the scenes work, including Holly Anderson and Diana Park. A special thanks to Lori Martinez for single-handedly wiping out the scourge of graduate student starvation. Outside of the GTL, I must thank Elizabeth Zotos. Her assistance in the administration of my funding, especially under the unusual circumstances of my thesis completion, is greatly appreciated.

The single greatest asset of the Gas Turbine Laboratory is the synergistic, team atmosphere among the students. Technical interaction with the high caliber of students in the GTL accounts for a large percentage of my education at MIT. I would first like to thank the members of the helicopter engine crew. The partnerships with Fouzi Al-Essa and Dr. Laurence Didearjean proved invaluable in both running the engine and interrogating the data. I hope I was able to help them in an equitable fashion. I appreciate the assistance of Jinwoo Bae and Eric Nelson, and I wish them the best of luck in completing their engine research. Control theory assistance from Dr. Harold Weigl was also greatly appreciated. I would like to thank the balance of the Smart Engines research group for their advice on a variety of technical matters. More important than technical advice, it was the friendships which made it all bearable. I would like to thank two students in particular: John Brookfield and Greg Stanislaw.

Before this becomes the longest chapter in this thesis, I would like to conclude by thanking my family. As I get older, I realize how much I appreciate the counsel, support, and love of my parents. Thanks, Mom and Dad.

This research was completed with funding from the National Science Foundation Graduate Research Fellowship Program and the Air Force Office of Scientific Research. The author would also like to recognize the assistance of the AlliedSignal Corporation for donating the personnel and time necessary for engine assembly and maintenance.

Table of Contents

List of Figures

Chapter 1

Chapter 2

Chapter 3

Chapter 4

Appendix A

Appendix B

List of Tables

Chapter 2

Chapter 3

Chapter 4

Appendix B

Nomenclature

Symbols:

a	Speed of Sound
A	Area
A	Jacobian Matrix in State Space Formulation
B	Professor Edward Greitzer's Non-Dimensional Stability Parameter
B	State Space Matrix
C	State Space Matrix
C_d	Coefficient of Discharge
D	State Space Matrix
f	Frequency
f( )	Function
G(jω)	Plant Sinusoidal Transfer Function
G(s)	Laplace Domain Plant Transfer Function
G(ω)	Transfer Function Estimate
H(s)	Laplace Domain Compensator Transfer Function
I_1	Inertia Ratio
jω	Complex Frequency
K	Control Law Gain
L	Length
m or $\dot{m}$	Mass Flow
M	Mach Number
N_1	Gas Generator Rotor Speed
N(jω)	Noise, Frequency Domain

p	Pressure
PR	Pressure Ratio
PSD	Power Spectral Density
R	Gas Constant
s	Laplace variable
S_{uu}	Power Spectral Density of U
S_{uy}	Cross-Spectral Density of U and Y
t	Time
U	Flow Velocity
U_t	Rotor Tip Speed
$U(j\omega)$	Command, Frequency Domain
v	Fluidic Velocity in Appendix A
V	Volume
x	Axial location in Appendix A
$Y(j\omega)$	Output, Frequency Domain
β	Non-Dimensionalized Stability Parameter (similar to B)
δ	$P_{t,amb}/P_{std}$
Δ	Change in Quantity
γ	Ratio of Specific Heats
$\gamma(j\omega)$	Coherence Function
π	Total Pressure Ratio
ρ	Density
σ	Standard Deviation
θ	$T_{t,amb}/T_{std}$
ω_H	Helmholtz Resonator Frequency

ζ	Damping Ratio

Subscripts:

amb	Ambient Condition
b	Combustor Station
c	Compressor (Compressor Face Station in Appendix A)
corr	Corrected Parameter
d	Downstream
dep	Depression (of Static Pressure)
des	Design Value
filt	Filtered
fp	Injection Feed Plenum Station
fs	Free Stream
imp	Impeller
inl	Inlet
inj	Injection Parameter
noise	Perturbation Noise
ref	Referred (In reference to mass flow corrected to sea level inlet conditions)
s	Static
std	Standard Conditions
t	Total
th	Throat Station
turb	Turbine
u	Upstream
valve	Valve Output

vd	Vaned Diffuser
1	Bellmouth Inlet Station
2	Compressor Inlet Station (Pressure Tap Station in Appendix A)
3	Compressor Exit Station
4	Turbine NGV Inlet Station
41	Turbine Rotor Inlet Station
5	Nozzle Inlet Station

Superscripts and Other:

$*$	Non-Dimensionalized
$\dot{x}$	Time Derivative of x
$\overline{x}$	Mean or Background Value of x
$\tilde{x}$	Perturbation Value of x

Chapter 1: Introduction

1.1 Background

The useful operating range of gas turbines is limited by the onset of surge and rotating stall instabilities. Surge is a 1-D (full annulus) fluctuation in pressure and mass flow through a compression system. The term is usually associated with extremely violent oscillations characterized by periods of reverse flow. Fluctuations occurring without flow reversal are labeled "mild" surge. The consequences of this phenomena in aircraft engines range from costly unscheduled inspections to loss of airframes. Rotating stall, on the other hand, is characterized by 2-D (circumferential) variations in compressor flow which travel around the annulus at a characteristic speed. Some compressors may operate in rotating stall, but the diminished pressure rise generally yields unacceptable performance. In many compressors, particularly axial machines, rotating stall develops into the more serious surge event.

A compressor operating map (see Figure 1.1) is divided into stable and unstable operating regimes by the surge line. Points to the left of the surge line are unstable. A gas generator's equilibrium operating line is the locus of steady-state operating points established by the matching (mass flow, rotational speeds, and work) of the compressor, turbine, and other downstream components. The placement of this line and the engine's control inputs (fuel and variable geometry scheduling) must prevent the operating point from crossing into an unstable region, even during transients. The proximity of an operating point to the surge line is expressed as surge margin. A simplistic definition of surge margin for the case of constant inlet corrected flow is the difference between the pressure ratios at a stable point and the surge line expressed as a percentage of the stable point's pressure ratio [1]. When peak compressor adiabatic efficiency is found in regions near the surge line and Brayton cycle efficiency increases with pressure ratio, this measure of safety margin also indicates the magnitude of performance penalty exacted by the open-loop stability requirement.

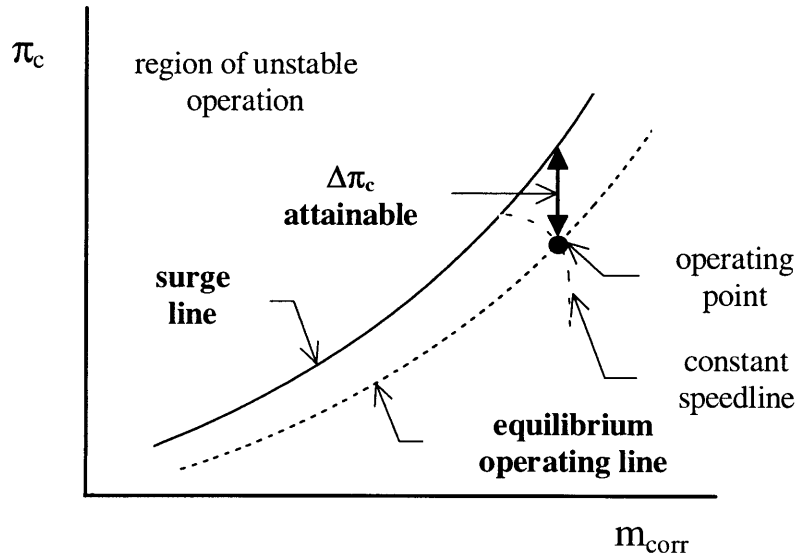

Figure 1.1: Compressor operating map indicating surge line, operating line, and $\Delta\pi_c$ attainable used in the calculation of stall margin.

Utilizing the remaining increments of efficiency near the surge line is desirable, but stability must not be compromised. Artificial stabilization techniques involving feedback control have proven successful in laboratory compressor rigs and low pressure ratio gas turbine engines, essentially shifting the surge line to lower mass flows. The next logical step is demonstrating this technology on high pressure ratio aircraft engine hardware. These techniques rely upon one or several measured engine parameters which act as indicators of impending instability. Therefore, a serious effort in surge control requires an understanding of the engine's dynamics at operating conditions near instability onset. This goal is the basis for the work presented in this thesis.

1.2 Previous Work

1.2.1 Instability Modeling and Inception

Because of its costly consequences, a great deal of work has focused on compression system instability. A key to its understanding was the recognition of the system dynamic nature of the phenomena. In 1955, Emmons [2] proposed a model in which the compression system is treated similarly to a Helmholtz acoustic resonator, a plenum attached to an inlet

duct of smaller cross-sectional area. He investigated the linear stability of his system equations. Greitzer [3, 4] presented a different formulation of the equations; he examined the non-linear system dynamics in numerical simulations which were compared to experimental results. His contributions include establishing a non-dimensional parameter, B, which governs the stalling behavior of a compression system.

$$B = \frac{U_T}{2a_P}\sqrt{\frac{V_P}{L_{CD}A_C}} = \frac{U_T}{2\omega_H L_{CD}} \tag{1.1}$$

The parameter can be thought of as the measure of the ratio of a system's compliance (plenum compressibility) to inertia (mass of fluid within compressor ducting). A high value of B is required for a system to exhibit surge, for the energy stored in the plenum must be sufficient to overcome the compressor duct inertia and allow the blowdown of flow back through the compressor. Low B axial compressors, such as that examined in his study, exhibit only rotating stall when mass flow is throttled. Greitzer also elucidated the differences between static and dynamic compression system instabilities and the criteria which must be present for each. Dynamic instability, the more limiting of the two cases, requires only a very small positive slope in the constant speed compressor characteristic (speedline in Figure 1.1); thus, the surge line is almost always located near the peaks of a compressor's speedlines. Moore and Greitzer [5, 6] later formulated a first principle 2-D rotating stall propagation model which illustrated the coupling between rotating stall and surge modes of instability. This tractable framework led to advancements in the understanding of instability inception in axial machines.

Unlike axial machines, there is less broad agreement concerning the fluid dynamic phenomena which contribute to instability inception in centrifugal machines. Complicating this factor is the wide variety of centrifugal compression system designs. Consider the range of behavior documented in the following studies for centrifugal compressors with vaned diffusers. Toyama [7] and Dean [8] present time domain analyses of surge inception of several high pressure ratio (>5) centrifugal stages with vaned diffusers. Both studies observe low frequency, mild surge fluctuations at operating points near the surge line. During these oscillations, the operating point occasionally crosses the nominal surge line without initiating deep stall. It was hypothesized that surge resulted when the instantaneous operating point was

pushed too far into the unstable regime to allow recovery. The studies differ slightly in their interpretation of the deep surge triggering mechanism. Toyama cites a limit in the pressure recovery from impeller tip to diffuser throat which causes a deterioration of the inlet flow, while Dean feels that this occurrence is preceded by a breakdown in the flow within the vane passages. Ribi [9] shows a low pressure ratio industrial compressor which also exhibits mild surge oscillations. This study attributes the triggering of surge to a condition of inducer rotating stall, occurring at the low mass flow points of the mild surge fluctuations. In stark contrast, Oakes, et al. [10] describe a high-speed centrifugal compressor with $\pi_c = 5.4$ which transitioned into surge after 9-lobed rotating stall within the vaned diffuser.

Several experimental projects at MIT have been performed on a pressure ratio of 2 centrifugal turbocharger with a vaneless diffuser. Fink [11] examined its surge dynamics to find, among other things, growing mild-surge oscillations corresponding to the system's Helmholtz frequency preceding deep surge. His identified surge triggering mechanism was a stationary asymmetry at the inducer which was related to asymmetries in the volute. In order to dynamically simulate his surge cycle oscillations, he added the influence of rotor speed variation to the basic surge model. The next section describes two active control experiments utilizing this compressor.

1.2.2 Control of Surge

Epstein, et al. [12] suggested that compression system instabilities could be controlled with minimal power if they developed as growing oscillatory phenomena. These oscillations could be arrested when the amplitudes were small, and thus easily manageable. Control efforts were divided into two areas: 1-D control of surge and 2-D distributed control of rotating stall. Day [13], Paduano [14], Haynes [15], and Gysling [16] successfully demonstrated rotating stall control using tip injection, independently moving IGV's, and aeromechanical feedback.

The research more of interest to this project is that of surge control on centrifugal machines. Two stabilization schemes were applied to a low pressure ratio turbocharger rig in order to extend its stable operating range. Pinsley [17] utilized unsteady plenum pressure as a

feedback variable to drive a fast acting throttle controller. Gysling [18] chose an aeromechanical feedback approach where plenum volume was adjusted by a movable wall responding directly to pressure fluctuations. Both techniques were successful in reducing the surge point mass flow approximately 25%.

The above success did not easily translate to gas turbine engine hardware. The increased unsteadiness in the flow phenomena in the engine, due in a large part to combustion, and the violent nature of surges adds a high degree of difficulty to the task. Ffwocs-Williams tested two pairs of actuators and sensors on a 60 h.p. auxiliary power unit with a centrifugal compressor of pressure ratio 3 [19, 20]. Unsteady plenum pressure sensing and plenum flow injection enabled recovery from deep surge triggered by a fuel spike. Diffuser pressure sensing and air injection into the impeller was utilized to realize a 2.6% extension in stable operating flow range. However, the conclusions of these experiments indicated that 2-D sensing and actuation would be required to stabilize the engine further.

This thesis is part of an effort to demonstrate active control technology on one of two helicopter engines in MIT's Gas Turbine Laboratory, both of which have high tip speed, high pressure ratio centrifugal stages. The current work was performed on an AlliedSignal (formerly Lycoming) LTS-101 gas generator which was initially installed and examined by Bell [21]. Similar studies involving an Allison 250-C30 engine are presently in progress. McNulty [22] performed sensor actuator studies similar to those of Simon [23] on a surge model modified to be applicable to a high pressure ratio gas turbine engine. With a linearized version of this model, McNulty studied several sensor/actuator pairs which could be implemented on the engine. He determined diffuser throat air injection coupled with inlet total pressure sensing would allow stabilization to the highest compressor characteristic slopes. Borror [24] studied the surge dynamics of this engine and tested the actuation method suggested by McNulty. Borror noted a slight increase in the spectral power level of pressure output below 100 Hz before the engine surged, but detected no global or 2-D mass flow or pressure oscillations. This apparent lack of precursor was explained by similar behavior in a non-linear engine simulation subjected to random process noise. The levels of unsteadiness which drove the simulation unstable were quantified and compared to experimental data.

1.3 Research Objectives

The goal of this continuing research is to explore the compression system dynamics of and, if possible, demonstrate active stability control on the LTS-101 gas generator. Building on lessons learned from Borror, most notably the requirement of greater control authority, this thesis examines the prerequisites to and the initial implementation of linear surge control. Linear control requires that actuation be available in both positive and negative directions from a given operating point, so the majority of experimentation was performed with a mean level of air injection. Thus, the gas generator including mean injection is the system to be stabilized by feedback control. Experimentation determined that this modified system exhibited markedly different dynamics near surge than the gas generator alone. The goal of this thesis is to identify this behavior, both mathematically and qualitatively, to support the development and testing of linear control laws.

The objectives of this research appear below in the order of appearance in this thesis:

- Quantify and explain the effects of steady-state, diffuser throat air injection on the pressure ratio and mass flow performance of the engine.
- Examine the surge behavior of the engine with and without a mean level of air injection.
- Perform open-loop, forced response testing to generate a linear system identification near the surge point.
- Determine the optimal feedback parameter.
- Examine the experimental results of the implementation of linear control law designs based upon the system identification.
- Adjust engine system modeling assumptions on the basis of the experimental observations.

Chapter 2: Experimental Facility and Test Procedures

2.1 Engine and Test Facility

The AlliedSignal (formerly Lycoming) LTS-101 is a 650 h.p. class helicopter engine. It is used in the Aerospatiale HH-65 Dauphin, Eurocopter BK117, and certain Bell 222 helicopters. For the experimental work at the MIT Gas Turbine Laboratory, the free power turbine and shaft are removed for testing of the gas producer alone. Figure 2.1 is a cross-section of the engine in the MIT test configuration. The LTS-101 generates a peak pressure ratio of approximately 8 through 1 axial and 1 centrifugal stage followed by a vaned diffuser. Air exits the diffuser into a reverse flow annular combustor which then feeds a single-stage, gas generator turbine. Flow rate is controlled by the experimental rig's variable-area nozzle, which will be addressed in more detail.

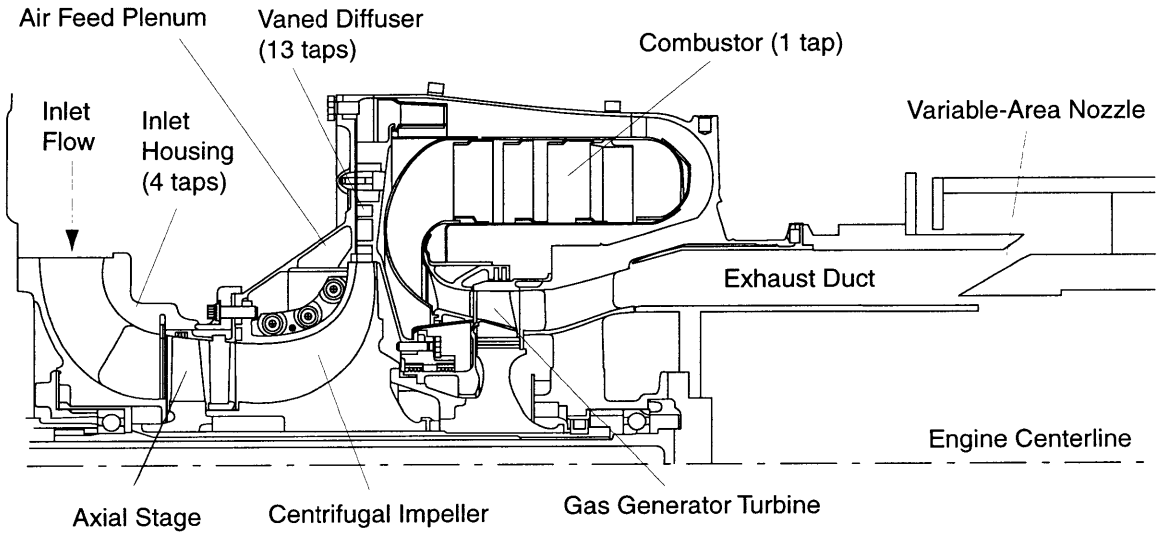

Figure 2.1: Cross section of the AlliedSignal LTS-101 gas generator in the MIT test stand configuration with the locations of high-frequency pressure taps shown

To facilitate surge testing in a safe and manageable manner, two components of the gas generator hardware differ from their production counterparts. In order to insure that the centrifugal stage limits the stable operating range of the engine, diffuser throat areas are

slightly enlarged. Also, turbine nozzle area has been reduced to raise the operating line, providing safe turbine inlet temperature margin during surge.

Figure 2.2 illustrates the test facility assembled by Bell, which is described in greater detail in his S.M. thesis [21]. The test rig is mounted on a steel frame inside a large, reinforced concrete test cell. The engine is operated by computer from a station outside of this cell. Video cameras facilitate visual monitoring. To eliminate thermal inlet distortion effects from the radiated heat of the engine, inlet air is collected from the roof of the laboratory and ducted to the vertical bellmouth inlet. Rubber skirting on the 3 ft. diameter ducting provides the interface between a flat wooden platform (not shown in the figure) mounted near the bellmouth entrance. The skirting's flexibility allows the engine the freedom of movement required for operation of the variable area nozzle while remaining connected to the outside air ducting. The exhaust ducting contains acoustic absorbers and extends to a 40 ft. tower on the laboratory's roof for the attenuation of acoustic energy. The lack of a power turbine results in high exhaust temperatures. Therefore, this ducting is evaporatively cooled by water injection when the temperature exceeds a threshold level.

The rig is equipped with a variable-area nozzle for controlling mass flow. The flow area of a downstream throttle, such as a power turbine, defines the operating line of a gas generator. As the throttle area decreases, mass flow reduces, and the operating point approaches the surge line. The LTS-101 mounts on a steel sled supported by linear bearings. These bearings allow 1-D movement in the direction of the machines rotational axis. The nozzle design consists of segments of two concentric cones (see cross section in Figure 2.1). When the outer-radius nozzle section, which is attached to the gas producer, moves with respect to the inner-radius section, attached to the stationary exhaust diffuser, exhaust area changes. The position of the gas generator, and thus nozzle area, is adjusted by a linear actuator and electronic position controller. The thrust produced by the gas generator requires a compensating weight and pulley system to insure loading levels remain within the operating limits of the actuator.

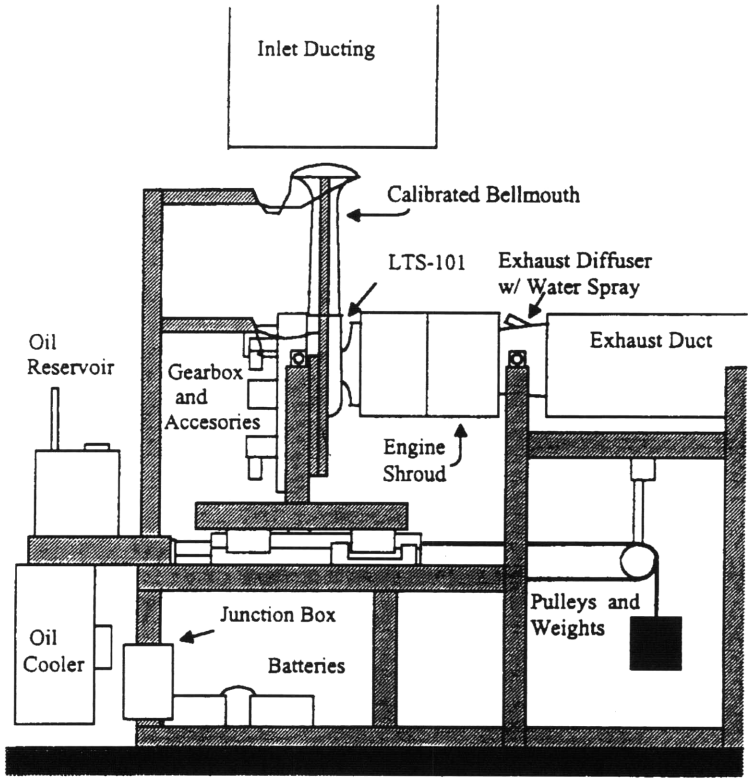

Figure 2.2: LTS-101 gas generator test stand (figure from [21])

Basic engine operation and data recording is accomplished through Genesis, a PC-based process control software package. Genesis interfaces with A/D and D/A boards for the recording (1 Hz sample rate) of temperatures, pressures, shaft speed, etc., and the control of valves, switches, power lever angle, and nozzle position, respectively. Genesis is also configured to monitor engine operational and safety limits and initiate corrective action when necessary. Examples of safety-related measures include automatic power chops to idle or fuel flow interruption. Shaft speed, cooling water flow, fuel flow, and exit gas temperature (EGT) are also monitored on external panel meters near the operator. Alarm circuitry within these meters is used to interrupt fuel flow when extreme values are encountered. Manual fuel and power switches located on this panel may also be utilized for emergency shutdowns.

2.2 Instrumentation

The purpose of this section is to describe the sensors used for measurements in this thesis, both for steady-state performance and dynamic behavior. Sensors not specifically used in this study, such as instrumentation for monitoring the condition of the rig and engine, are omitted but can be found in [21].

Steady-state performance measurements are recorded at 1 Hz sampling rate by the Genesis package and are used to determine the gas generator's operating point. Referred mass flow (flow corrected to sea-level standard conditions) is calculated from an AlliedSignal provided calibration to static pressure depression at the inlet bellmouth entrance. At this location, four taps are connected to a common pressure line, physically averaging the sensed pressures. It is measured by a Setra Model 239 pressure transducer with an operating range of 0-15 in. H_2O psid. Atmospheric pressure is measured inside the test cell with a digital Setra Model 370 transducer with a range of 8.70-15.95 psia. Inlet temperature is measured with 4 type K thermocouples mounted in a FOD screen over the mouth of the inlet, one of which is used for correcting gas generator shaft speed. Shaft mechanical speed is measured by an AlliedSignal supplied tachometer, converted into % N_1 by a panel mounted frequency counter, and then transmitted digitally to Genesis for recording.

Compressor discharge pressure, P_3, is used in conjunction with atmospheric pressure for the computation of gas generator pressure ratio. It is measured by a Setra Model 204 transducer with an operating range of 0-250 psid. Compressor discharge temperature, $T_{t,3}$ is measured by a type K thermocouple.

Fuel flow is measured by a flowmeter which outputs a TTL signal to a frequency counter for conversion to engineering units. The converted measurement is transmitted digitally to Genesis. $T_{t,41}$, turbine rotor inlet temperature, is calculated from inlet mass flow, $T_{t,3}$, and measured fuel flow. During tests near the surge line, the engine approaches the $T_{t,41}$ limiting value because of the lower level of air flow passing through the engine. When injection is employed, the calculation must be corrected for the added mass flow. For a 2% m_{des} level of

injection, the corrected $T_{t,41}$ value is approximately 25° R lower than the Genesis calculated value, the reading observed by the engine operator.

Prior to and following each run, the Setra pressure transducers measuring P_1, P_3, and P_5 are calibrated versus the digital Setra pressure transducers over their expected operating ranges. The digital pressure gauge used in the measurement of atmospheric pressure is used to calibrate P_1. P3 and P5 are calibrated with a digital Setra Model 370 with a range of 0-100 psia. The calibration is automated using a separate Genesis code, and calibration constants are checked for consistency before proceeding with the run plan. Cell temperature changes during the run were shown to cause a shift in the pressure transducer calibrations. Jinwoo Bae, a member of the project team, installed a cooling air feed system with the goal of maintaining constant transducer temperature to minimize this source of error.

Table 2.1 shows accuracy estimates for the steady-state instrumentation. Accuracy estimates for calculated performance parameters are obtained by propagating the values in Table 2.1 through the appropriate equations (see Table 2.2). These estimates also require mean parameter values at experimental conditions, which were obtained from data. It is important to note that these values reflect only instrumentation accuracy and not the added uncertainty of operating point fluctuations and other system noise related scatter.

Parameter	Sensor	Range	Accuracy
$P_{ambient}$	Setra 370 (digital)	8.70-15.95 psia	±0.0070 psia (±0.097% F.S.)
P_1	Setra 239	0-15 in. H_2O	±0.034 in. H_2O (±0.22% F.S.)
P_3	Setra 204D	0-250 psig	±0.96 psig (±0.38% F.S.)
T_{inlet}, $T_{t,3}$	Type K TC	-	±4.0° R

Table 2.1: Accuracy estimates for steady-state, performance instrumentation

Calculated Parameter	Accuracy
π_c	±0.82% π_c
$m_{inl,corr}$	±0.16% m_{des}
$T_{t,41}$*	±11° R

*Fuel flow accuracy estimated to be ±1%

Table 2.2: Accuracy estimates for calculated parameters

Of particular importance in this research are the unsteady pressure measurements at various locations throughout the engine. Measurements were made with Kulite XCQ-062 (50 and 250 psid range) and XCS-062 (5 and 15 psid range), high-frequency response, silicon diaphragm pressure gauges. The transducers feature thermal compensation circuitry and an accuracy specification of ±0.5% full scale output. Pacific Scientific 8650 bridge completion amplifiers provided excitation and signal conditioning for the transducers. Each Kulite has a reference pressure port which is connected to either a vacuum for absolute readings or left open to atmosphere to measure gauge pressure. Both gauge and absolute measurements were made with the choice depending upon the expected pressure values at each location and transducer physical limitations and resolution requirements. The pressure transducers were installed in a protective housing which provided strain relief for the leads, water-jacket cooling near the transducer, and a female AN fitting for attachment to the engine.

All taps were constructed of 0.072 in. I.D., annealed stainless steel tubing. In previous testing, male AN fittings were brazed directly to tap tubing, providing a connection to the transducer assembly. However, it was noted that a small volume existed in the tap connection at the interface of the male and female AN fittings, an undesirable characteristic from a frequency response standpoint. Therefore, the connection was modified with a brass insert to fill this volume and provide uniform tap geometry from engine to sensor. This insert was brazed directly to the tap tubing and fit freely into a machined cavity in the male fitting. This design had the added benefit of allowing free rotation of the male fitting around the insert, which reduced strain on the tubing and Kulite cables during sensor installation and removal. Leakage was prevented by squeezing an o-ring between the base of the insert and male fitting.

Figure 2.3 illustrates the cross-sectional location of the 4 high-frequency, inlet static pressure taps. The four taps are approximately 11 in. long and located 90° apart, between the struts in the inlet assembly. The purpose of these taps was to replace the long, small diameter taps located in the axial stage stators which Borror [24] found to have poor frequency response characteristics. The vaned diffuser has 13 taps distributed between three different flowpath locations as shown in Figure 2.4. Throat taps are approximately 8 in. long and located near the entrance to the diffuser vane passages. There is some uncertainty as to the

location of these taps within the passage, but [24] suggests that these taps are nearer the entrance of the diffuser than the throat, defined by a perpendicular line from the leading edge of the vane suction side. The utility of this tap location appears to be diminished by its proximity to the centrifugal rotor and its associated high-speed, highly unsteady flow field. The data is characterized by high-levels of broadband noise with little coherent structure. The 6 in. vane plenum taps were installed to examine performance and the circumferential uniformity of injection. Diffuser exit taps are approximately 4.5 in. long and are located in three passages, 120° apart. In addition to providing information regarding pre-surge oscillations at this location, they can also help quantify diffuser performance under the influence of injection. Table 2.3 shows the typical tap and transducer setup for the experiments in this thesis.

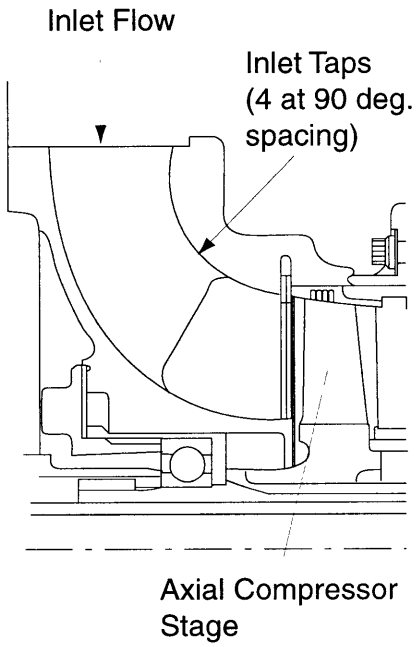

Figure 2.3: Inlet cross-section showing location of high-frequency taps

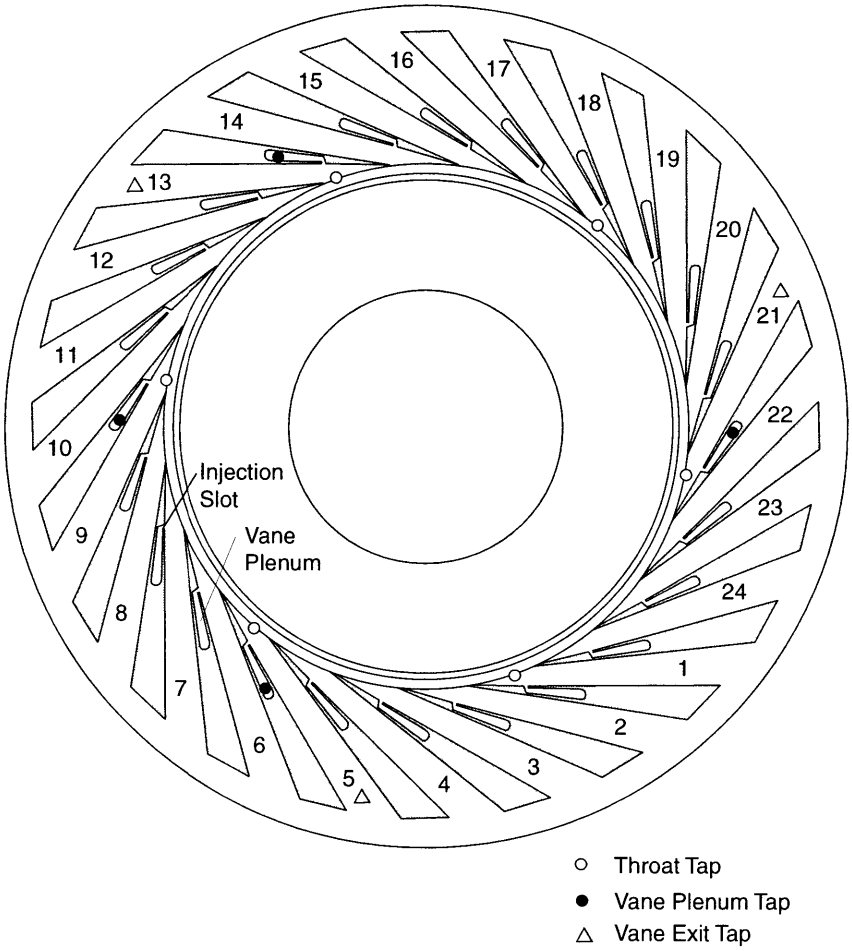

Figure 2.4: Vaned diffuser detail showing location of high frequency pressure taps

Tap Location	Vane or Tap #	Transducer Range
inlet	1	5 psig
inlet	2	5 psig
inlet	3	5 psig
inlet	4	5 psig
diffuser throat	5	50 psig
diffuser throat	13	50 psig
diffuser throat	21	50 psig
vane plenum	13	250 psia
vane plenum	21	250 psia
diffuser exit	5	250 psia
diffuser exit	13	250 psia
diffuser exit	21	250 psia
combustor	N/A	250 psia

Table 2.3: Typical high-frequency pressure tap instrumentation list

The amplified output of the pressure transducers is filtered by an On-Site Instruments TF-16-04 programmable filter board powered by a dedicated PC. The 8-pole, Cauer (elliptic) anti-aliasing filters have a rolloff of 75 Db/octave above the cutoff frequency, which was set at 600 Hz for all runs. Therefore, the influence of rotor revolution frequency, ~760 Hz, was eliminated. Unsteady pressures and the actuator command and position are recorded on a dedicated data acquisition PC running two 8-channel, 12-bit, Adtek AD-380 A/D cards. The sampling rate used was 4 kHz, satisfying the Nyquist sampling criterion for frequencies below 600 Hz.

Real time monitoring of signals in both the time and frequency domains was accomplished using several oscilloscopes and a Hewlett Packard 35665A spectrum analyzer, respectively. Typically the frequency content of an inlet pressure transducer was monitored by the spectrum analyzer. Near surge (in cases with injection only) a broadband peak centered around 27 Hz would appear, and its magnitude provided an indication of the proximity of surge. The analyzer was also used in the experimental tuning of controller gains.

2.3 Actuation System

McNulty's linearized stability studies concluded that the best actuator for active surge control on the LTS-101, based upon the criteria of maximum attainable positive compressor slope, was diffuser throat air injection [22]. This section describes the air-injection system utilized on the LTS-101.

The actuation system is shown schematically in Figure 2.5. 100 psig, oil-free air is produced by a Sullair industrial air compressor and an associated dryer system. The air is filtered for particulate and flows through an adjustable pressure regulator. Flowrate is then measured by a Fisher Porter rotameter with a calibrated range of 123.8 scfm. For measurement of mass flow, rotameter output is corrected by pressure and temperature readings from a Wallace Tiernan 300 psig dial pressure gauge and type-K thermocouple, respectively. Flow then passes through a remotely-operated, pneumatically-actuated ball valve, the primary on/off control for the injection system. As a safety precaution, this valve is configured to fail in a closed position during a power interruption. Air then passes into the primary element of

the actuation system, the high-frequency response valve, which is described in the following paragraph. The output of this valve enters the annular feed plenum within the impeller cover of the engine (see Figure 2.1). 24 angled slots around this annulus connect the feed plenum to openings directly over the vane plenums (see Figure 2.4). In previous experiments, this connection was thought to be a large source of pressure loss within the system, so the slots were machined to be approximately 7-times the area of the original orifices. Air is injected perpendicular to the primary gas path through slots in the vane walls.

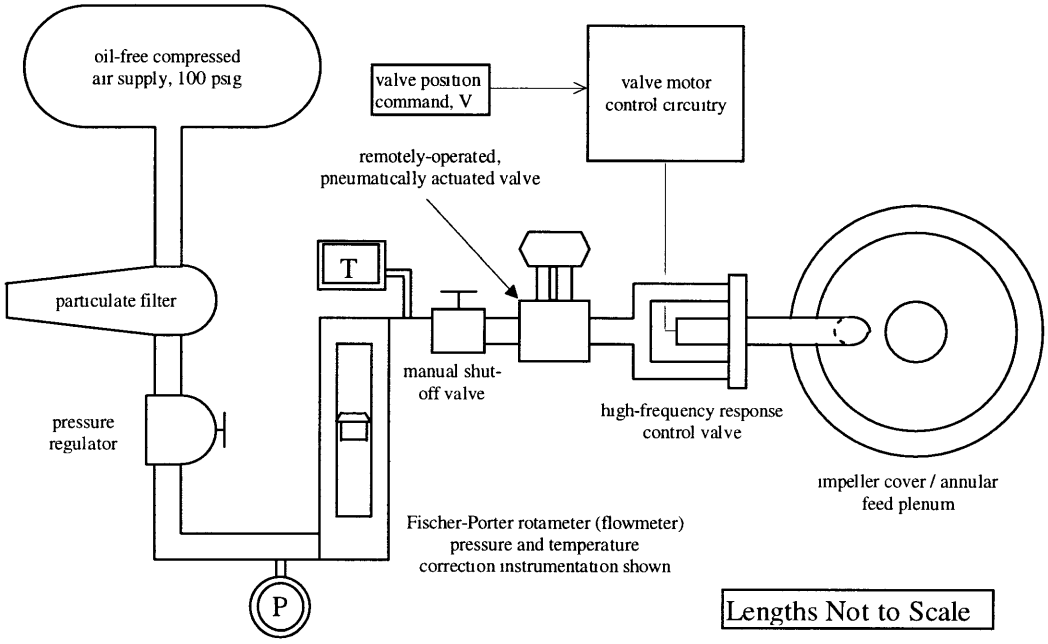

Figure 2.5: Schematic of air injection feed system

Parameter	Sensor	Range	Accuracy
Injected Flow	Fisher-PorterRotameter	0-123.8 scfm	±2.5 scfm (±2% F.S.)
P_{inj}	Wallace-Tiernan Gauge	0-300 psig	±0.3 psig (±0.1% F.S.)
T_{inj}	Type K TC	-	±4.0° R
Calculation			
m_{inj}	-	-	±0.17% m_{des}

Table 2.4: Acuracy estimates for flow injection measurements

The high-frequency response control valve is the prototype of the actuator designed by Berndt for use in distributed control of rotating stall. Details of this valve may be found in [25]. The valve has a bandwidth of 300 Hz, a leakage flow of 1% m_{des}, and a maximum flow of 4% m_{des}. The primary element of the valve is a linear actuator produced by the MOOG corporation. It positions a closing slider over slots for the passage of air which are machined in a cylindrical body. A -10-10 V input signal is processed by a control unit which adjusts the motor's coil currents to position the slider in the requested position. The frequency response of the slider's position to command is provided in Figure 2.6, as well as the poles of the transfer function fit in Table 2.5.

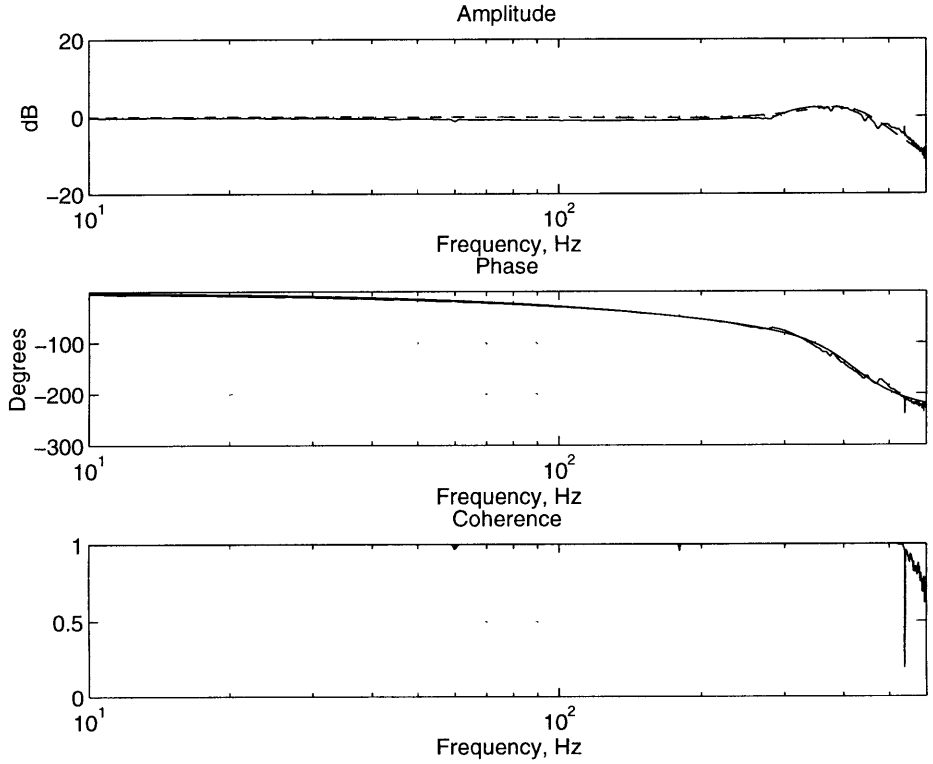

Figure 2.6: Frequency response of valve position vs. valve command, solid line is experiment, dashed is transfer function fit.

Poles	Frequency, Hz	Damping Ratio, ς
-535.911 ± 2588.57i	411.98	0.2027
-1496.37	-	-

Table 2.5: Valve command to valve position transfer function poles

Since the overall pressure ratio of the injection system is insufficient to choke the valve slots, the smallest area in the injection path, flow is a non-linear function of valve position (or valve command, equivalently). Figure 2.7 illustrates the flow versus valve command at the back pressure of a typical operating point. Although, the relationship is non-linear, for small perturbations around a mean injection value, such as used in forced response and control testing, the relationship can be approximated as linear.

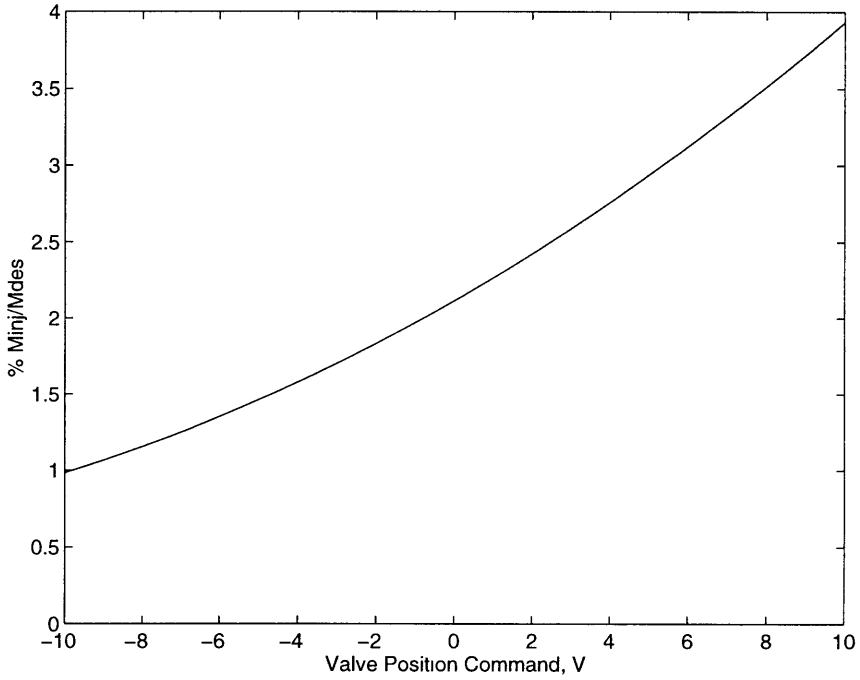

Figure 2.7: Injection flow vs. valve command relationship measured at a typical test operating point

2.4 Control Law Implementation Equipment

A detailed schematic of the control and high-speed data acquisition setup is shown in Figure 2.8. Signals utilized in control law implementation are indicated by evenly dashed lines. These signals are recorded by the high-frequency data acquisition system described previously but are split to be utilized as feedback and/or real-time monitoring parameters. The PC dedicated to performing the control algorithm calculations receives the feedback signals through a Data Translations DT2801 12-bit A/D card. This card has a total maximum sampling rate of 13700 Hz while using DMA transfer. This sampling rate is split between 7 input

signals (the maximum number anticipated for future control testing) which may be utilized by a control algorithm, 6 control parameters and a termination signal for control law execution.

The control algorithm is coded in a FORTRAN program originally written by Dr. Chris Van Schalkwyk. It implements a discrete, state-space control law design. In order to provide robustness to steady-state shifts in measured pressures triggered by nozzle movements and/or speed corrections, input parameters are digitally high-pass filtered at 5 Hz within the control algorithm. During execution, feedback parameters as well as output of the control law are continuously written to a circular buffer in the memory of the computer. When a kill control law execution command is detected, this data may be saved to disk for the short period of time preceding the termination command.

The calculated valve command is sent to a Burr Brown PCI-20093W-1 12-bit D/A board which outputs a ±5 V signal. The desired input range of the valve control circuitry is ±10 V, so the signal is amplified by a Pacific Scientific 8650 configured as an instrumentation amplifier. The valve command and resulting position are recorded by the high-frequency data system, and the position is monitored for fault detection on an oscilloscope.

2.5 Experimental Procedures

This section addresses the general operating procedures common to the engine experiments and specific techniques used in forced-response and controller experimentation.

A typical test team consists of four people. The test director plans the experiment and coordinates all members of the team in achieving its objectives. The director also performs high-speed data acquisition duties during the engine run. The engine operator controls and monitors the behavior of the engine. A controls/actuation operator focuses on the operation of the actuation system in both open and closed loop operation. This person monitors signal frequency content with the spectrum analyzer to determine proximity to surge and the effectiveness of actuation. During closed-loop testing, this individual is responsible for control law execution and tuning. An additional member serves as safety officer for the experiment. As the other members of the team may become engrossed in experimental details, the safety offi-

cer is responsible for monitoring test safety and parameters which may adversely affect engine health..

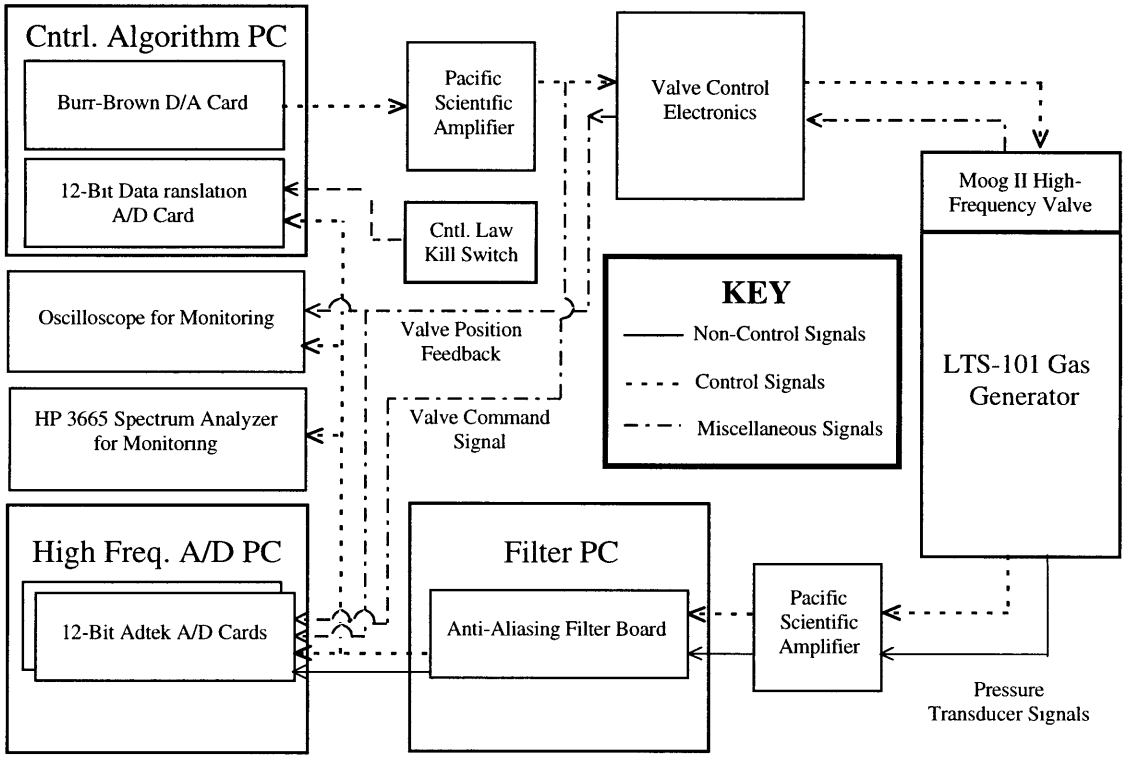

Figure 2.8: Schematic of signal flow for control applications

Before an experiment, both steady-state and high-frequency response pressure transducers are calibrated by separate processes. If the calibration is satisfactory, the cell is cleared of personnel and the engine started. The engine is allowed to warm up at idle for 3 minutes. It is then slowly accelerated to 95% $N_{1,corr}$, the speed chosen for experimentation (selected such that the flow fence, a part-speed stability enhancing device, is fully retracted from the flow path). The variable-area nozzle is slowly closed until the desired operating point is reached. This transition takes several minutes and is sufficient for engine warm-up at high power settings. As will be discussed in the following chapter, diffuser throat air injection allows the nozzle to be closed to a lower inlet flow operating point than without injection. Therefore, mean injection must be added before nearing the typical surge point to allow the operating point to be reduced further in flow. Nozzle movements and shaft speed corrections near the surge line are recorded with the high-frequency data acquisition system in case surge

is triggered. After testing is complete, the engine is allowed to cool down at idle for 3 minutes before shutdown. A post-run calibration is then performed on the pressure transducers to determine if any shifts in the calibration constants occurred during operation which would affect the collected data.

As nozzle area is decreased, exhaust temperature and turbine inlet temperature increase accordingly. Water injection is employed to limit exhaust duct temperatures, and $T_{t,41}$ is monitored to insure it remains in a safe operating range.

Once the desired operating point is established, testing can begin. High speed data acquisition is initiated by the test director at desired points. The engine operator marks steady-state data at the same time such that engine performance can be later correlated to unsteady measurements. If a surge occurs, the operator commands the engine to idle, via a panic button, and closes the remote, pneumatically-actuated valve in the injection feed system. Exhaust duct cooling water is automatically stopped to prevent flooding.

Frequency-response identification runs are accomplished by forcing the engine with sinusoidal air-injection. Two methods of spanning the desired frequency range were attempted. Frequency range sweeps resulted in low coherence of the transfer function estimates, so 15 s intervals of discrete frequency forcing was utilized. A programmable function generator allowed 3 of these intervals to be performed in succession and recorded conveniently on a 45 s data set. System identification was performed near surge, so forcing frequencies and amplitude had to be chosen carefully to avoid triggering instability.

For control experiments, the control law was tuned at a stable operating point near surge with mean injection. The impact of gain adjustments, which could be performed with type-in parameters in the control algorithm software, were monitored on the spectrum analyzer. With the controller's parameters selected, the operating point was moved toward surge in small increments, recording unsteady data during all transients. Testing generally continued until the engine surged.

Although not addressed in this thesis, closed-loop frequency response testing was accomplished by feeding a forcing function from a waveform generator to an open channel on

the control algorithm PC's A/D board. The control law output and forcing function were summed and sent as input to the valve controller via the D/A card. The forcing function was recorded on the high-frequency data acquisition system with unsteady pressures for evaluation of transfer functions.

Chapter 3: Steady-State Injection Response

In order to facilitate control applications, diffuser throat air injection must be capable of modulation in increased and decreased flow directions. This requirement mandates performing experiments with a mean level of injection. Injection modifies the compressor characteristic, the surge point, and the pre-surge behavior of the engine. The purpose of this chapter is to quantify the effects of injection which define this "new" machine and offer physical explanations for the observed behavior.

3.1 Characteristics and Surge Point

For a given nozzle position, diffuser throat air injection induces two effects on the gas generator: pressure ratio loss and a decrease in inlet mass flow. Figure 3.1 illustrates the effect of injection at two downstream nozzle positions and a shaft speed of 95% $N_{1,corr}$. As a reference, operating points without injection are shown as "o" on the plot. It is important to note that corresponding "+" marks of the two data sets do not represent equal amounts of injected air flow. However, the two nozzle positions can be compared by linear fits of the injection effects. Note that nozzle position B, nearest the peak of the speedline, exhibits higher pressure ratio loss per reduction of inlet mass flow. Data from Borror [24] indicate the same trend over several operating points but at lower injection levels.

The two effects discussed above are not independent. The amount of displaced inlet flow is greater than the injected flow. This discrepancy can be attributed to the constant inlet corrected mass flow of the gas generator turbine. A choked, downstream nozzle of given area enforces a matching condition of constant turbine inlet corrected flow, $m_{4,corr}$ [25]. Corrected mass flow is expressed as follows:

$$\frac{\dot{m}\sqrt{T_t}}{p_t A} = f(\gamma, M) \tag{3.1}$$

Figure 3.2 shows the constant values of $m_{4,corr}$ at two nozzle positions. $m_{4,corr}$, which includes both inlet and injected flow, is converted to an equivalent $m_{inl,corr}$ (the conversion entails multiplication by a constant at each nozzle position, leaving the qualitative nature of the $m_{4,corr}$ data unchanged) such that the operating point with zero-injection is identified relative to the 95% $N_{1,corr}$ speedline. From Figure 3.2 and equation 3.1, it is evident that changes in p_t and T_t from injection are connected with a readjustment in the amount of inlet mass flow for a given amount of injection. For example, the π_c loss attributed to injection (see Figure 3.3) drops $p_{t,4}$, requiring a reduction in total mass flow. Although not addressed in detail, injection also changes $T_{t,4}$ by modifying compressor-turbine work matching and lowering $T_{t,3}$ by the mixing of cooler injection air with the primary gas path.

McNulty [22] proposed that the p_t loss effects of injection were composed of two parts: (1) a mixing loss due to the injection of air perpendicular to the gas path and (2) the creation of a "boundary-layer" type blockage at the diffuser throat, linked in literature to pressure recovery performance degradation [26]. Experimental evidence from the current work and Borror [24] indicate that McNulty's estimate over predicts p_t loss. For a physical explanation of this effect, split the compressor pressure ratio, π_c, into the pressure ratios of the impeller and vaned diffuser, π_{imp} and π_{vd}.

$$\pi_c = \pi_{imp}\pi_{vd} \tag{3.2}$$

$$\pi_{imp} = f(m_{inl,corr}, N_{1,corr}) \text{ and } \pi_{vd} = f(m_{inl,corr}, m_{inj}, N_{1,corr}) \tag{3.3}$$

π_{vd} is decreased due to mixing of the injection stream with the gas path flow. The penetration of injection into a free stream flow has been shown to correlate with momentum ratio.

$$\frac{\rho_{inj} U_{inj}^2}{\rho_{fs} U_{fs}^2} \tag{3.4}$$

A value near 1 is necessary for significant penetration and the creation of blockage [22]. At an injection level of 4% m_{des}, the momentum ratio of injected flow versus gas path flow is approximately 0.023, essentially non-penetrating. Therefore, the blockage loss described by McNulty appears negligible. However, injection reduces m_{inl}. At constant speed, the axial

stage and impeller deliver greater turning to the flow; hence, π_{imp} must increase. Thus, π_{vd} and π_{imp} compete, limiting the p_t loss effect of injection.

This argument provides a plausible explanation for the slope difference in fits of injection effect between operating points. Operating points on steep, negatively sloped regions of the speedline, such as nozzle position A, exhibit less p_t loss than points on flatter sloped portions of the characteristic for the same amount of injection. Although, a characteristic was not available for the impeller only, its shape can be assumed to be similar to the complete characteristic, only shifted upward. Inherent is the assumption that diffuser p_t loss varies only slightly between operating points. With this assumption, a given negative $\Delta m_{inl,corr}$ created by injection creates a greater positive $\Delta\pi_{imp}$ at A than B. The greater $\Delta\pi_{imp}$ offsets more of the diffuser's mixing loss and yields a lower net p_t loss for the entire compressor. Therefore, injection will have the greatest effect on π_c at points near the peak of the characteristic, the region of greatest importance in compressor stability research.

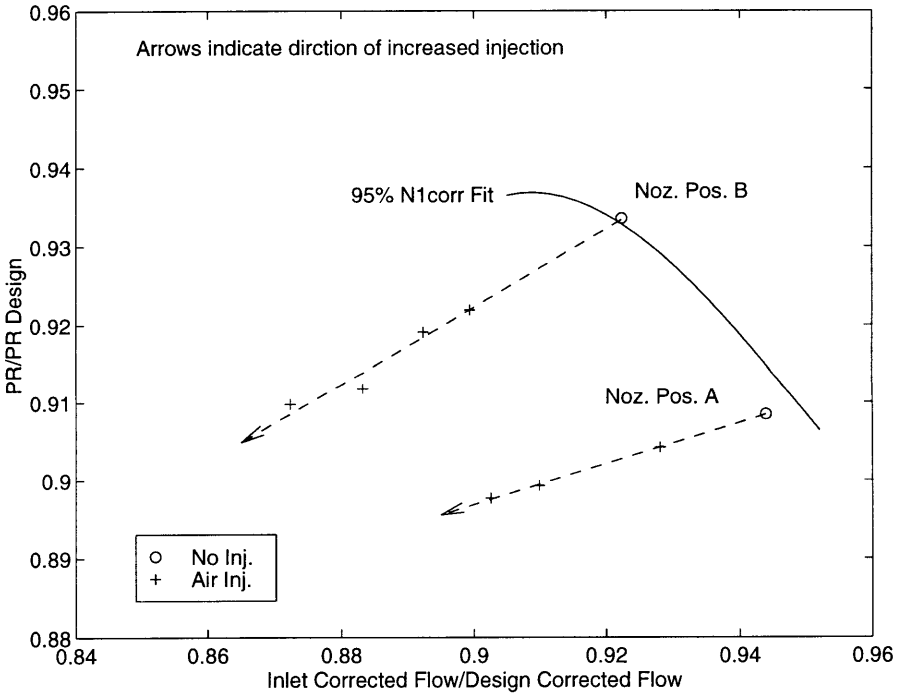

Figure 3.1: Effects of diffuser throat air injection on gas generator operating point

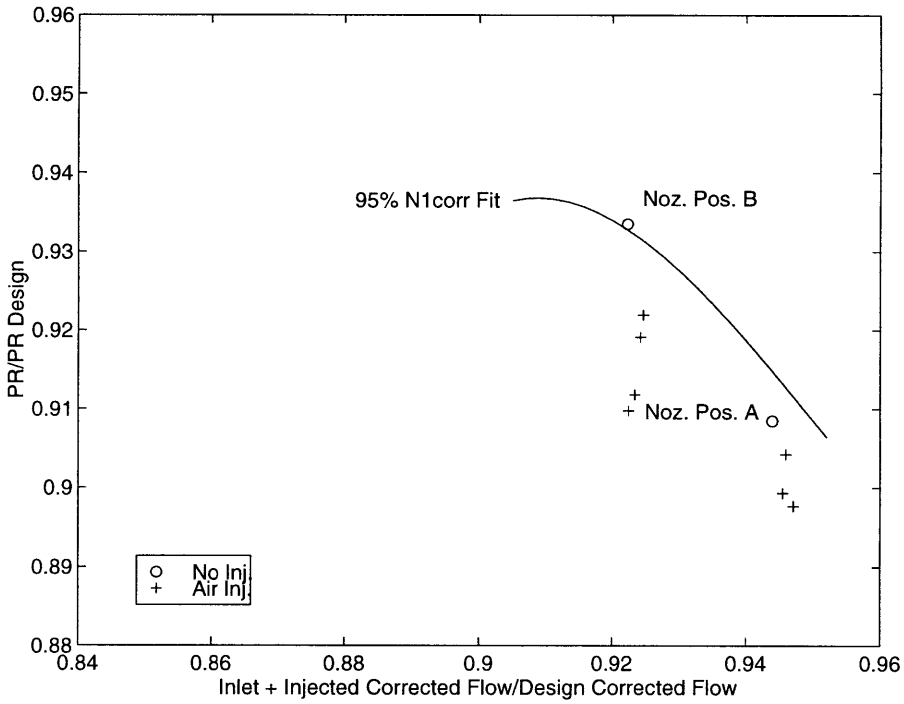

Figure 3.2: Turbine corrected flow at two nozzle positions with increasing levels of diffuser throat air injection. Flows are corrected to equivalent $m_{inl,corr}$ (see text for further explanation).

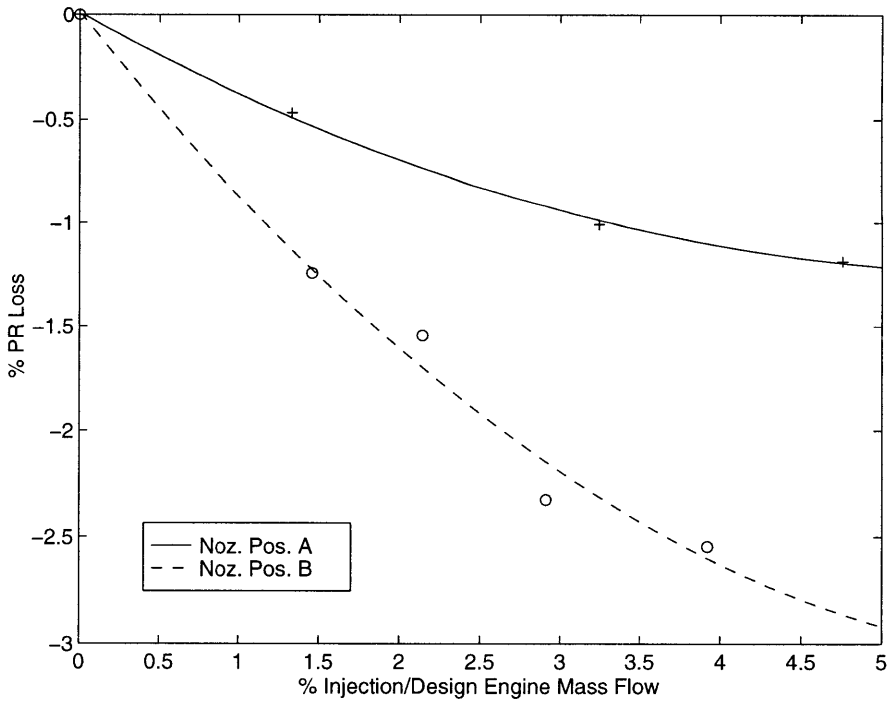

Figure 3.3: Percentage pressure ratio loss versus injection flow

The previous paragraph suggests that a compressor characteristic would exhibit a change in shape when injection is introduced, not a constant valued shift in π_c and $m_{inl,corr}$. Figure 3.4 illustrates experimentally determined 95% $N_{1,corr}$ speedlines near peak pressure rise both with and without a mean injection level of 2.14% m_{des}. This level was associated with the baseline valve position about which forced response and control law experiments were performed. Only data corresponding to $N_{1,corr} = 95 \pm 0.03\%$ were utilized in the fits. Process noise fluctuations of $\pm 0.1\%$ $N_{1,corr}$ are not uncommon, suggesting scaling the data points according to $\pi_c \propto N_{1,corr}^2$. This method was not utilized, however, due to poor correlation between π_c and $N_{1,corr}$ fluctuations. From visual inspection, the near-peak speedline data of the baseline zero-injection and mean-injection cases are well approximated by cubic and quadratic polynomials, respectively. Table 3.1 shows the calculated coefficients.

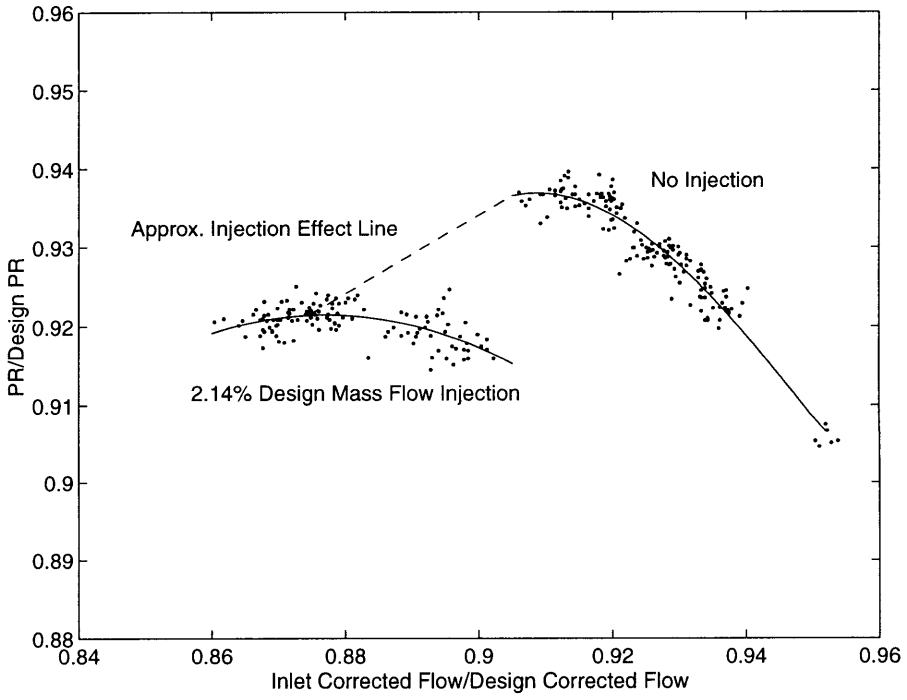

Figure 3.4: 95% $N_{1,corr}$ speedline curve fits

	$m_{inl,corr}$ / m_{des} Limits		Speedline Fit Coefficients			
Speedline	Low m	High m	m^3	m^2	m	constant
No Injection	0.905	0.952	186.960	-534.020	507.390	-159.454
2.14% Injection	0.860	0.905	N/A	-7.849	13.769	-5.116

Table 3.1: Speedline fit parameters

There are two features to point out concerning the speedline shift. The first is the shape difference of the characteristics near the peak. The baseline characteristic has a negatively-sloped stable region which flattens to a peak over a short range of $m_{inl,corr}$. The mean injection characteristic exhibits a gradual transition from negative slope to a region of mild positive slope, thus forming a large region of near zero slope at the peak. As will be seen later in the chapter, the flattening of the characteristic peak allows a dynamic instability, mild surge, to develop. The second feature is the stabilization (in the sense of surge) to lower $m_{inl,corr}$ and $m_{4,corr}$. The lower surge value of $m_{inl,corr}$ is apparent. Figure 3.4 also shows that if the slope of an injection effect curve near the surge point of the baseline case (approximated as the slope determined for nozzle position B in Figure 3.1) is extended to the mean injection characteristic, the surge points do not match. This line is an estimate of constant turbine corrected flow. This line shifts to lower flows as the variable area nozzle is closed, such that the zero-injection case is no longer stable. Therefore, mean injection stabilizes the gas generator to a lower turbine corrected flow operating point.

Figure 3.4 illustrates an important point. $m_{inl,corr}$ represents the flow through the axial stage and centrifugal impeller of the compressor. Since these components are stable (in the sense of surge) at lower corrected flow than the surge flow of the entire compressor, it can be concluded that surge inception is associated with diffuser behavior. This observation is consistent with the modifications described in Chapter 2, which were made to insure the diffuser would be the stability limiting element in the compressor. However, when injected flow is added to the inlet flow, the diffuser continues to operate below typical surge $m_{4,corr}$. This implies that a local fluid dynamic effect of the injection may be extending the flow range of the diffuser, not merely a 1-D effect of mass addition. One hypothesis in the literature surveyed in Chapter 1 suggests surge inception is triggered by a breakdown or separation of flow within

the vane passages [8]. At low $m_{inl,corr}$, diffuser inlet flow is highly tangential and may separate near the vane tip. Air injection may enhance surge stability by adding momentum to the region which is normally affected by inlet separation.

Operating points in this thesis are expressed in terms of $m_{inl,corr}$ and indicate the presence or absence of a mean level of injection. Since there was no means of monitoring injection at at each experimental time step, it was held at a constant mean value (typically 2.14% m_{des}) with error bounds of ±0.10% m_{des}. Therefore, significant operating point changes were recorded by monitoring $m_{inl,corr}$. Table 3.2 shows the surge points and rms fluctuations of $m_{inl,corr}$ for the experimental data. It is important to note that the values shown are averages of fluctuations exhibited by the last stable operating point prior to surge. Although further experimentation was not practical to determine repeatability, the author estimates similarly obtained surge points to fall in a range of ±1.5% $m_{inl,corr}/m_{des}$ from the tabulated values. Note the larger rms fluctuations in $m_{inl,corr}$ for the mean injection system, a fact which will be addressed in the next section.

Speedline	avg. % $m_{inl,corr}$ / m_{des}	% rms fluctuation
No Injection	90.76%	0.27%
2.14% Injection	86.38%	0.80%

Table 3.2: Experimentally determined surge points and rms mass flow fluctuations

3.2 Signal Frequency Content

An investigation of the surge inception process must examine the frequencies of naturally excited pressure disturbances encountered during operation. Of primary importance is the existence and frequency of any oscillatory, precursor behavior prior to surge. For instance, the turbocharger rig of Fink [11] exhibited 1-D, oscillatory behavior in mass flow and pressure rise at the system Helmholtz frequency. This behavior grew in amplitude until it developed into deep surge. Rotating stall may develop in the rotor or diffuser of a centrifugal system, or naturally excited acoustic disturbances may couple with surge dynamics. This section examines the dominant frequencies of engine operation near surge.

Borror [24] examined the surge behavior of the LTS-101 without flow injection. His conclusions were as follows:

- No linearly growing disturbances preceded surge.
- Frequency content below 100 Hz at throat, combustor, and inlet increased simultaneously around 250 ms prior to surge.
- Rotating stall was not present in the vaned diffuser based on measurements at the throat.

To examine the observations of Borror and to provide a baseline for comparison with mean injection experiments, the spectral content of engine taps with no injection was examined. Experimental data for this study was filtered with analog, 8-pole, Caur (elliptic), anti-aliasing filters set at a cutoff frequency of 600 Hz and digitally sampled at 4 kHz. Engine rotor frequency is ~760 Hz, so integral rotor revolution disturbances were eliminated from data sets. 2-pole, digital notch filters were employed to remove 60 Hz (and odd-numbered harmonics) electrical noise. These filters were implemented with the filtfilt.m MATLAB command. This algorithm eliminates the normally associated phase shift and effectively doubles the order of the filter. The power spectral density (PSD) of the averaged, or zeroth mode, of the taps at each axial location are plotted. PSDs show frequency distribution of signal power, such that the integral over a frequency range yields the power contained in that band. The units of the PSD are $\frac{(\text{psia})^2}{\text{Hz}}$. PSD calculations were performed by the MATLAB spectrum.m function (scaled by $\frac{1}{f_{sampling}}$). Hanning windows of 16384 points for the discrete fast Fourier transform were chosen on the basis of desired frequency resolution, which is determined by the following formula:

$$f_{resolution} = \frac{f_{sampling}}{\#\ \text{of DFFT points}} \tag{3.5}$$

$f_{resolution}$ = 0.244 Hz for these calculations. A window overlap region of 12288 points provides smoothing for the spectral estimate of the overall data set.

The taps include: 3-inlet, 3-diffuser throat, 2-vane plenum, 3-diffuser exit, and 1-combustor (the typical setup described in Section 2.2 Instrumentation). Figures 3.5-9 are the PSD's of these taps at two operating points near surge, $m_{inl,corr}/m_{des}$ = 0.910 and 0.908 (the last stable operating point before surge).

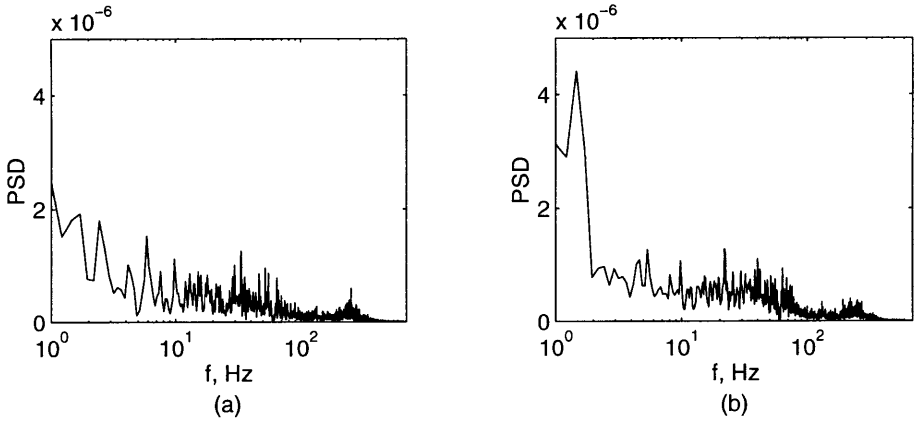

Figure 3.5: PSD of zeroth mode of inlet static pressure, zero-injection, at operating points $m_{inl,corr}/m_{des}$: (a) 0.910, (b) 0.908 (max. f = 700 Hz)

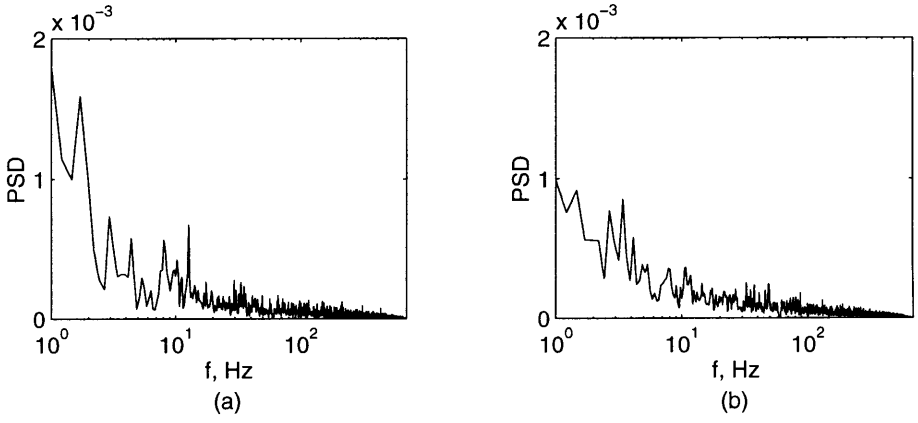

Figure 3.6: PSD of zeroth mode of diffuser throat static pressure, zero-injection, at operating points $m_{inl,corr}/m_{des}$: (a) 0.910, (b) 0.908 (max. f = 700 Hz)

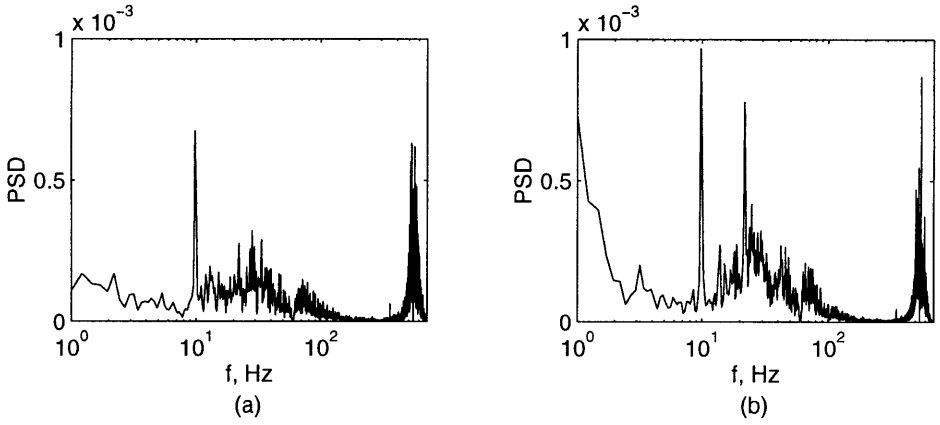

Figure 3.7: PSD of zeroth mode of vane plenum static pressure, zero-injection, at operating points $m_{inl,corr}/m_{des}$: (a) 0.910, (b) 0.908 (max. f = 700 Hz)

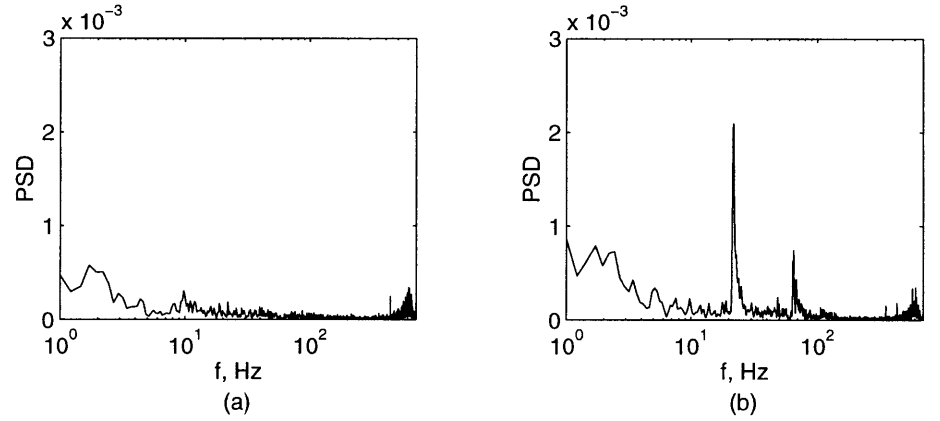

Figure 3.8: PSD of zeroth mode of diffuser exit static pressure, zero-injection, at operating points $m_{inl,corr}/m_{des}$: (a) 0.910, (b) 0.908 (max. f = 700 Hz)

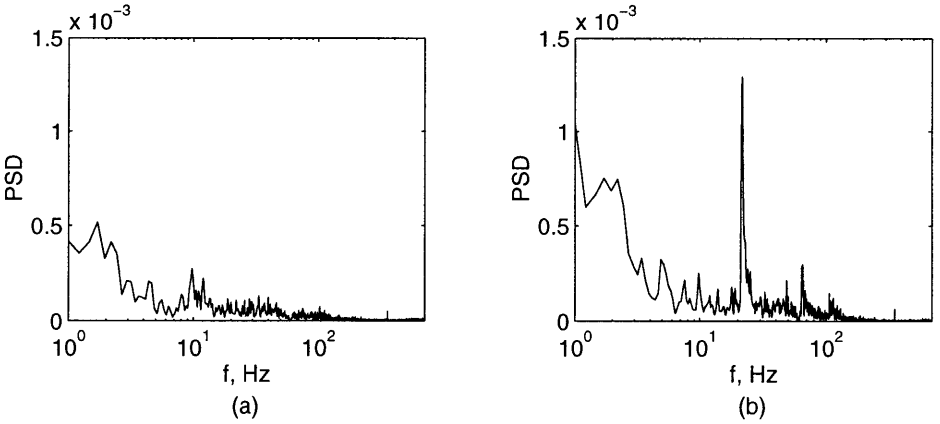

Figure 3.9: PSD of combustor static pressure, zero-injection, at operating points $m_{inl,corr}/m_{des}$: (a) 0.910, (b) 0.908 (max. f = 700 Hz)

Except for the throat, all taps exhibit slight growth in the spectral content below 100 Hz as the gas generator is throttled. The most prominent feature of these spectra is the sharp, 22 Hz peak appearing in all taps other than the diffuser throat at $m_{inl,corr}/m_{des} = 0.908$. It also exhibits a third harmonic near 65 Hz (frequencies are rounded to the nearest Hz). Other peaks appear but do not grow as the operating point moves closer to surge, suggesting that they may have little to do with instability inception. A summary of the observations, separated into categories of growing and invariant, appears in Table 3.3.

	Frequency Peaks, Hz	
Tap Location (# averaged)	Growing	Invariant
axial stage inlet (3)	22	252
diffuser throat (3)	none	none
vane plenum (2)	10, 22, 44, 65	555
diffuser exit (3)	22, 65	611
combustor (1, no avg.)	22, 65	106

Table 3.3: Dominant frequency peaks near surge for zero-injection case

Figures 3.10-14 examine frequency of pressures when the gas generator is subjected to 2.14 ± 0.10% m_{des} steady air injection. The operating points shown are $m_{inl,corr}/m_{des} = 0.873$ and 0.852 (the last stable point before surge).

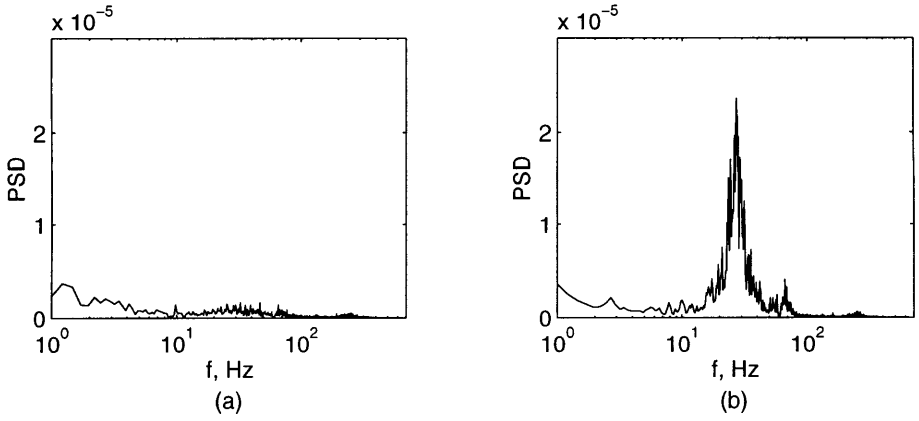

Figure 3.10: PSD of zeroth mode inlet static pressure, 2.14% mean-injection, at operating points $m_{inl,corr}/m_{des}$: (a) 0.873, (b) 0.852 (max. f = 700 Hz)

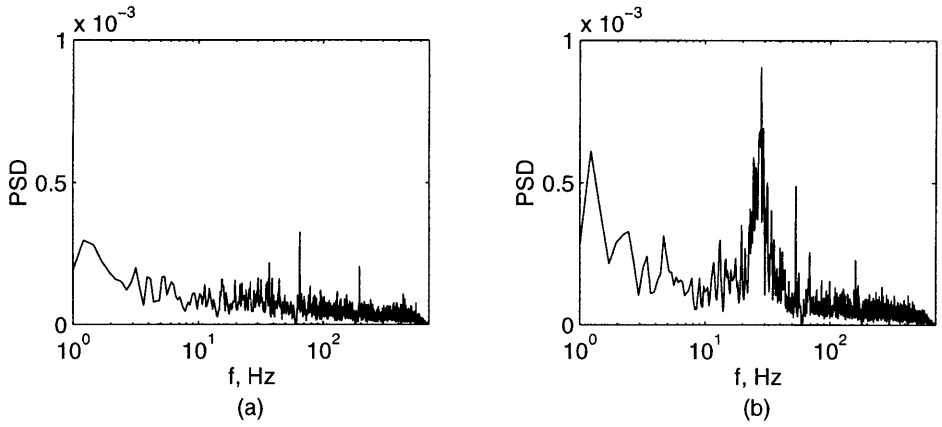

Figure 3.11: PSD of zeroth mode throat static pressure, 2.14% mean-injection, at operating points $m_{inl,corr}/m_{des}$: (a) 0.873, (b) 0.852 (max. f = 700 Hz)

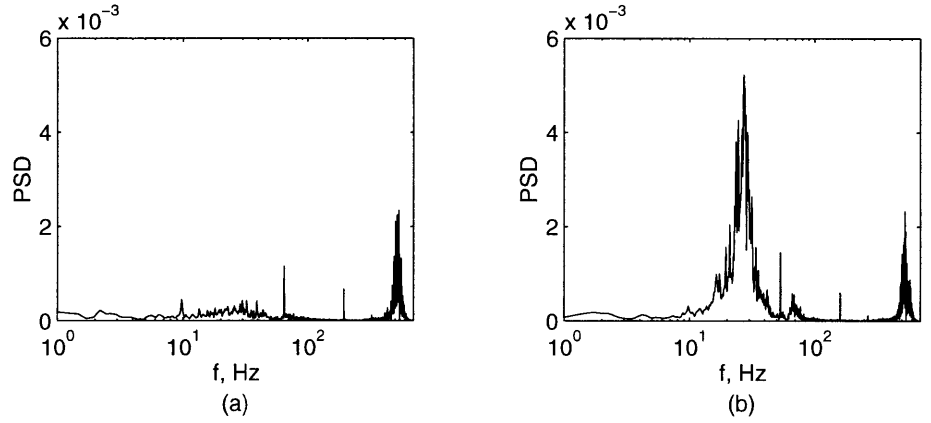

Figure 3.12: PSD of zeroth mode vane plenum pressure, 2.14% mean-injection, at operating points $m_{inl,corr}/m_{des}$: (a) 0.873, (b) 0.852 (max. freq. shown 700 Hz)

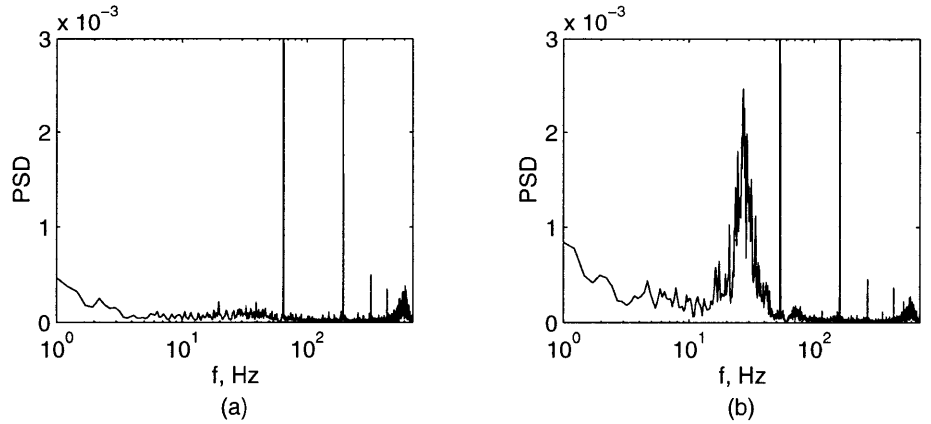

Figure 3.13: PSD of zeroth mode diffuser exit static pressure, 2.14% mean-injection, at operating points $m_{inl,corr}/m_{des}$: (a) 0.873, (b) 0.852 (max. f = 700 Hz)

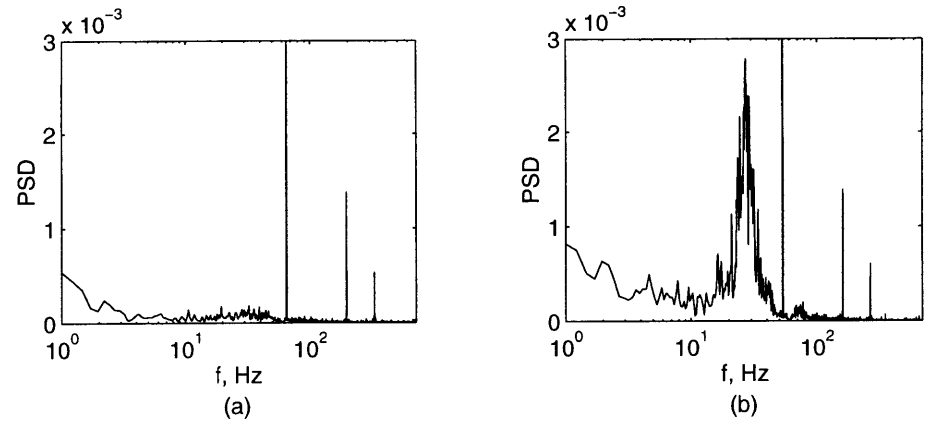

Figure 3.14: PSD of combustor static pressure, 2.14% mean-injection, at operating points $m_{inl,corr}/m_{des}$: (a) 0.873, (b) 0.852 (max. f = 700 Hz)

The dominant feature of the injection case is the appearance of clear, growing peaks at 27-28 and 66-69 Hz (throughout the thesis, these frequencies will be referred to as 27 Hz and 68 Hz). In comparing the magnitude of these peaks to the zero-injection case, note the different scaling of the y-axis values. For example, the 27 Hz peak observed at the inlet is approximately 17 times the magnitude of the 22 Hz peak seen without injection. Sharply defined stationary peaks not seen in the zero-injection case appear at 52 Hz and this frequency's odd harmonics. Table 3.4 summarizes the frequencies observed from this case.

	Frequency Peaks, Hz	
Tap Location (# averaged)	Growing	Invariant
axial stage inlet (3)	27, 67	250
diffuser throat (3)	28, 69	52 (har.)
vane plenum (2)	27, 67	52 (har.), 528
diffuser exit (3)	27, 71	52 (har.), 589
combustor (1, no avg.)	27, 68	52 (har.)

Table 3.4: Dominant frequency peaks near surge for 2.14% mean injection case

In order to assess the behavior of these frequencies immediately prior to surge, a waterfall plot showing the time variation of PSD is utilized. In this case, PSD values are calculated over 1024 points (0.256 s), then the time point is marched by 64 points (0.016 s). To allow comparison between injection and zero-injection cases, the surge point was arbitrarily defined by a sustained slope criteria (Δpsi/Δtime) on the pressure loss in the combustor during

the beginning of the surge blowdown. Figure 3.15 indicates the surge point selection corresponding to the zero-injection case.

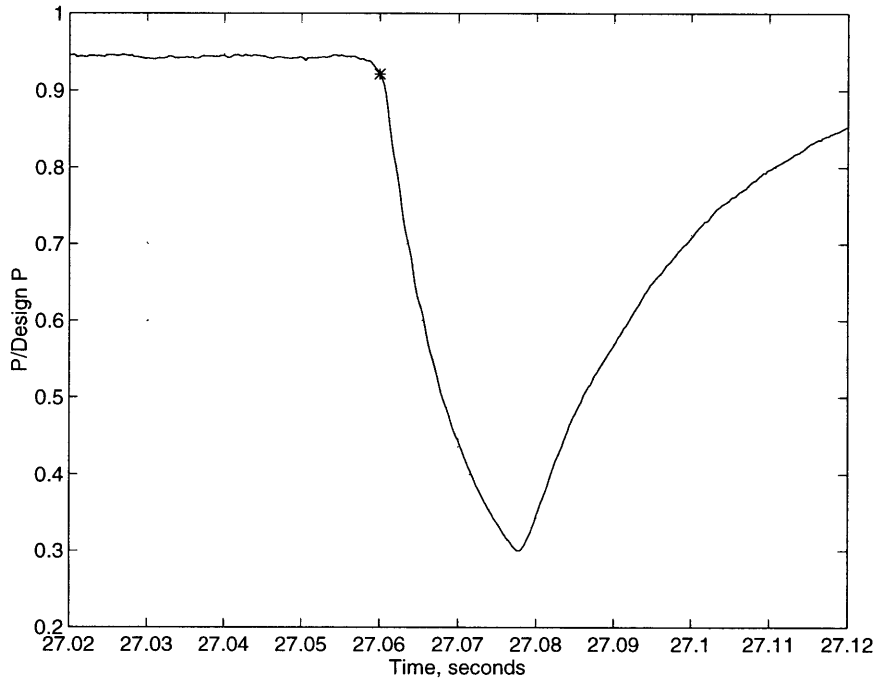

Figure 3.15: Surge point, identified by asterisk, on plot of combustor pressure

Figures 3.16-18 show waterfall plots of zeroth-mode inlet tap behavior for both cases (3.16 and 18 are plotted on the same z-axis scale for easy comparison). The plots are limited to frequencies of 0-100 Hz, the primary range of interest. Note that the zero-injection case shows virtually no dominant frequency activity prior to surge, even when the z-axis is scaled for better contrast, the frequency content is broadband. On the other hand, the 27 Hz mode is clearly visible with mean injection. However, this peak does not "grow" into the surge instability.

To assess the spatial structure of pre-surge activity for both zero and mean-injection cases, the spatial Fourier decomposition technique was utilized. At compressor inlet and diffuser exit, signals from the three corresponding taps are decomposed into their zeroth (1-D, surge-type oscillations) and first mode (1-lobe, circumferentially non-uniform) activity. With only three taps at each axial station, a spatial Nyquist criterion limits the decomposition to these modes. The pressure signals are normalized by their respective rms noise levels before

the modal decomposition. Figures 3.19-26 show the magnitude of the zeroth mode and the magnitude and phase of the first spatial mode for cases with and without mean injection.

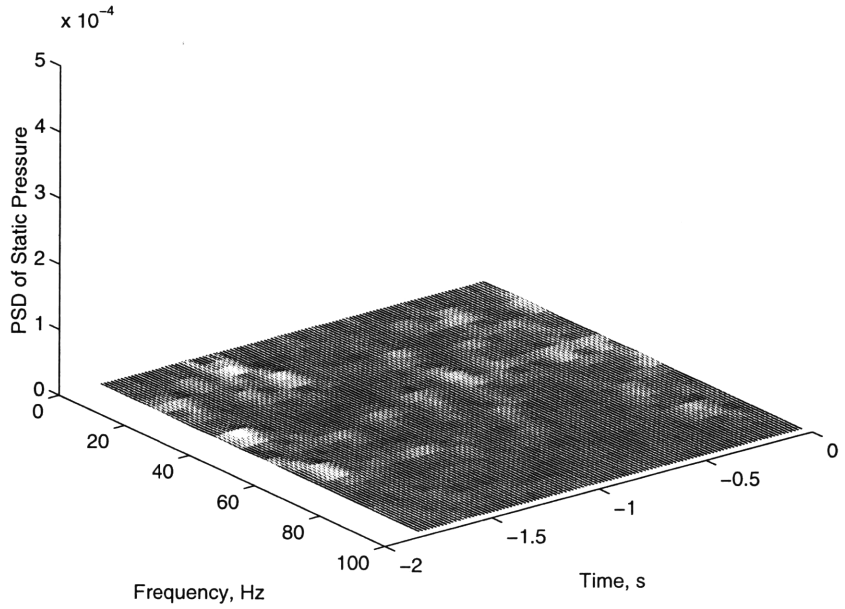

Figure 3.16: Frequency content of the zeroth mode of inlet static pressures during transition into surge (t=0), zero-injection case

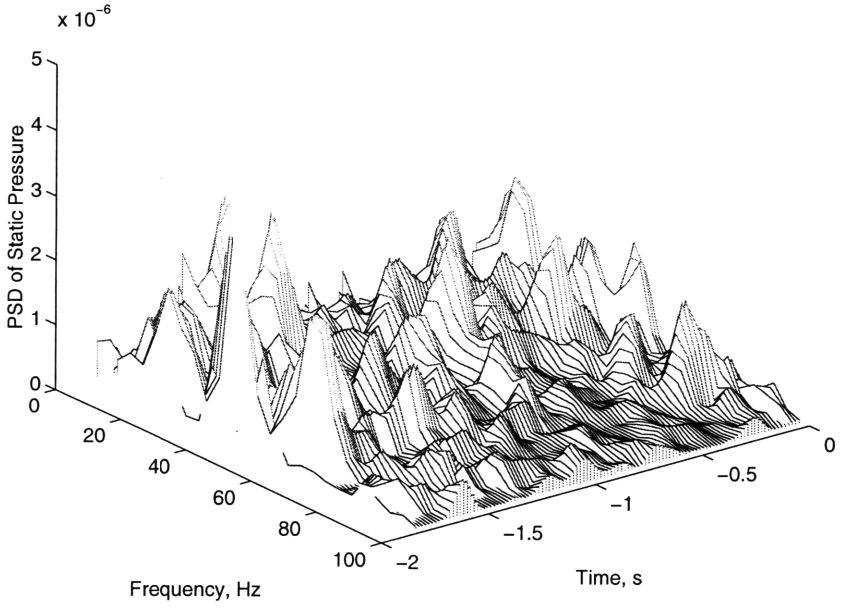

Figure 3.17: Enhanced view of frequency content of the zeroth mode of inlet static pressures during transition into surge (t=0), zero-injection case

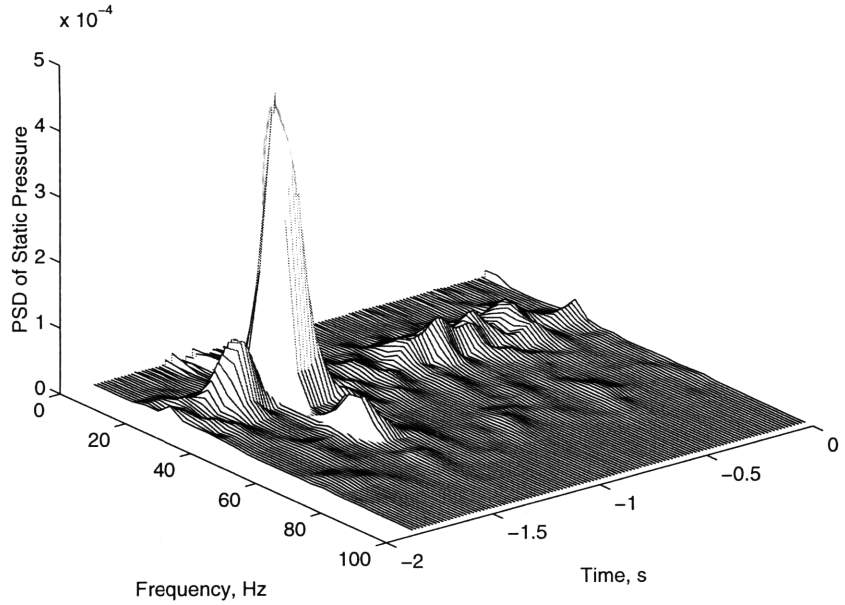

Figure 3.18: Frequency content of the zeroth mode of inlet static pressures during transition into surge (t=0), 2.14% mean-injection case

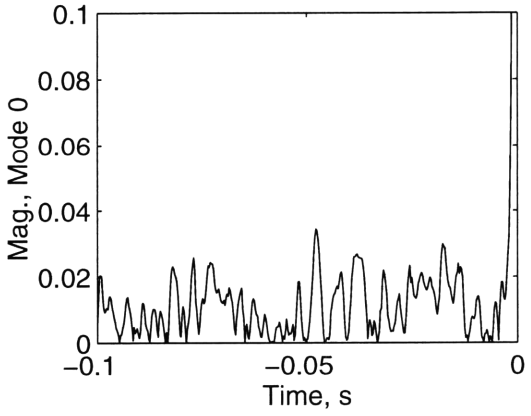

Figure 3.19: Magnitude of 0-mode spatial Fourier coefficient at inlet before surge, zero-injection case

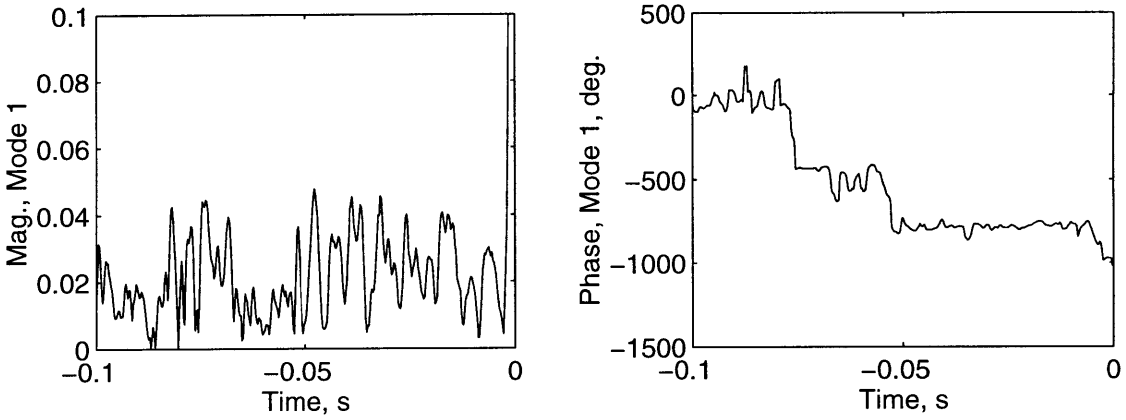

Figure 3.20: Magnitude and phase of 1-mode spatial Fourier coefficient at inlet before surge, zero-injection case

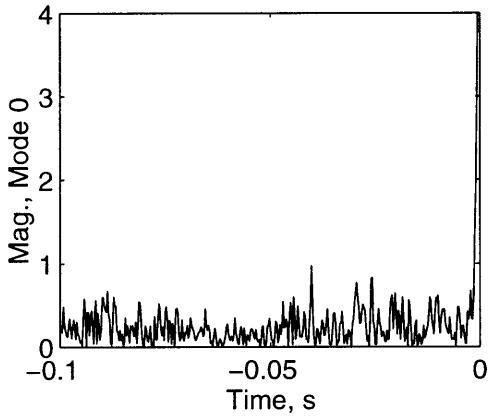

Figure 3.21: Magnitude of 0-mode spatial Fourier coefficient at exit of diffuser before surge, zero-injection case

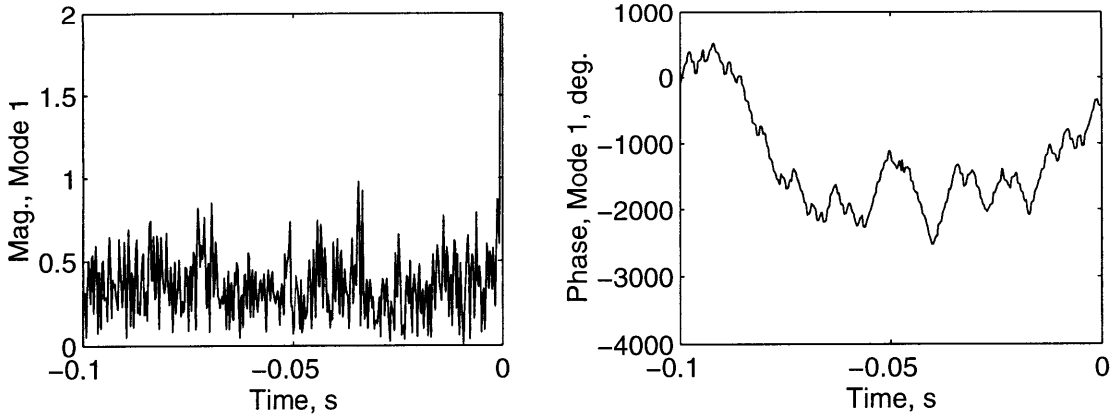

Figure 3.22: Magnitude and phase of 1-mode spatial Fourier coefficient at exit of diffuser before surge, zero-injection case

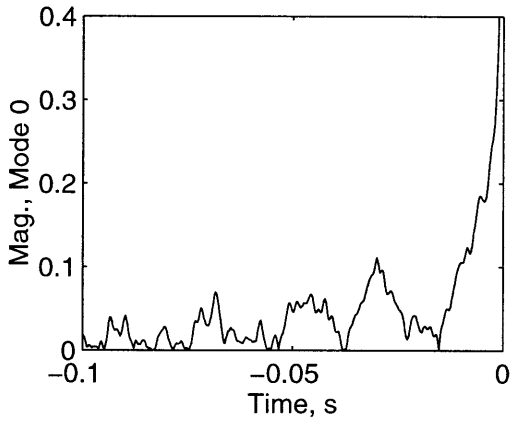

Figure 3.23: Magnitude of 0-mode spatial Fourier coefficient at inlet before surge, 2.14% mean injection case

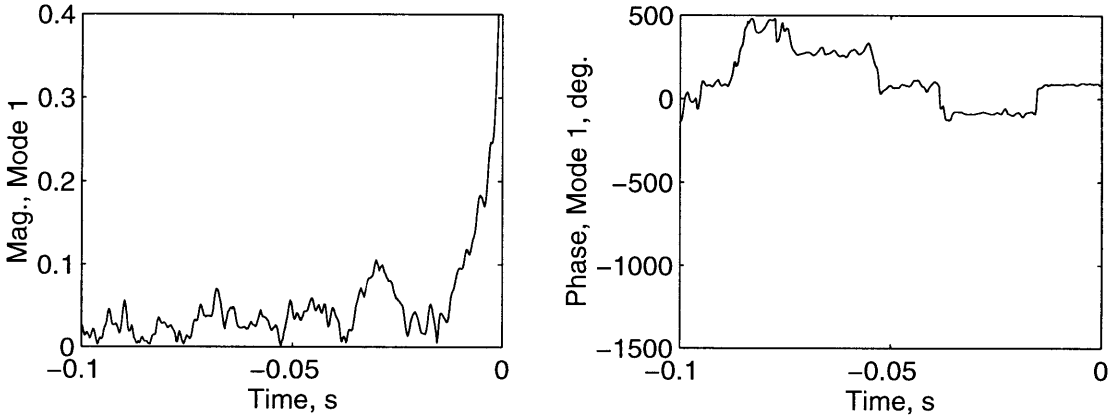

Figure 3.24: Magnitude and phase of 1-mode spatial Fourier coefficient at inlet before surge, 2.14% mean injection case

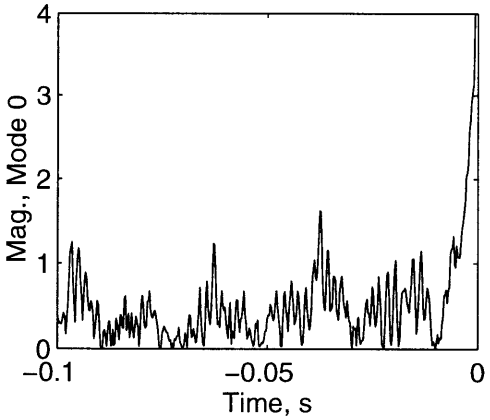

Figure 3.25: Magnitude of 0-mode spatial Fourier coefficient at diffuser exit before surge, 2.14% mean injection case

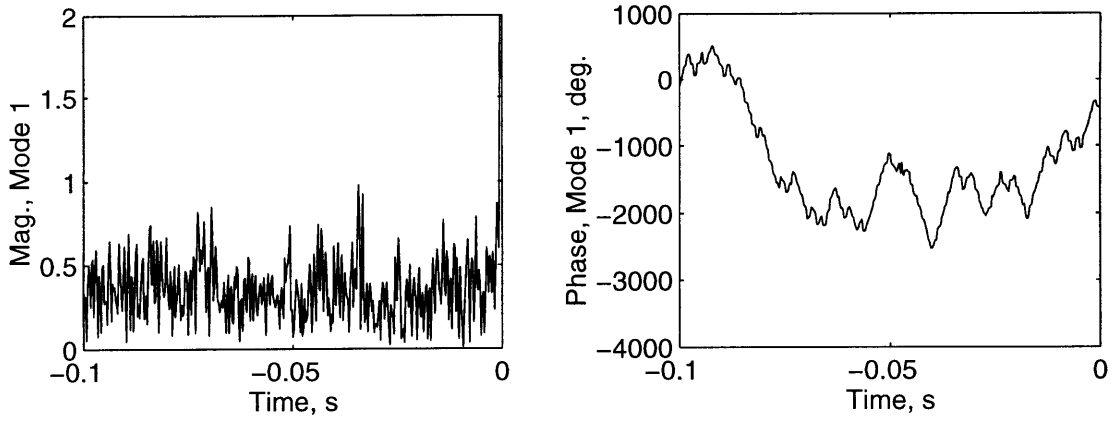

Figure 3.26: Magnitude and phase of 1-mode spatial Fourier coefficient at diffuser exit before surge, 2.14% mean injection case

No significant pre-surge growth is evident for the zero-injection cases shown (Figures 19-22). Zeroth-mode disturbances at the inlet for the mean injection case exhibit steady growth at 0.05 s before surge in Figure 3.23. The first-mode disturbance amplitude (Figure 3.24) seems to grow in a similar fashion to the 1-D amplitude, but the phase indicates that the disturbance is fixed in its spatial orientation, or not rotating. The magnitude is misleading because the first-spatial mode coefficient captures non-uniformities in the inlet flow which can be exaggerated by the 1-D axial flow phenomena. Figures 3.25 and 26 indicate zeroth-mode growth at the diffuser exit occurring only 0.01 s prior to surge and no evidence of first-mode growth. In summary, rotating stall does not appear during instability inception, but the mean injection case exhibits energy growth in the axial mode of unsteadiness 0.05 s prior to surge.

It remains to correlate this frequency content with physical behavior of the engine. The primary spectral peak of interest is 27 Hz, noted as the engine approaches surge. Unsteady mass flow fluctuation is estimated using a calibration with the high-frequency inlet taps and an approximate correction to minimize response to inertial effects (refer to Appendix A for a description). Pressure ratio fluctuations are derived directly from unsteady combustor pressure measurement and the value of atmospheric pressure. Figure 3.27 illustrates a growth of the counterclockwise cycles associated with the prominent peak of 27 Hz energy at 1.5 s prior to surge in Figure 3.18. Such fluctuations are a dynamic instability known as mild surge, and have been observed in several documented studies of high pressure ratio centrifugal

systems. For the LTS-101, these cycles grow and decay in no apparent pattern, and as mentioned earlier, do not linearly grow into deep surge. However, the average cycle amplitude increases as the nozzle area is closed. The next section examines the development of these oscillations.

Figures 3.28 and 3.29 show transition into surge for points with and without injection. Figure 3.28 shows that although the 27 Hz cycles do not grow linearly into surge, this surge is preceded by two large magnitude oscillations similar to those observed in Figure 3.27. Figure 3.29 shows no apparent pre-surge cycle, only random operating point fluctuations. It is hypothesized that surge results from mild surge cycles and/or system noise generating operating point excursions into unstable regimes. It is important to draw the distinction between unstable operating points and the surge line, since excursions may occasionally cross the nominal surge line without precipitating the instability. The surge line is generally a conservative estimate to compressor stability which takes into consideration normal unsteady operating point fluctuations. Unstable operating points, in this context, represent conditions where surge is inevitable.

The 68 Hz peak is less understood. The first attempt to identify the origin of these oscillations was to create time plots at each axial sensor location. Figure 3.30 shows data which was bandpass filtered in the range of 60-75 Hz, isolating the 68 Hz behavior. For the throat, vane plenum, and diffuser exit sensor locations, the same vane passage was chosen to eliminate misleading data from possible circumferential non-uniformities. Combustor pressure waves lead the other sensors in phase, suggesting that the disturbance originates at this location. The oscillations consistently attained their largest magnitudes when the phase relationship between axial locations was near that observed in the last time steps of Figure 3.30. The oscillations decayed as this phase relationship deteriorated. This behavior suggested that the 68 Hz phenomena was system related as opposed to being isolated to a single component. A phase mismatch was often seen to develop near the throat and vane plenum taps, indicating interaction between the injection feed plenum and compression system dynamics.

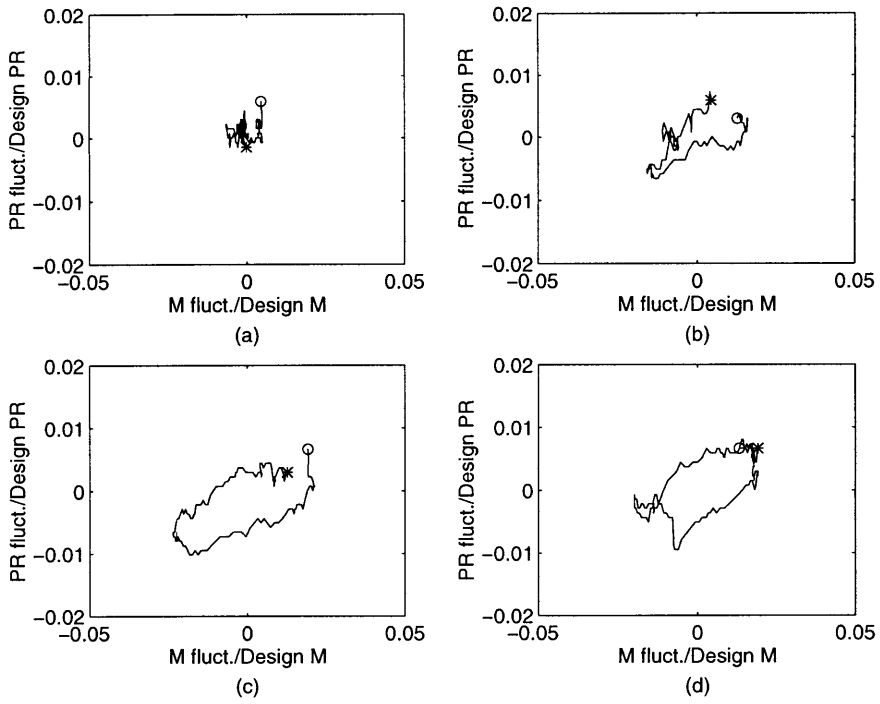

Figure 3.27: Evolution of 27 Hz mild surge oscillations during 2.14% m_{des} injection in 0.04 s increments. Operating point traces begin at '∗' and end at 'o'.

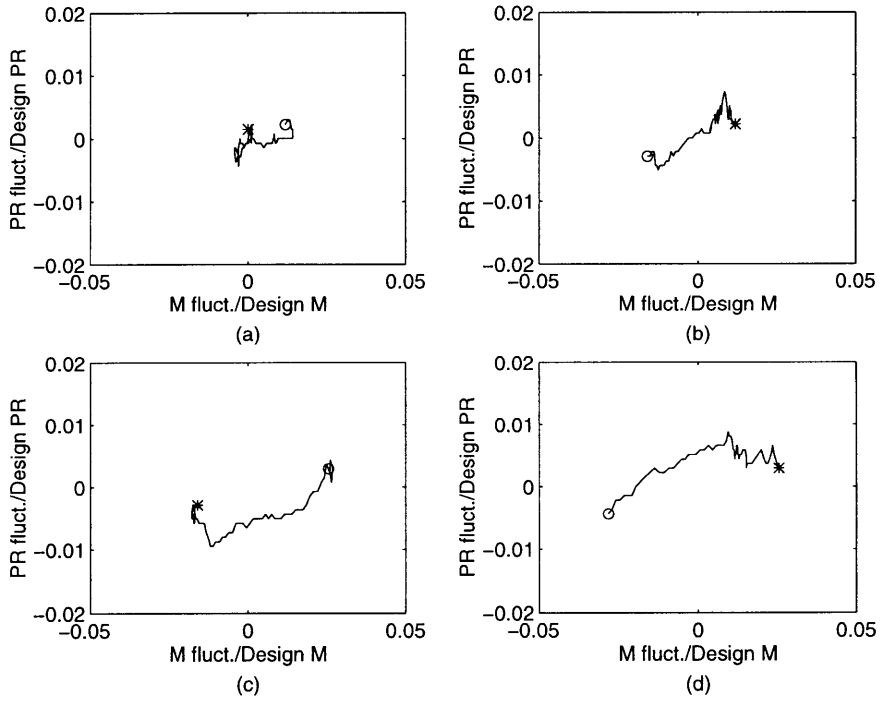

Figure 3.28: Evolution of 2.14% mean injection case into surge in 0.02 s increments. Operating point traces begin at '∗' and end at 'o'.

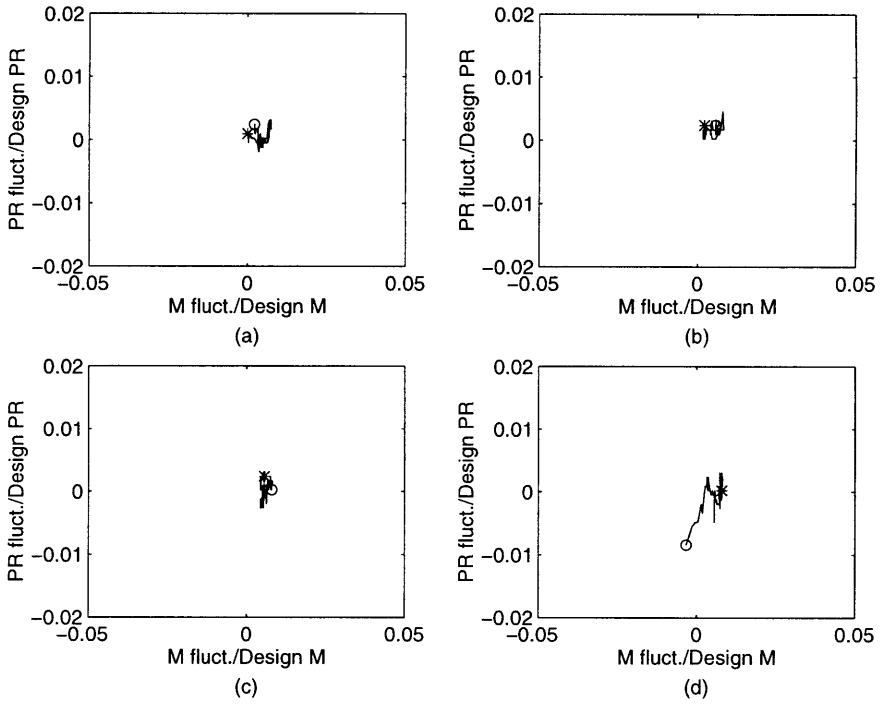

Figure 3.29: Evolution of zero-injection case into surge in 0.02 s increments. Operating point traces begin at '∗' and end at 'o'.

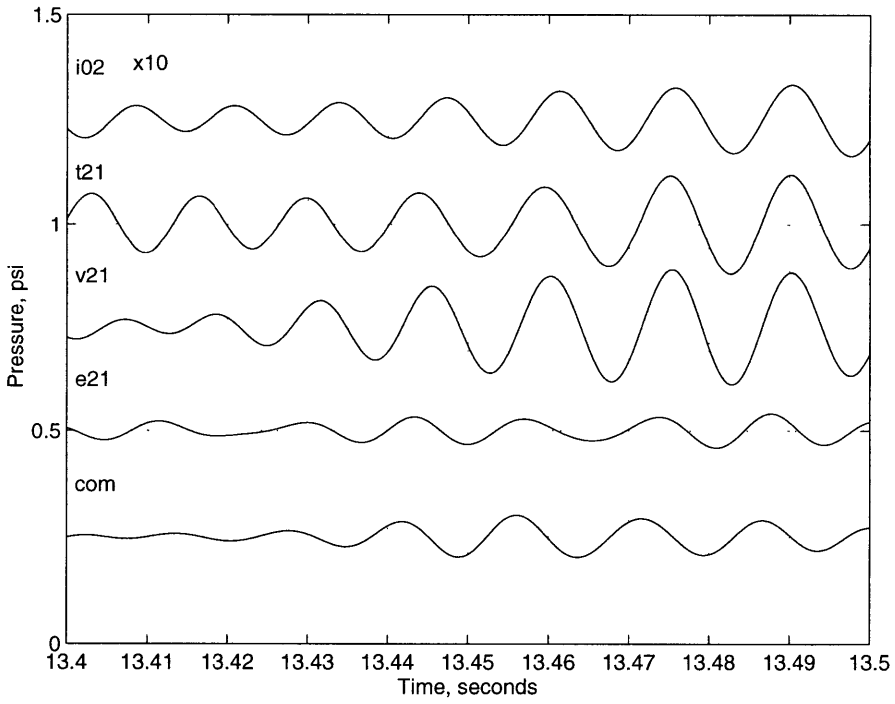

Figure 3.30: Pressure traces of inlet (i02), diffuser throat (t21), vane plenum (v21), diffuser exit (e21), and combustor (com) during 68 Hz oscillations. Band pass filtered between 60-75 Hz.

Since it appears combustor oscillations supply the energy to the observed oscillations, it was of interest to examine the frequency response of other sensors to the "forcing". Figure 3.31 shows the frequency response estimate between combustor and inlet tap pressures. Treating the natural combustor oscillations as the forcing function, the computational method described for forced response testing in Chapter 4 was utilized for this estimate. Note the 4 dB amplitude increase and the phase change between 60-70 Hz. At standard atmospheric conditions, not accounting for the elevated speed of sound in high temperature regions of the compressor ducting, the 140° phase lag at 68 Hz corresponds to a wave traveling 6.5 ft. Since this is significantly longer than the flow path length between the two sensors, a purely acoustic phenomena was dismissed as an explanation for this behavior. An acoustic phenomena would exhibit a much smaller phase lag between the sensors.

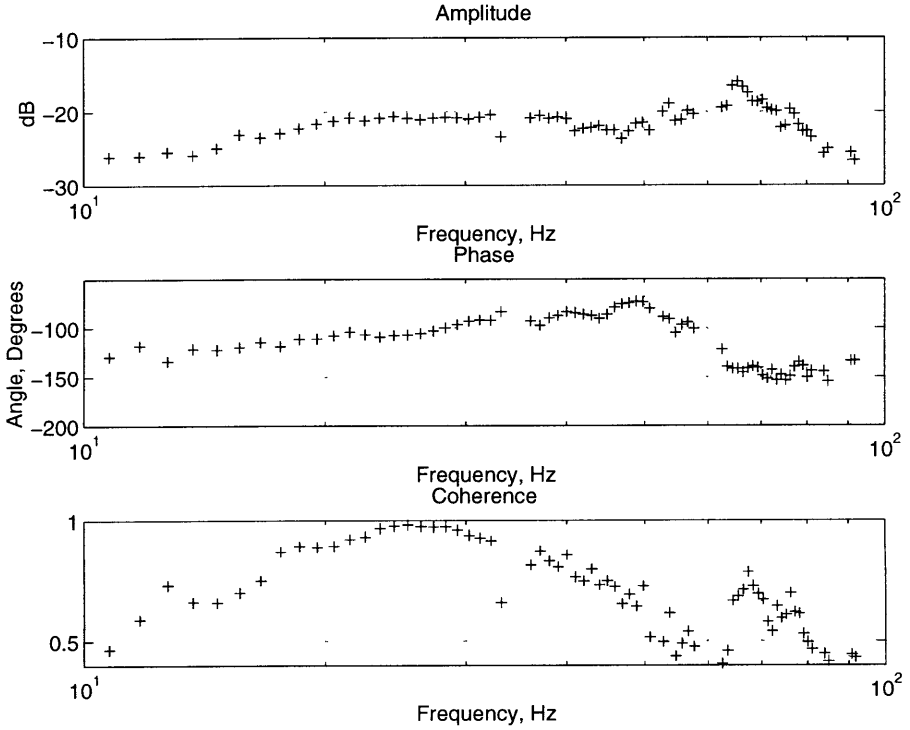

Figure 3.31: Frequency response estimate of inlet pressures to natural combustor pressure forcing

Because this phenomena appeared to be system related and linked to phase behavior near the injection slots, a lumped parameter model was created to examine the interaction of the injection plenum with the gas generator. The model was based upon the dynamic model

presented in [22] and is described in Appendix B. The key element is the addition of a volume to the downstream compressor ducting immediately following the actuator disk representing the compressor's total pressure rise. Assuming that the feed system inertia was negligible, flow into and out of the volume was modeled as a quasi-steady throttle relation driven by the static pressure difference between the feed plenum and vane passage. This lumped parameter model was unsuccessful in duplicating the frequencies of mild surge and the 68 Hz oscillation, even with liberal adjustments in the geometric parameters. However, the modeled phase relationships between sensors was similar to experimental observations.

Transfer functions of inlet mass flow, inlet static pressure (just upstream of the compressor actuator disk), and combustor pressure under forcing by combustor pressure noise (additive to the basic combustor pressure term) are shown in Figure 3.32. The frequencies are non-dimensionalized by the resulting mild surge frequency of the model. As mentioned above, the correct frequencies are not captured by the lumped parameter model, nor is the correct ratio between the mild surge and second calculated resonant peak, appearing at 5.3 f_{surge}. However, the phase relationships are consistent with observed behavior. Note the phase relationship between $p_{s,2}$ and m_{inl} varies from 180° at low frequencies, where Bernoulli's equation predicts static pressure to be opposite in phase to velocity changes, to 270° at high frequencies, where the unsteady effects addressed in Appendix A add additional lag. Also note that m_{inl} leads p_b by 90° at the mild surge frequency, consistent with a Helmholtz oscillation. The best evidence that the model captures the probable cause of the 68 Hz phenomena is Figure 3.33 when compared to the results of Figure 3.31. A frequency response of p_{inl} to the resulting p_b (not $p_{b,noise}$) was created from the results of Figure 3.32. The amplitude peak appears at the second resonance frequency, and the phase behavior is qualitatively similar, slowly rising to near the resonant peak and then falling off. The phase similarity of this model to the experimental behavior leads to the conclusion that the feed plenum volume interacts with the compression system to introduce the 68 Hz system mode.

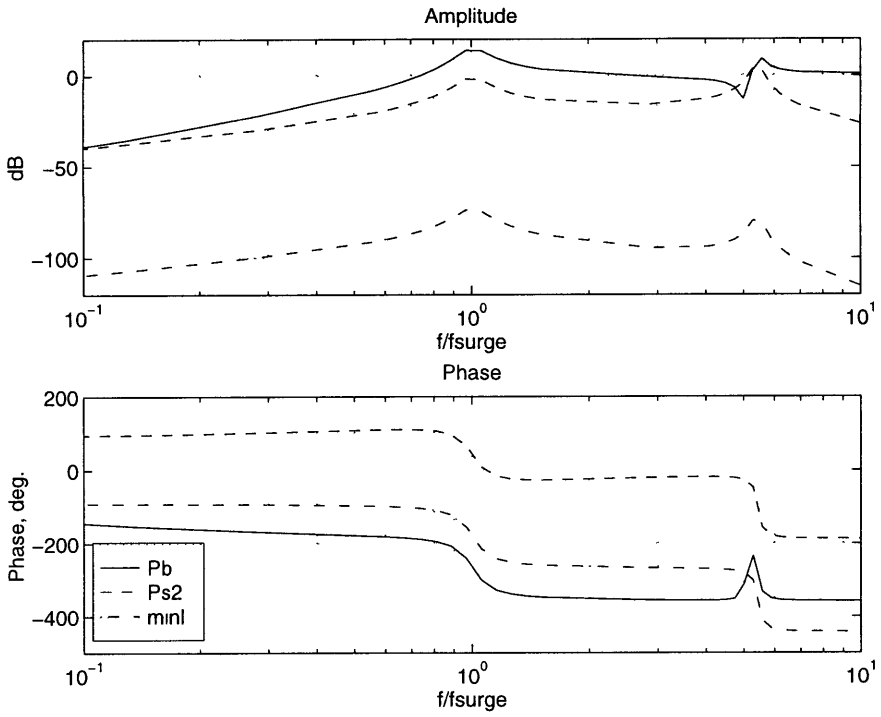

Figure 3.32 : Transfer function estimates of combustor pressure (p_b), inlet static pressure ($p_{s,2}$), and inlet mass flow (m_{inl}) to combustor pressure noise generated from linear, lumped parameter model

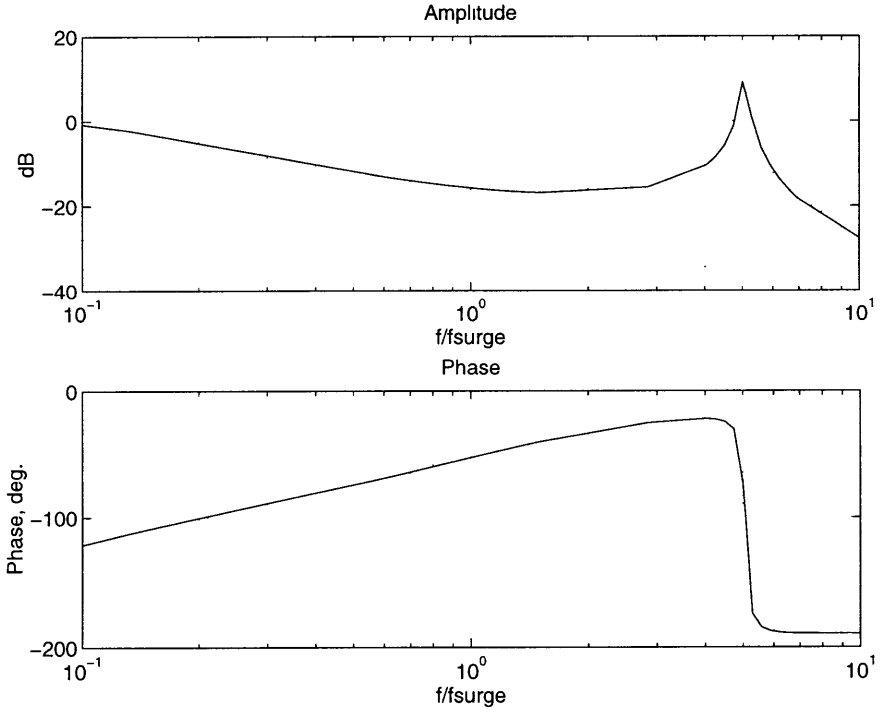

Figure 3.33: Transfer function between combustor pressure and inlet static pressure from linear, lumped parameter model

Several invariant peaks, appearing clearly at all operating points, are tap acoustic resonances. These signals appear prominently, such as in the vane plenum spectrums, and may exhibit slight frequency variation between taps at the same axial location. The signals do not pertain to engine dynamics and, therefore, corrupt accurate measurements. Borror experimentally determined that 6.75 in. taps of similar geometry exhibited a 420 Hz resonance at room temperature [24]. Equation 3.5 shows the proportionality of tap resonance frequency to temperature and tap length. Based upon this relationship and Borror's experimental results, Table 3.5 shows estimated versus actual tap resonance frequencies.

$$f \propto \frac{\sqrt{\gamma R T_{tap}}}{L_{tap}} \propto \frac{\sqrt{T_{tap}}}{L_{tap}} \tag{3.5}$$

Location	Length, in.	T_{tap}, °R	$f_{predicted}$, Hz	f_{actual}, Hz
Borror's Rig	6.75	~530	N/A	420
Inlet	11	520	255	250
Diffuser Exit	4.5	700-1000 (est.)	724-865	610
Vane Plenum	6	700-1000 (est.)	543-649	555

Table 3.5: Estimated versus actual probe resonance frequencies

A range of T_{tap} values for the diffuser exit and vane plenum taps were chosen due to uncertainty in these parameters. The taps are exposed to the high compressor exit temperature but are cooled near the Kulite transducer by a water jacket. The agreement at diffuser exit is poor, but its spectral characteristics are similar to those of the other taps. Slight leakage or difference in geometry could account for the discrepancy. Therefore, the author still attributes this frequency to a probe resonance.

3.3 Non-linear Model Comparison

It was hypothesized that the existence of large, mild surge oscillations could be attributed to the change in characteristic shape created by injection. In assessing this hypothesis, a non-linear simulation developed by Dr. Laurence Didierjean and utilizing the system equations derived by McNulty [22] was utilized. Inherent in the equations is the assumption of

isentropic plenum processes. The system equations and non-dimensionalization are provided below.

$$\frac{dW_c}{d\tau} = \beta \frac{(I_l + 1)}{(p_c I_l + 1)} \left(\pi_c - p_b^*\right) \tag{3.6}$$

$$\frac{dp_b^*}{d\tau} = \frac{1}{\beta}\left(W_c + W_{inj} - W_{turb}\right) \tag{3.7}$$

$$\beta \equiv \frac{1}{\sqrt{\gamma T_b^*}} \sqrt{\frac{V_b}{A_c (L_u + L_d)}} \tag{3.8}$$

$$I_l \equiv \frac{L_u}{L_d} \tag{3.9}$$

$$W_{inl,turb,\text{ or } inj} \equiv \frac{\dot{m}_{inl,turb,\text{ or } inj} \sqrt{RT_{amb}}}{p_{amb} A_c} \tag{3.10}$$

$$p_b^* \equiv \frac{p_b}{p_{amb}} \tag{3.11}$$

$$T_b^* \equiv \frac{T_b}{T_{amb}} \tag{3.12}$$

$$\tau \equiv \omega_H t \tag{3.13}$$

The purpose of this simulation was to examine qualitative differences in behavior driven by two different compressor characteristic shapes. The work of McNulty [22] and the efforts with the linear, lumped parameter model found in Appendix B indicate the difficulty in using the physical dimensions of the LTS-101 in mathematical simulations to match experimental results. Therefore, engine parameters were chosen to exhibit natural oscillations near 30 Hz to approximate the behavior observed in experiment.

$$\beta = 1.5 \tag{3.14}$$

$$I_l = 4 \tag{3.15}$$

$$\omega_H = 76 \text{ Hz} \tag{3.16}$$

Process unsteadiness was simulated by injecting normally distributed p_B noise into the system equations. A small time step Euler integration scheme was utilized to evaluate the system response. Qualitatively, operating point fluctuations were insensitive to the level of noise and time step chosen. However, the magnitudes were influenced by these parameters.

Figure 3.34 illustrates the compressor characteristics used in the simulations. Each characteristic was a combination of curve fits found in Table 3.1 and a steep, positively sloped region to the left of the surge point. The operating points are indicated by asterisks and labeled with letters. Initial condition 'b', was selected as the highest flow rate (to 0.1% m_{des}) which resulted in surge. A stable initial condition at 1.0% m_{des} higher flow, 'a', was selected for comparison.

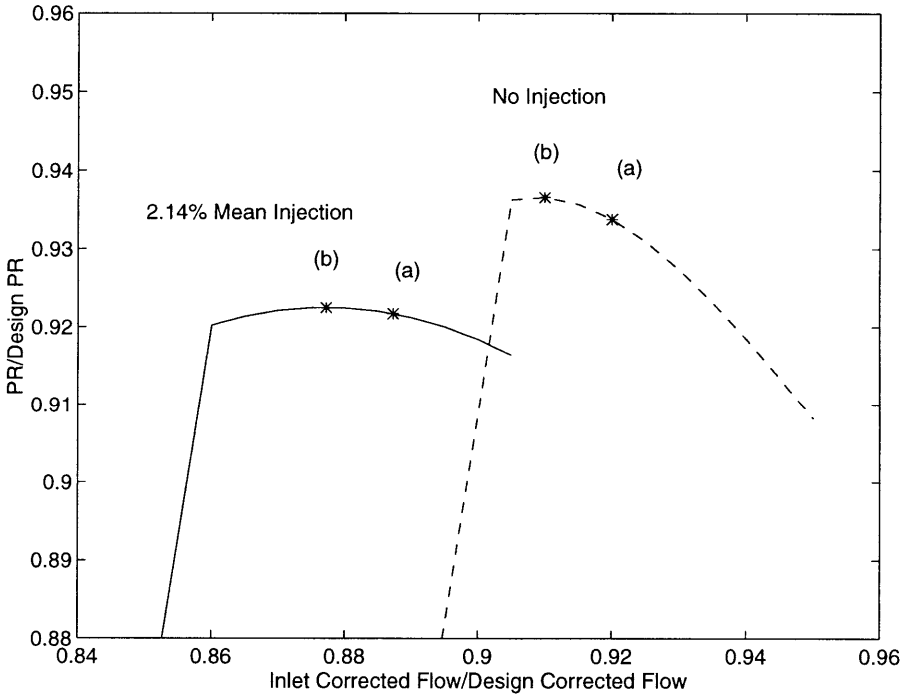

Figure 3.34: Compressor characteristic speedlines used in simulation with operating points identified by stars and letter labels.

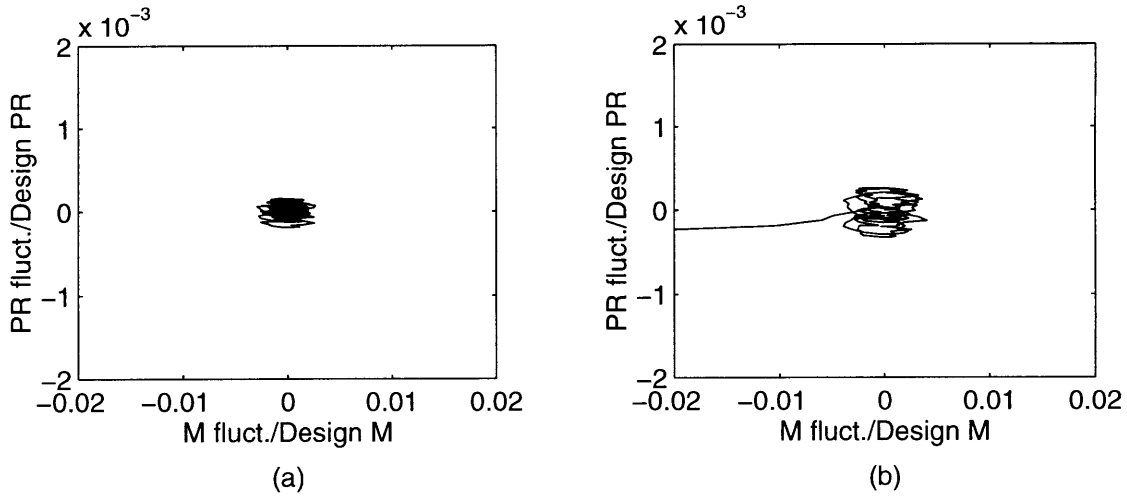

Figure 3.35: Zero injection operating points shown on Figure 3.29. $m_{inl,corr}/m_{des}$: (a) 0.920, (b) 0.910.

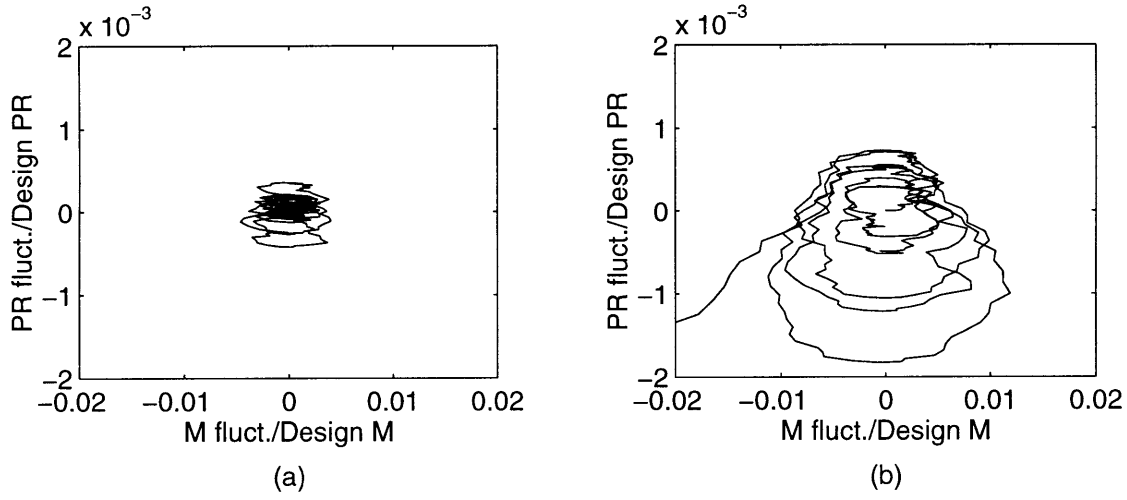

Figure 3.36: 2.14% mean injection operating points shown on Figure 3.29. $m_{inl,corr}/m_{des}$: (a) 0.887, (b) 0.877.

Simulated operating point excursions in the zero-injection case are small when compared to the mean-injection case. There is clear oscillatory phenomena in both, but the surge inception process appears different. Without injection, Figure 3.35, surge occurs with minimal growth in the oscillation cycles, so the influence of system noise seems directly responsible for pushing the operating point into a region of instability. The simulated mean injection case, Figure 3.36, exhibits slow growth in the oscillations around the operating point

until this point crosses into an unstable regime. It is indicative behavior of a growing oscillation.

The general trends of the simulation agree with experimental behavior. Without injection, the engine appears to transition into surge without warning. Perhaps any oscillations present are dominated by process noise. The mean injection case, however, exhibits large scale oscillations as the surge line is approached. This simulation supports the hypothesis that the appearance of large scale oscillations is determined by the characteristic shape. What is not modeled is the damping of these oscillations. The experimentally observed oscillations do not grow steadily in amplitude before surge. Referring back to the experimentally observed oscillations shown in Figure 3.27. The oscillation appears approximately 1.5 s before surge and decays. The surge event which followed, shown in Figure 3.28, resulted from a small scale oscillation cycle growing suddenly into a larger one. The same growth and decay behavior was noted by Tryfonidis [27] in axial compressors as system damping decreased. Furthermore, the simulation predicts that points near the peak of the characteristic continue to grow into surge events. The damping of these oscillations in the gas generator allows operating points to exist in positively-sloped regions without surging. In engine operation, the average oscillation amplitude increases as the operating point is throttled toward surge, but sustained growth is not observed.

3.4 Summary

Steady air injection at the diffuser throat was shown to change steady and unsteady behavior of the AlliedSignal LTS-101 gas generator, especially near surge. Effects of injection, including pressure loss, cycle temperature changes, and a large displacement of inlet mass flow, are interrelated by the requirement to maintain constant turbine inlet corrected flow. This requirement is dictated by matching the gas generator to a downstream choked nozzle of given area. Injection allows this area to be reduced, extending the gas generator's operating range to lower turbine corrected flow than attainable without injection. It is hypothesized that fluid dynamic effect of injection stabilizes the vaned diffuser, the

destabilizing element of the compression system, allowing surge-free operation at these reduced flows.

95% $N_{1,corr}$ speedlines near peak pressure rise were experimentally generated both with and without injection. Mean injection creates a large region of approximately zero slope near the peak of the characteristic. Through experiment and simulation, this change in characteristic shape allows the formation of mass flow and pressure ratio oscillations near 27 Hz known as mild surge. These oscillations play a role in surge initiation for the mean injection case, but they do not steadily increase in amplitude as predicted by simulation. Process noise appears to control surge inception for cases without injection, and the instability appears with negligible pre-surge warning. A 68 Hz mode, appearing with mean injection, was attributed to the interaction of actuator plumbing with the overall compression system dynamics. A linear, lumped parameter model, including a feed system volume, closely matched the phase behavior between combustor and inlet pressure sensors observed experimentally and lead to this conclusion. All of the oscillatory behavior observed in the engine was 1-D in nature, with no evidence of a first-mode circumferential component.

Chapter 4: Forced Response and Control Experimentation

The previous chapter investigated the naturally excited dynamics of the LTS-101 gas producer. This chapter examines the system's forced response to modulated diffuser throat air injection, particularly at frequencies near naturally occurring resonant peaks. The frequency response estimates are used to assess injection's effectiveness and determine a viable feedback sensor for use in closed loop operation. A transfer function is estimated from forced response data for use in control law design, and preliminary closed loop experiments are presented.

4.1 Forced Response System Identification

The block diagram for forced response testing is shown in Figure 4.1. The objective is to estimate the engine dynamics from a known input, valve command, and measurements of the output, average pressure signals at a given axial location.

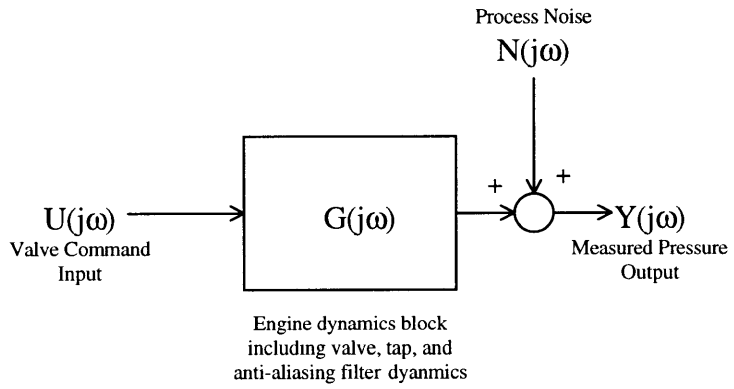

Figure 4.1: Block diagram for forced response testing

The engine dynamics block may be divided into the separate frequency response characteristics of its components: valve, tap, and anti-aliasing filter dynamics. However, this testing was intended to be an expedient, intermediate step to control law design and evaluation. Therefore, these items are combined in the overall plant dynamics. Each axial location of sensors yields a G(jω) estimate of the pressure response dynamics. As mass flow is re-

duced, system modes may become lightly damped, causing resonant peaks of engine pressure and flow oscillation to appear. The frequencies which appeared under natural excitation were of particular interest in the forced response experiments.

Forced response estimates can be derived from power spectral density calculations. If the noise (see Figure 4.1) is uncorrelated to input forcing, an estimate is calculated using the equation below [28].

$$G(\omega) = \frac{S_{yu}(\omega)}{S_{uu}(\omega)} \tag{4.1}$$

Estimate quality is described by the coherence function, $\gamma_{uy}(\omega)$, which yields values from 0 to 1. At a particular frequency, values near 1 indicate that there is a causal relationship between the forcing and output signal and that the output is not contaminated by process noise [28].

$$\gamma_{uy}(\omega) = \sqrt{\frac{\left|S_{uy}(\omega)\right|^2}{(S_{uu}(\omega))(S_{yy}(\omega))}} \tag{4.2}$$

A frequency response estimate near the surge line was desired, posing a difficult experimental problem. A minimum level of modulated injection is required to overcome the noise floor of the engine's natural unsteadiness and elicit a coherent output response. Unfortunately, high levels of forcing at lightly damped operating points can precipitate surge. A viable combination of operating point and forcing magnitude was chosen by trial and error, utilizing a spectrum analyzer to monitor the magnitude of modal activity as an indication of proximity to surge. For the frequency response data which follows, the operating point (with 2.14% m_{des} mean injection) is 0.851 $m_{inl,corr}/m_{des}$, and the amplitude of valve command modulation is ±1 V, corresponding to injection fluctuations of ±0.15% m_{des} during low frequency forcing.

Two methods of forcing the engine were attempted. First, 0-400 Hz linear frequency sweeps of constant amplitude sine waves were applied as the valve command signal. Several sweep durations were attempted, and multiple sweeps were collected on a 45 s high-frequency data set. Coherence was poor over the entire range of frequencies, regardless of forcing am-

plitude. It was apparent that discrete frequency forcing would be required to yield coherence levels near 1. A programmable function generator supplied a succession of 3, 15 s sine wave sets of specified frequency to the valve controller. Again, data was collected in a 45 s data set. 21 whole number frequencies were chosen to span the desired range, 15-375 Hz, and to focus in regions of particular interest, near 27 and 68 Hz. After experimentation, it was realized that a coherence improvement could have been realized by choosing forcing frequencies which exactly matched values utilized in the spectral decomposition algorithm. Future experimentation should utilize these frequencies, which occur at increments of $f_{resolution}$ (defined by equation 3.5) in the range of 0 Hz to the Nyquist frequency of data sampling.

Figures 4.2-6 are the experimental, open-loop, frequency response estimates for output from each of the five axial pressure tap locations. The middle 13 s of each 15 s sample (chosen to avoid frequency transition regions in the data sets) was processed by MATLAB's spectrum.m function. Using the valve command voltage as the input and the average of each axial location's pressure taps as the output, spectrum.m performed power spectral density computations and the calculations described in equations 4.1 and 4.2. Hanning windows of 16384 data points (4.096 s) with an overlap of 8192 (2.048 s) were used for the FFT evaluations within the algorithms. Forcing and response data at each frequency were combined to generate a plot over the desired frequency range. For each axial location, a threshold level of coherence (shown as the lower y-axis scale in the (c) plots of Figures 4.2-6) was selected to delineate acceptable points. The values reflect a compromise between coverage of the desired frequency range and confidence in the response data. Local dynamics and signal to noise ratios differ between axial stations, altering attainable coherence levels.

The inlet taps of Figure 4.2 exhibit the most favorable combination of visible engine dynamics and coherence out of the 5 axial locations. Since the dominant effect of injection is the displacement of inlet mass flow, this result is not surprising. Clear peaks near 30 and 70 Hz represent the engine's response to forcing near the mild surge and injection plenum interaction frequencies examined in Chapter 3. Peaks near 250 Hz and 310 Hz represent an inlet tap resonance and the natural frequency of the valve dynamics, respectively.

All other axial locations indicate 30 Hz forcing with a high level of coherence. However, each location has limitations. Figure 4.3 indicates diffuser throat sensors lose coherence near 70 Hz and high frequency magnitudes are poorly resolved. Figure 4.4 shows the excellent coherence of the vane plenum taps, but this response is more associated with their being closely-coupled with the actuator as opposed to indicating an engine system response. Take, for example, its clear resolution of the 310 Hz resonant peak associated with the valve dynamics. Figures 4.5-6 show the diffuser exit and combustor taps, which exhibit nearly identical response estimates due to their proximity to one another. Injection appears to have little, if any, coherent influence beyond 40 Hz. It is believed that the forcing magnitude is too small to elicit a response of suitable signal to noise ratio near the combustor. The phase lead which appears at low frequencies in these estimates is misleading as to the speed of response of combustor pressure to injection. Recall that injection causes a loss in total pressure ratio. The 130° phase lead at low frequencies is associated with a pressure peak in the combustor, so the pressure trough, the actual effect of injection, lags the valve command by 50°.

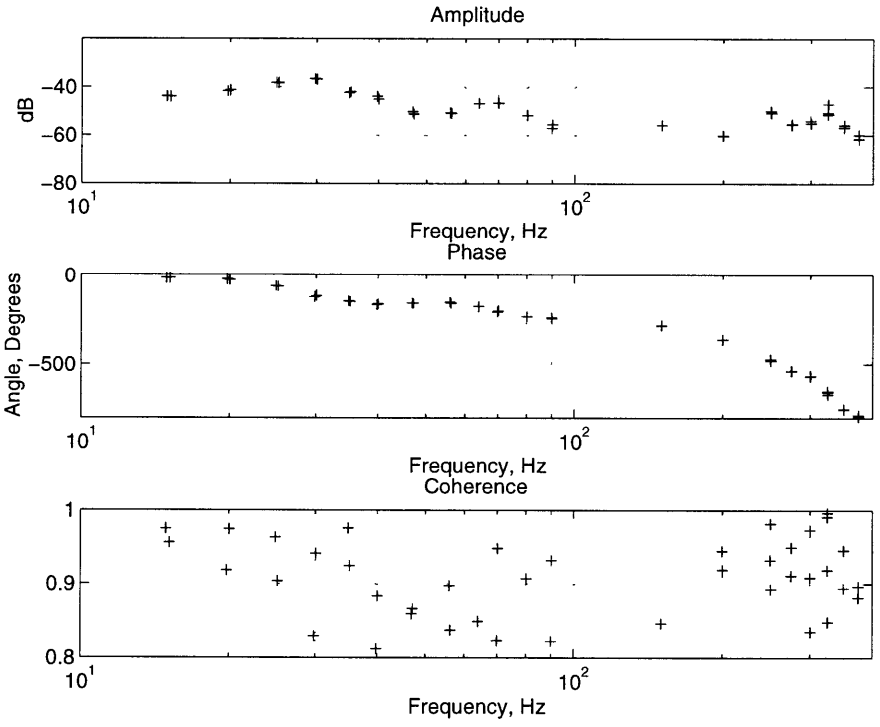

Figure 4.2: Experimentally determined frequency response for valve command voltage to averaged inlet pressure (max. f = 400 Hz)

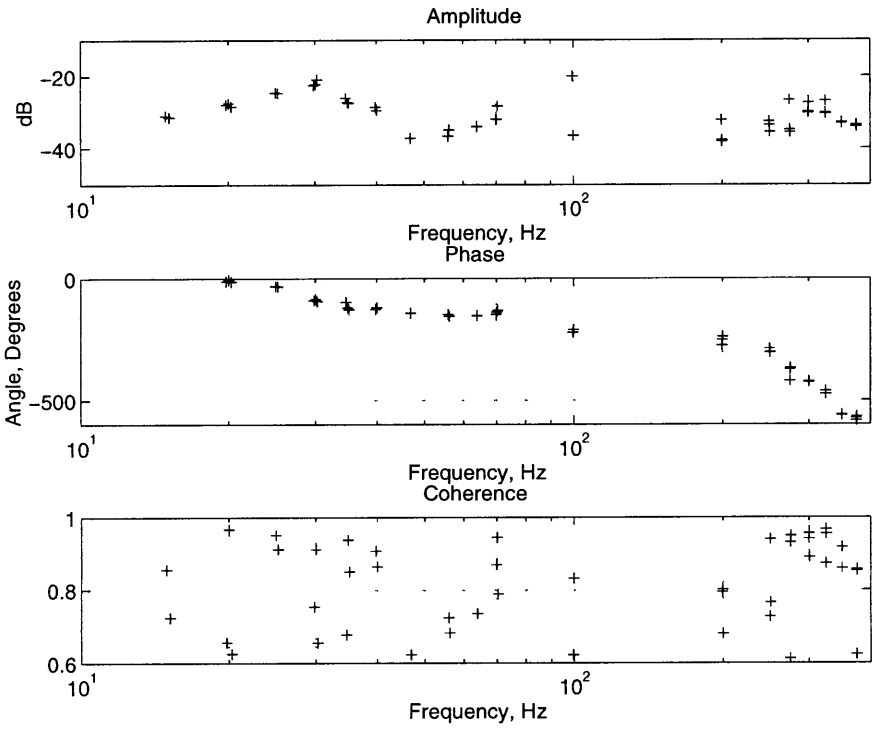

Figure 4.3: Experimentally determined frequency response for valve command voltage to averaged diffuser throat pressure (max. f = 400 Hz)

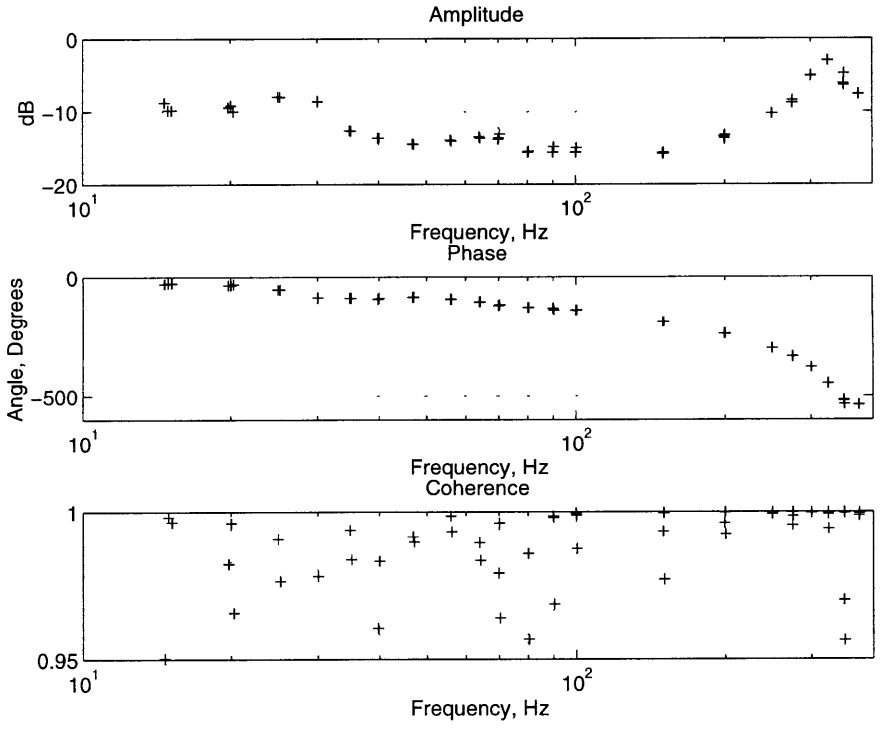

Figure 4.4: Experimentally determined frequency response for valve command voltage to averaged diffuser vane plenum pressure (max. f is 400 Hz)

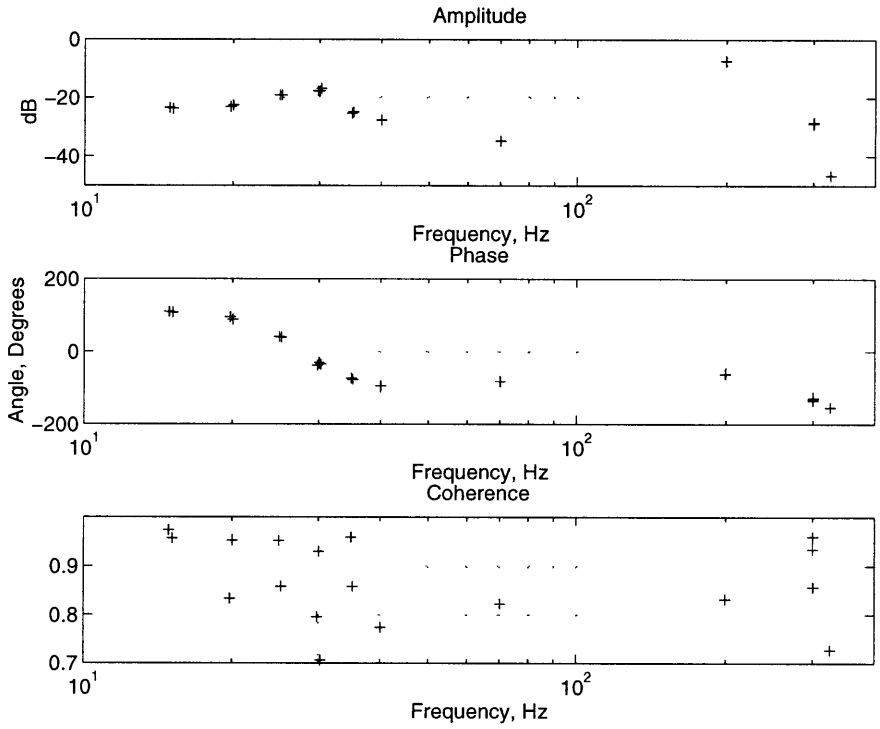

Figure 4.5: Experimentally determined frequency response for valve command voltage to averaged diffuser exit pressure (max. f = 400 Hz)

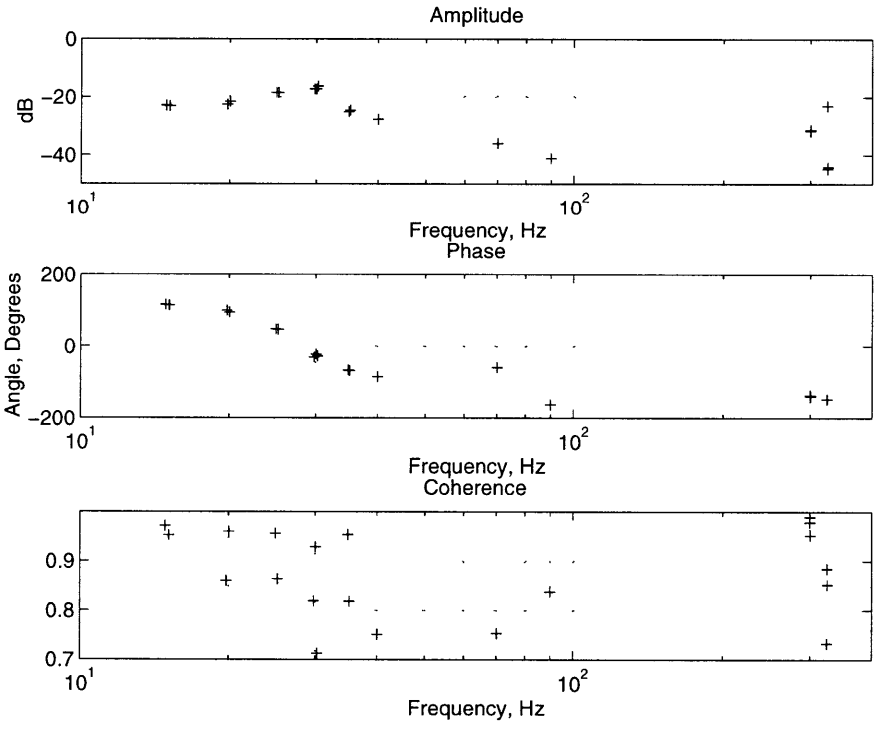

Figure 4.6: Experimentally determined frequency response for valve command voltage to combustor pressure (max. f = 400 Hz)

The inlet taps' resonant response to forcing at the system modes (27 and 68 Hz) indicates that the air-injection actuator has control influence at these modal frequencies. Since sensors at the remaining locations do not indicate other prominent system modes, it can be concluded that the inlet taps exhibit good observability of the dominant system dynamics. Therefore, inlet taps were chosen to be the regulated variable for linear control system design. This choice agrees with the conclusions of McNulty [22] and Simon [23] that sensing within the upstream duct is optimal.

For control design purposes, a pole-zero expression of the forced response estimate was needed. MATLAB's invfreqs.m routine was utilized to generate a transfer function fit to the forced response data. Weighting of experimental values (an option of the infreqs.m routine) was utilized for optimizing the fit. The lowest order system which generated an acceptable fit of magnitude and phase included 10 poles and 4 zeros. Table 4.1 gives the location of each pole and its damping ratio. Figure 4.7 shows the transfer function fit along with the highest coherence data point at each forcing frequency. This fit is slightly different from the system identification used in control law design activities. However, the primary difference, an increase in damping of the 219 Hz pole, was negligible with respect to the root loci for the various controllers. The stability of this pole was of little concern, so controller dynamics never interacted strongly with it. In the next section, predicted control law effectiveness is examined with regard to the fit described below.

POLES	**Frequency, Hz**	**Damping Ratio, ς**	**Description**
-29.6054 ± 178.1544i	28.354	0.1639	Mild Surge
-50.2294 ± 420.7048i	66.957	0.1186	Inj. Plen. Influence
-1010.4099 ± 1379.9890i	219.632	0.5908	Unknown
-137.5689 ± 1531.9563i	243.818	0.0894	Tap Resonance
-63.5187 ± 2060.2318i	327.896	0.0308	Valve Resonance
ZEROS	**Frequency, Hz**	**Damping Ratio, ς**	**Description**
-93.2847 ± 336.6721i	53.583	0.2670	-
1057.4037 ± 535.0010i	85.148	-0.8923	-

Table 4.1: Pole and zero locations for transfer function fit to frequency response data, valve command voltage to average inlet static pressure

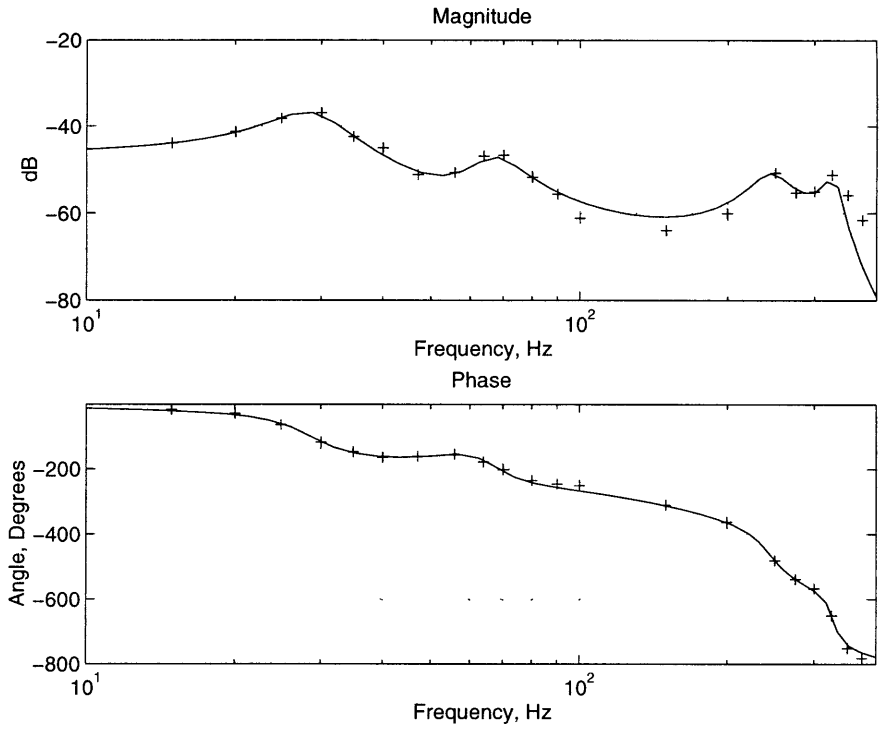

Figure 4.7: Transfer function fit of valve command to average inlet static pressure; high coherence experimental points shown as '+' at each forcing frequency (max. f = 400 Hz)

This single operating point system identification cannot provide information concerning pole migration toward instability. Experimental results indicate that both the mild surge and injection plenum interaction poles exhibit a decrease in damping as the engine is throttled. The model described in Appendix B exhibits this behavior as both the mild surge and injection plenum interaction poles migrate toward instability as mass flow decreases (see Figure 4.8). The surge poles approach instability more rapidly, but movement in the plenum interaction poles suggests that their influence should be addressed in control schemes. This mode may have precipitated a surge during a closed-loop forced response test. 64 Hz forcing was accompanied by large oscillations in its subharmonic at 32 Hz (see Figure 4.9). Although not appearing to go unstable itself, a possible explanation is that the amplitudes present were sufficient to trigger mild surge, which is capable of developing into deep surge.

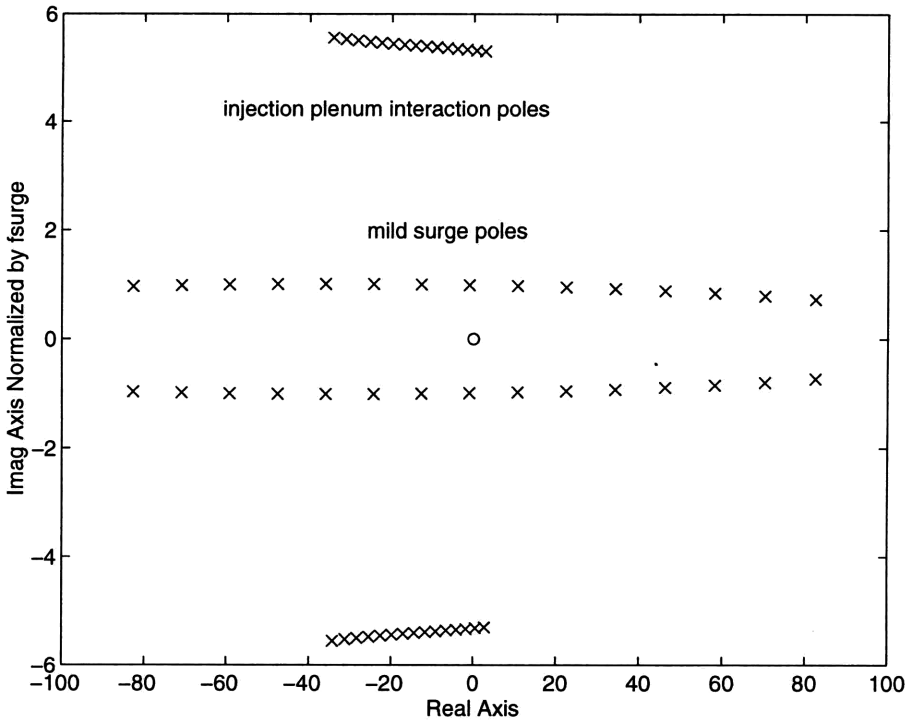

Figure 4.8: Pole-zero migration with throttle closure for simulation including injection plenum system interaction

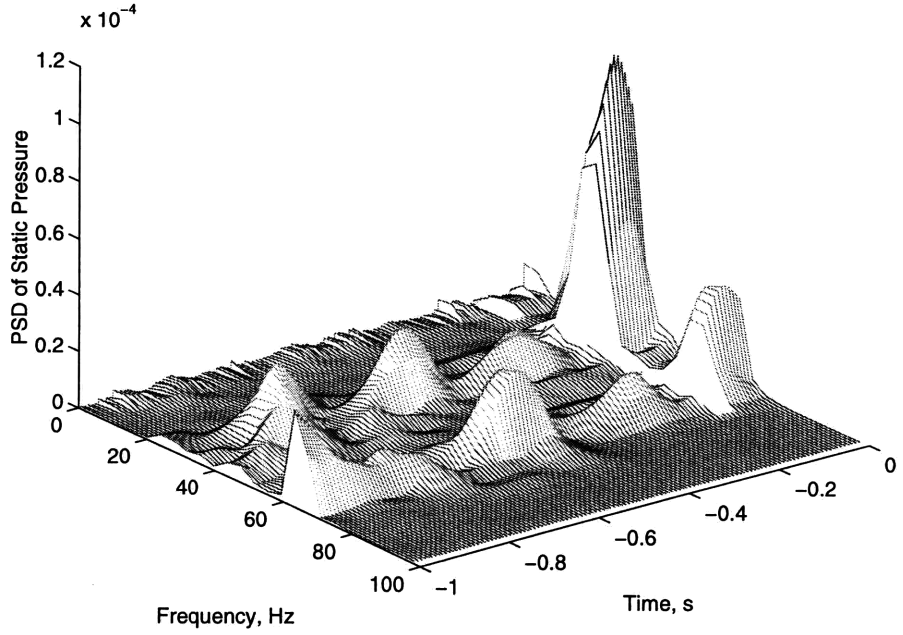

Figure 4.9: Surge during closed-loop forced response testing at 64 Hz valve modulation.

4.2 Control Algorithm Testing

This section documents the preliminary evaluation of several linear control law designs. It presents the control algorithms and the results of their experimental implementation. It is not the intent of this section to delve deeply into the design process of each algorithm, but merely evaluate their effects on the dynamics of the engine. Credit is owed to three individuals for the design work: Professor James Paduano for the classical bode-designed compensator, Dr. Harold Wiegl for the H_∞ compensator, and Dr. Laurence Didierjean for the lead-lag compensator and assistance in coding the various control laws.

The control problem was formulated as a regulator design, as shown schematically in Figure 4.10, and was based upon a system identification similar to that discussed in the previous section. The goal was to utilize modulated diffuser throat air injection to maintain a stable output response of the inlet static pressure taps. Inlet pressures were averaged and processed by a FORTRAN code executing on a dedicated control law computer (details of the experimental setup may be found in Chapter 2). The experimental procedure was to close the variable-area nozzle in small increments, moving the operating point toward the surge line, while the system was under closed-loop operation. Since it was necessary for the control algorithm to remain insensitive to shifts in the mean value of inlet pressure, the average pressure signal was filtered by a digital, 5 Hz, high-pass filter whose bode plot is shown in Figure 4.11. The resulting signal was then processed by the discrete, state space control algorithm and multiplied by a gain. This output, a valve position request, was converted to a command voltage by a D/A board and then sent to the valve controller. Control law gain values could be changed by interrupting control law operation, entering a new gain, and restarting closed-loop operation. This tuning operation was performed at operating points which were stable with constant, mean-injection but near enough to the surge line to exhibit free-response modal activity at 27 and 68 Hz. The frequency content of an inlet probe was constantly monitored on a spectrum analyzer. Control law gain adjustments were made to decrease system modal amplitudes observed on this monitored tap. Gains yielding maximum modal attenuation were chosen as optimal. In order to preclude surges during gain adjustments, the valve command defaulted to a mean-flow, neutral command position.

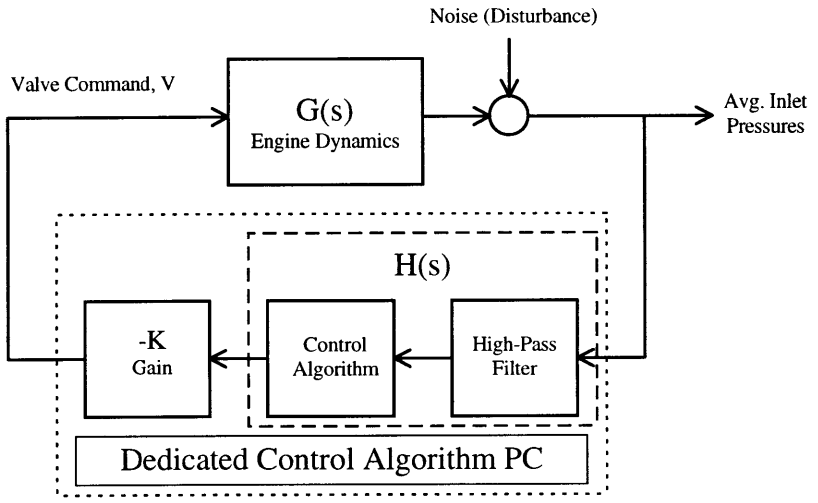

Figure 4.10: Control law block diagram

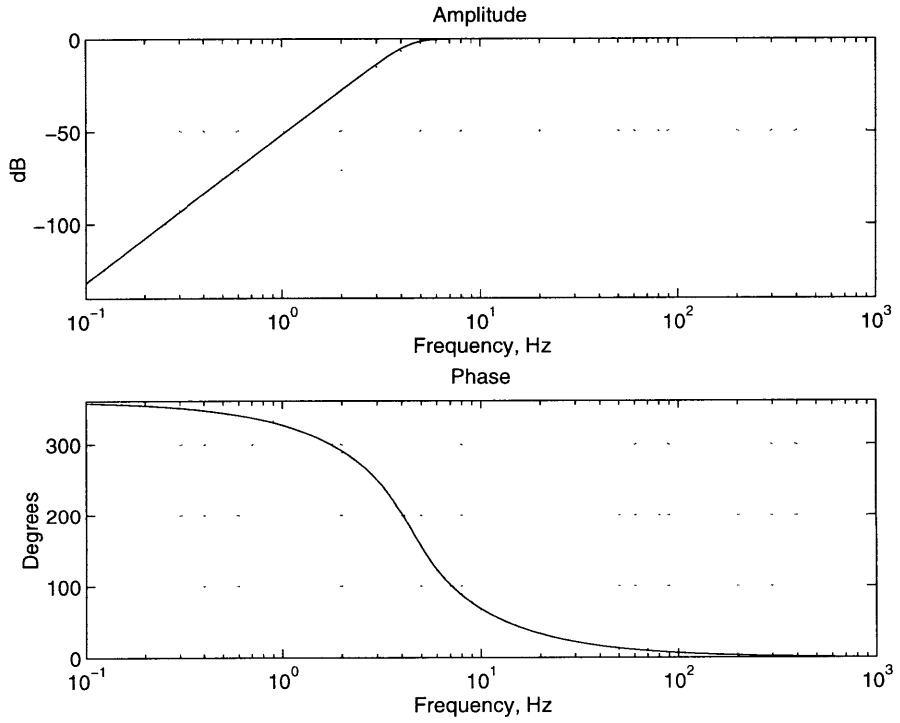

Figure 4.11: 5 Hz, digital high-pass filter bode plot

A bode plot of the open-loop transfer function, KG(s)H(s), and a closed-loop root locus is presented for each control law design. The open-loop transfer function represents the control law's effect on system dynamics in response to disturbances of various frequencies.

The gain of the bode plots for all four controllers are normalized to 0 dB at 10 Hz and plotted using the same scale to facilitate comparison. These plots include the influence of the high-pass filter dynamics. When the interaction of controller and system poles with the filter dynamics on the closed-loop root locus is small (not affecting its qualitative characteristics), filter poles and zeros are omitted to avoid unnecessary clutter.

Due to the difficult and time-consuming nature of performing closed-loop forced response testing, control scheme effectiveness was assessed by comparing the PSD's of average inlet pressure, both with and without control, at the same operating point. Attenuation and/or stabilizing modifications of the 27 and 68 Hz system modes is the figure of merit by which the control laws are evaluated, in addition to any measured flow range extension. Actuation frequency and amplitude are also examined with the premise that low energy actuation is preferential with regard to actuator life.

The first control algorithm tested was simple proportional control. The output of the high-pass filter was multiplied by a constant gain to generate the valve command signal. The open-loop transfer function bode plot is shown in Figure 4.12, and the root locus is shown in Figure 4.13, on which poles of recognized physical phenomena are labeled. The root locus indicates that although the control should damp the 27 Hz mild surge pole, it excites the 68 Hz injection plenum interaction mode and pressure tap resonance. PSD plots comparing frequency content of the inlet static pressure taps during open and closed-loop operation indicate that the 68 Hz and tap resonance modes were excited. However, the mild surge mode was not noticeably damped nor shifted in frequency (see Figure 4.14). These spectra were generated at identical nozzle position and mean injection air flow, but unfortunately, the operating point conditions are unknown due to a loss of data.

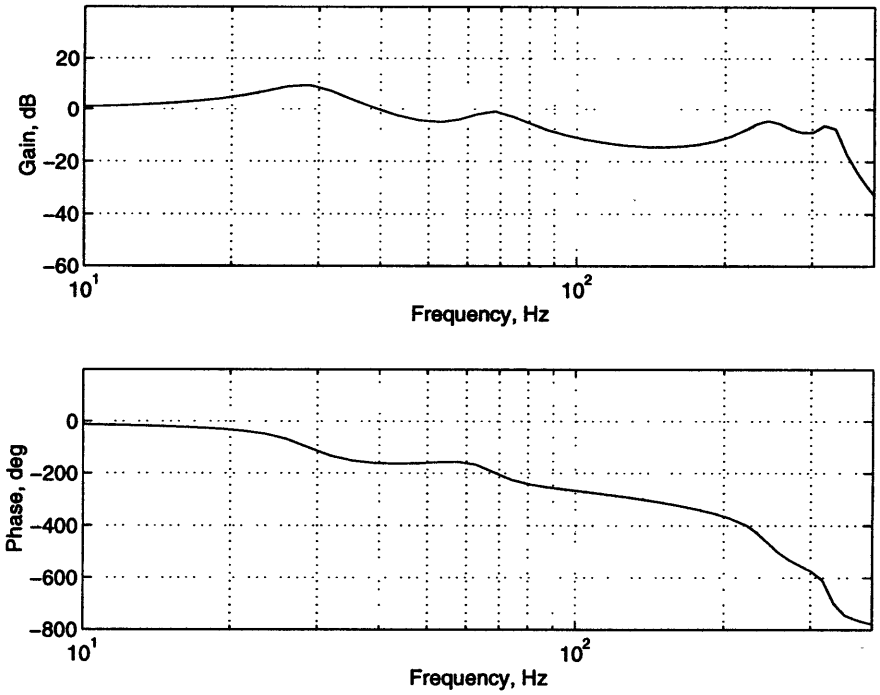

Figure 4.12: Bode plot of open loop transfer function for proportional gain controller (max. f = 400 Hz)

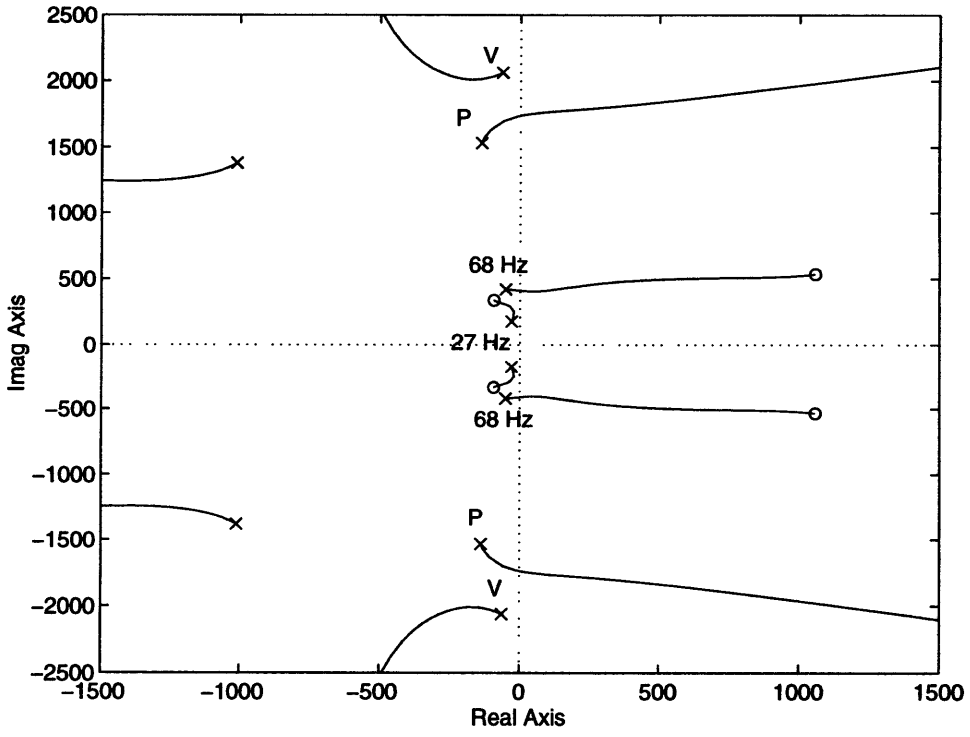

Figure 4.13: Root locus for proportional control law. Poles: 27 Hz - mild surge, 68 Hz - acoustic resonance, P - pressure tap resonance, and V - valve dynamics

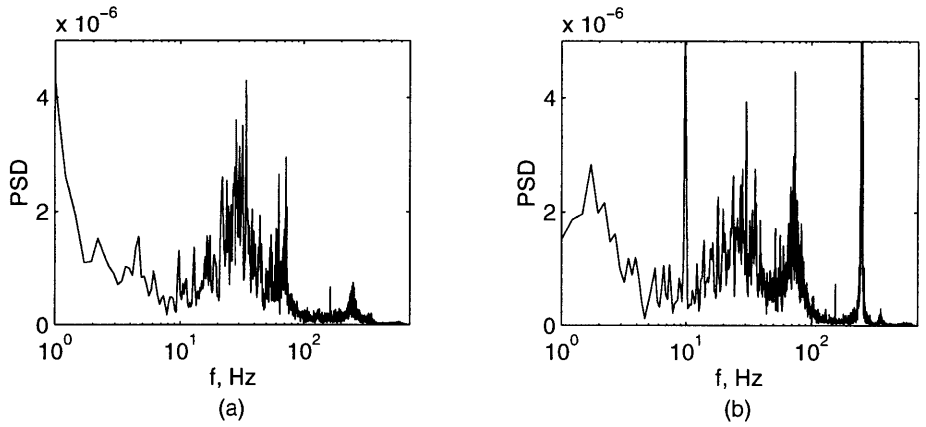

Figure 4.14: Comparison of inlet pressure signal spectrums for (a) no control and (b) proportional control, K = 1.2. $m_{inl,corr}/m_{des}$ is unknown (max. f = 700 Hz)

Figure 4.15 shows the frequency content and a representative time trace of the control valve command. Valve command reflects the inlet pressure spectrum except for low frequency filtered data as expected. However, the valve exhibits high frequency and high amplitude position requests which might limit actuator life.

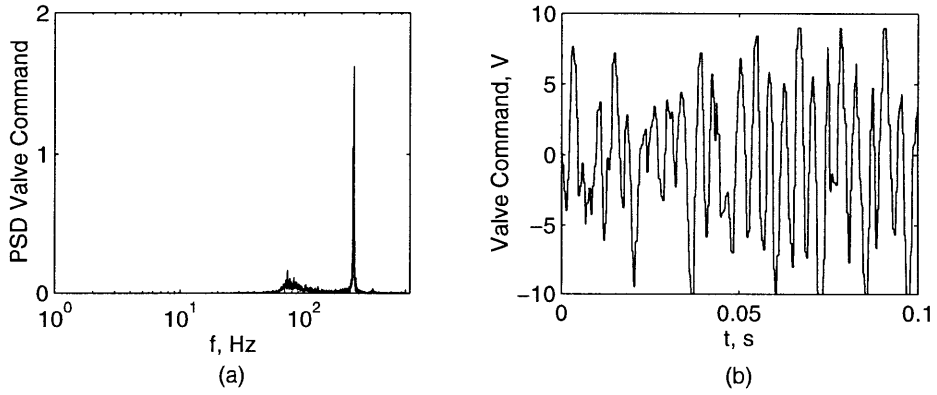

Figure 4.15: (a) Valve command PSD (max. f = 700 Hz) and (b) time trace of typical valve command for proportional control, K = 1.2. $m_{inl,corr}/m_{des}$ is unknown

A lead-lag compensator was used in the feedback loop to improve gain and phase margin characteristics of the system [29]. The bode plot of the open loop transfer function can be seen in Figure 4.16, and the lower frequency portion of the root locus diagram is shown in Figure 4.17 (the higher frequency region is identical to Figure 4.13). Values for the controller poles and zeros are provided in Table 4.2. The goal of this controller was to stabi-

lize mild surge and damp the injection plenum interaction oscillations. Figure 4.18 shows the spectral comparison both with and without control. The controller damps the mild surge peak slightly, but excites the probe resonance and the interaction mode. The large peak near 10 Hz is unexplained, but its sharpness indicates that it might have been an isolated, short-duration event (not modal) during the 15 s data set. When these spectrums are examined with Figure 4.19, the valve command activity, it is apparent that the controller is reacting only to the higher frequency modes. The high frequency, nearly peak to peak chatter of the valve command signal is, again, undesirable for actuator durability. Despite the large excitement of the higher frequency modes, the mild surge mode was still found responsible for the transition into surge (see Figure 19).

With the controller operating at K = 3, surge occurred at $m_{inl,corr}/m_{des} = 0.846$, the lowest surge-free mass flow recorded during experimentation. Recall that the error bounds on this measurement are $m_{inl,corr}/m_{des} = \pm 0.0016$. During periods of control law evaluation, stable, mean-injection operating points (without control) were demonstrated to at least $m_{inl,corr}/m_{des} = 0.861$, a value less than the surge point quoted in Chapter 2. However, since the actual flow range with mean-injection was not determined, it is difficult to claim a significant improvement.

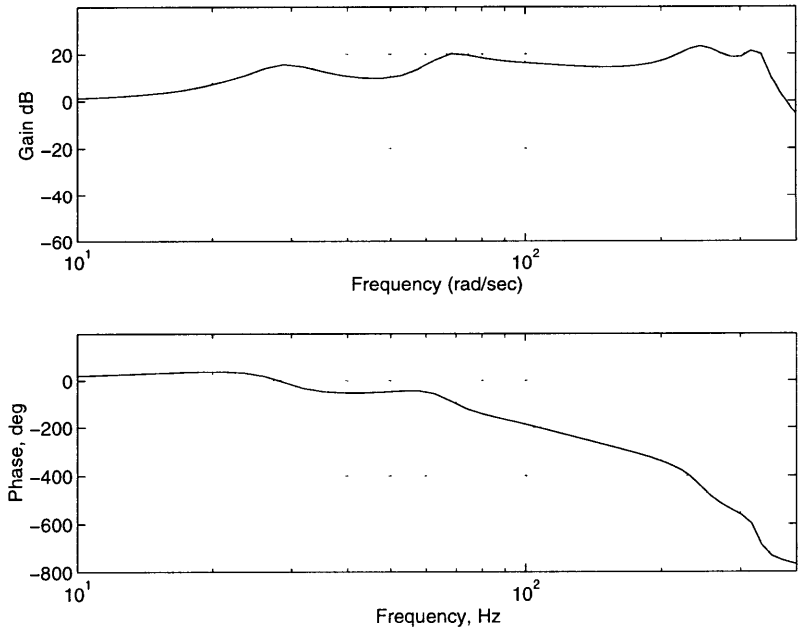

Figure 4.16: Bode plot of open loop transfer function for lead-lag controller

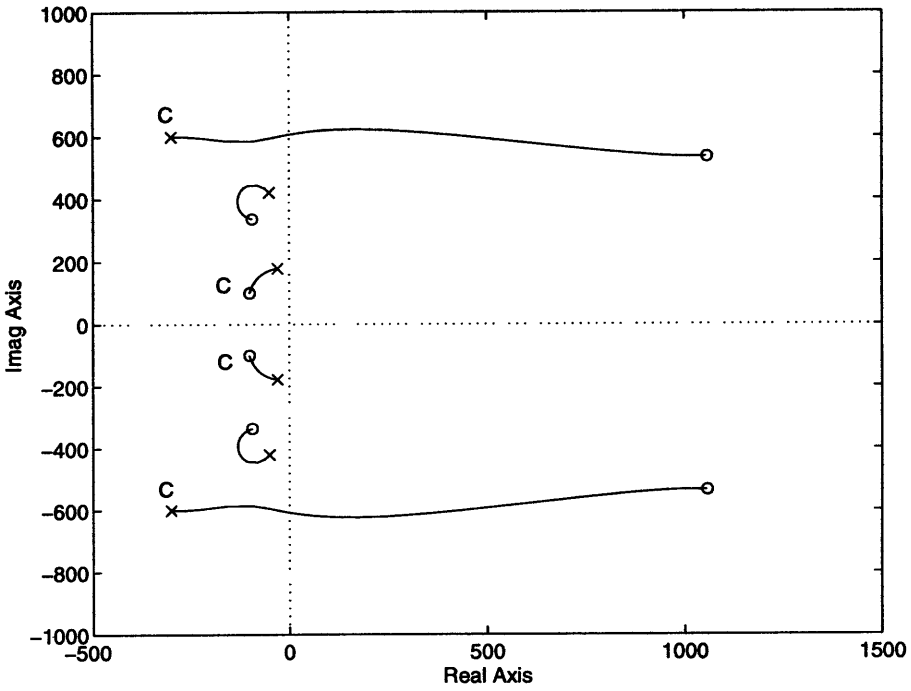

Figure 4.17: Lead-lag controller low frequency root locus. Control poles and zeros noted with a 'C

POLES	Frequency, Hz	Damping Ratio, ς
-299.9887 ± 600.0002i	95.493	0.4472
ZEROS	**Frequency, Hz**	**Damping Ratio, ς**
-100.1397 ± 100.0000i	15.915	0.7076

Table 4.2: Poles and zeros for lead-lag controller

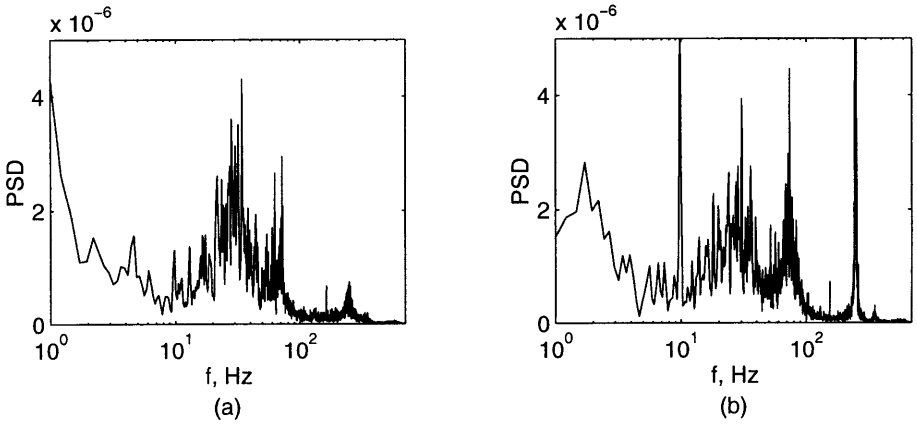

Figure 4.18: Comparison of inlet pressure signal spectrums for (a) no control, $m_{inl,corr}/m_{des}$ = 0.864 and (b) lead/lag compensator control, K = 3, $m_{inl,corr}/m_{des}$ = 0.860 (max f = 700 Hz)

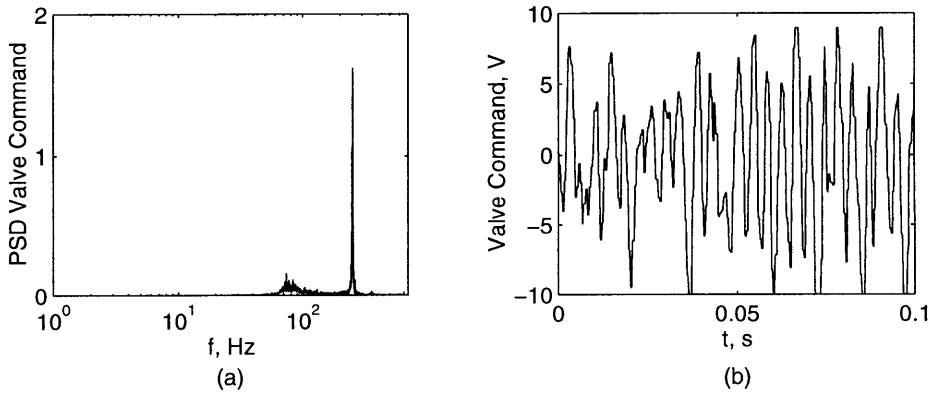

Figure 4.19: (a) Valve command PSD (max. f = 700 Hz) and (b) time trace of typical valve command spectrum for lead/lag compensator control, K = 3 $m_{inl,corr}/m_{des}$ = 0.860

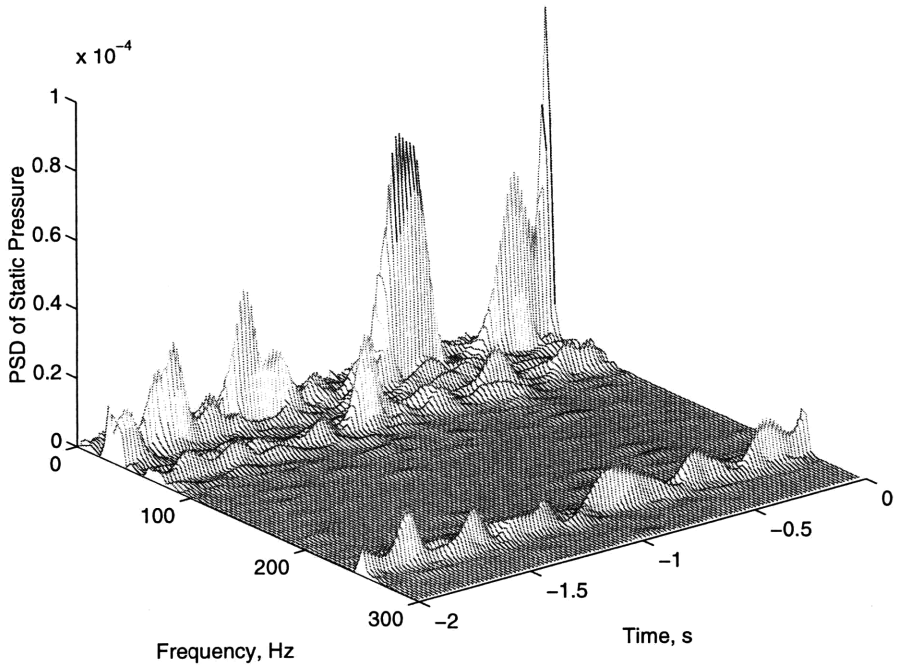

Figure 4.20: Waterfall plot showing transition into surge for engine system under lead-lag control, K = 3, $m_{inl,corr}/m_{des}$ = 0.846

A control law which shows promise in damping mild surge is a classical, bode design compensator. Its open loop transfer function bode plot is shown in Figure 4.21 and its root locus in Figure 4.22. It consisted of three pole and three zero pairs whose locations are shown in Table 4.3. From its root locus the control law attempts to stabilize all of the identified system modes, allowing only valve and compensator dynamics to go unstable. This control law was only briefly evaluated, but its effect on the spectral content was encouraging. At approximately the same $m_{inl,corr}/m_{des}$ as shown in the lead/lag compensator case, the influence of the mild surge peak is virtually eliminated. The injection plenum interaction mode, however, appears at a slightly amplified level, despite the fact that the controller employs a pole-zero cancellation at that location. At higher frequencies, the inlet tap resonance appears in addition to a slightly excited valve resonance. If the mild surge mode is the primary precursor of surge, the damping effect of this control may result in an extension of stable flow range. Unfortunately, experimental difficulties did not allow the testing of this engine to surge.

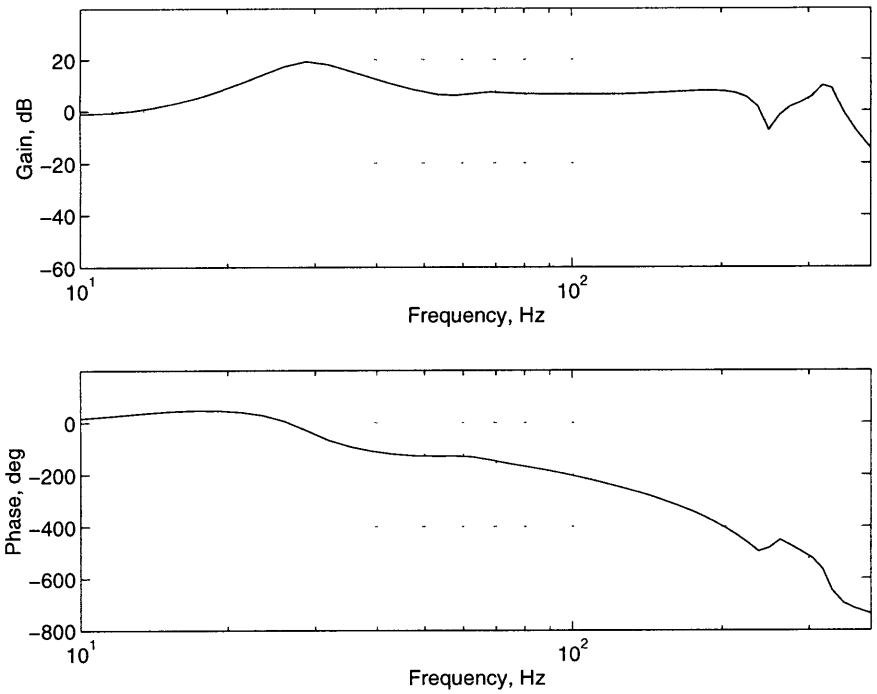

Figure 4.21: Open loop transfer function bode plot for classically designed controller

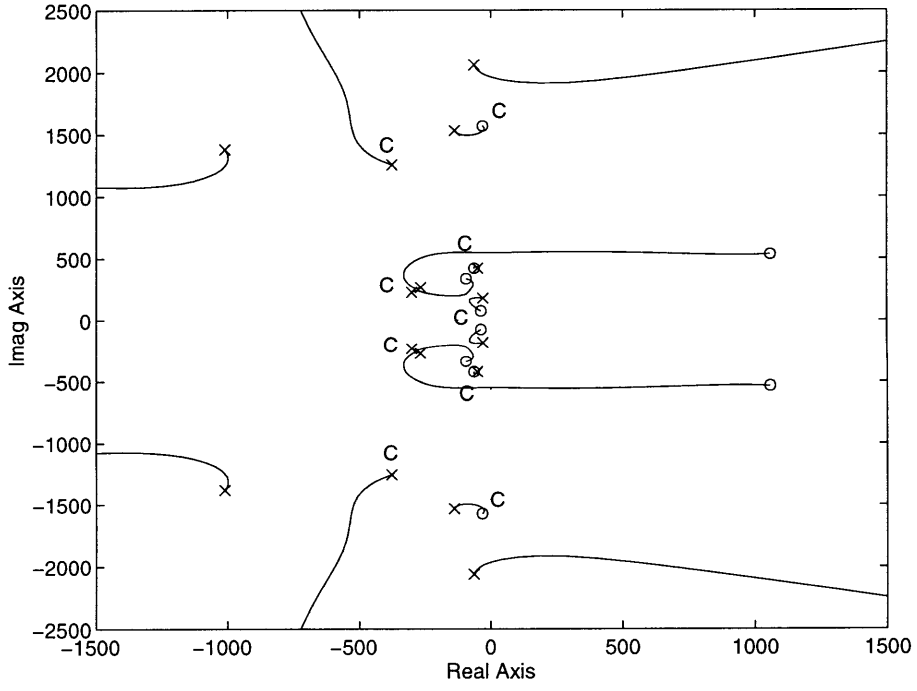

Figure 4.22: Classically-designed controller root locus. Control poles and zeros noted with a 'C'

POLES	Frequency, Hz	Damping Ratio, ς
-376.99 ± 1256.64i	200.00	0.2873
-301.59 ± 226.19i	36.00	0.8000
-267.03 ± 267.03i	42.50	0.7071
ZEROS	**Frequency, Hz**	**Damping Ratio, ς**
-31.41 ± 1570.79i	250.00	0.0200
-37.69 ± 75.39i	12.00	0.4472
-62.83 ± 420.97i	67.00	0.1476

Table 4.3: Poles and zeros for classically designed controller

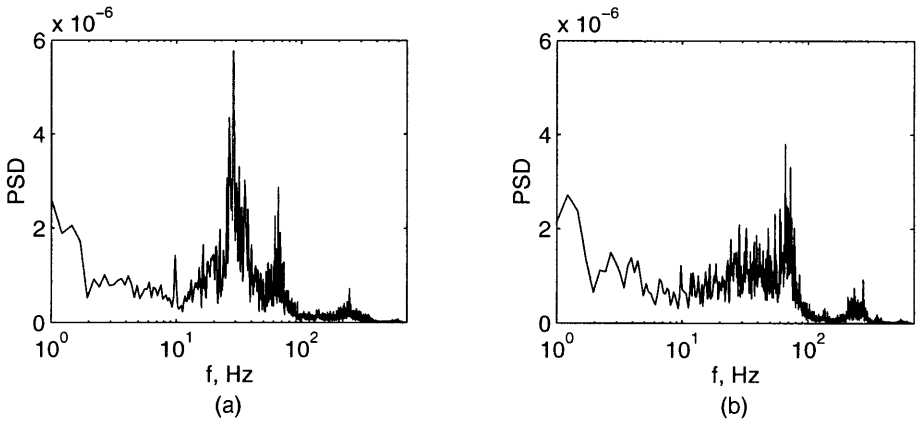

Figure 4.23: Comparison of inlet pressure signal spectrums for (a) no control, $m_{inl,corr}/m_{des}$ = 0.861 and (b) classically designed compensator control, K = 3, $m_{inl,corr}/m_{des}$ = 0.860 (max. f = 700 Hz)

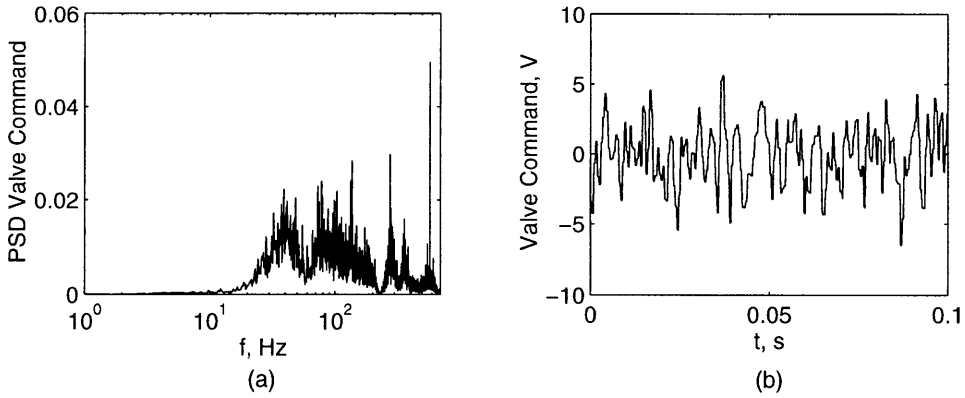

Figure 4.24: (a) Valve command PSD (max. f = 700 Hz) and (b) time trace of typical valve command spectrum for classically designed compensator control, K = 2.5 $m_{inl,corr}/m_{des}$ = 0.860

The final controller tested was an H_∞ design. This controller was designed (and implemented) in state space format, but using Matlab's conversion tools from discrete to continuous time and from state space formulation to a transfer function representation, we can examine the control law in the same fashion as earlier in the chapter. The controller was designed to stabilize the mild surge poles within a region of uncertainty of their location. Figure 4.25 is the bode plot of the H_∞ open-loop transfer function. Figure 4.26 indicates that the mild surge poles would be driven towards lower frequency and higher damping by the presence of nearby controller poles. Figure 4.27 indicates that this frequency shift is occurring, but that there is no associated increase in damping. The mild surge mode is shifted to approximately 18 Hz and an additional mode near 40 Hz appears, possibly associated with controller poles seen in the root locus diagram. Looking ahead to Figure 4.28, it is this reduced frequency mild surge mode which increases in amplitude and precipitates surge.

The lack of damping of this mild surge mode may be explained when the high-pass filter dynamics are included in a root locus plot. As can be seen in Figure 4.29, the filter dynamics interact with the mild surge mode to decrease its damping and drive the pole into the right half plane. Unfortunately, it appears that control law design may have neglected the influence of the filter, and forced the system into instability.

POLES	Frequency, Hz	Damping Ratio, ς
$-90.3636 \pm 197.0664i$	31.364	0.4168
ZEROS	Frequency, Hz	Damping Ratio, ς
1110.477	-	-

Table 4.4: Poles and zeros for H_∞ controller

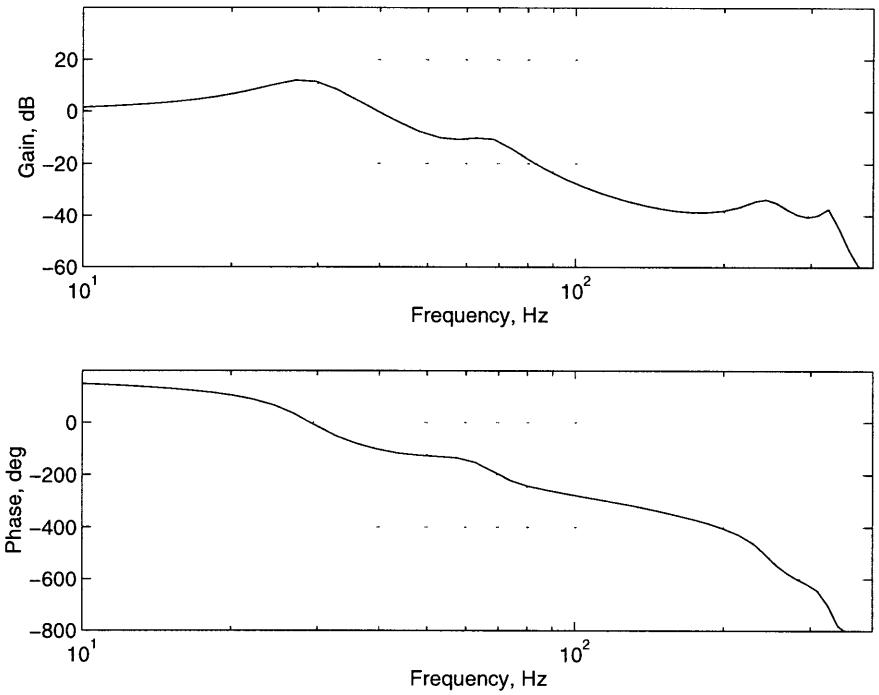

Figure 4.25: Open loop transfer function bode plot for H_∞ controller (max. f = 400 Hz)

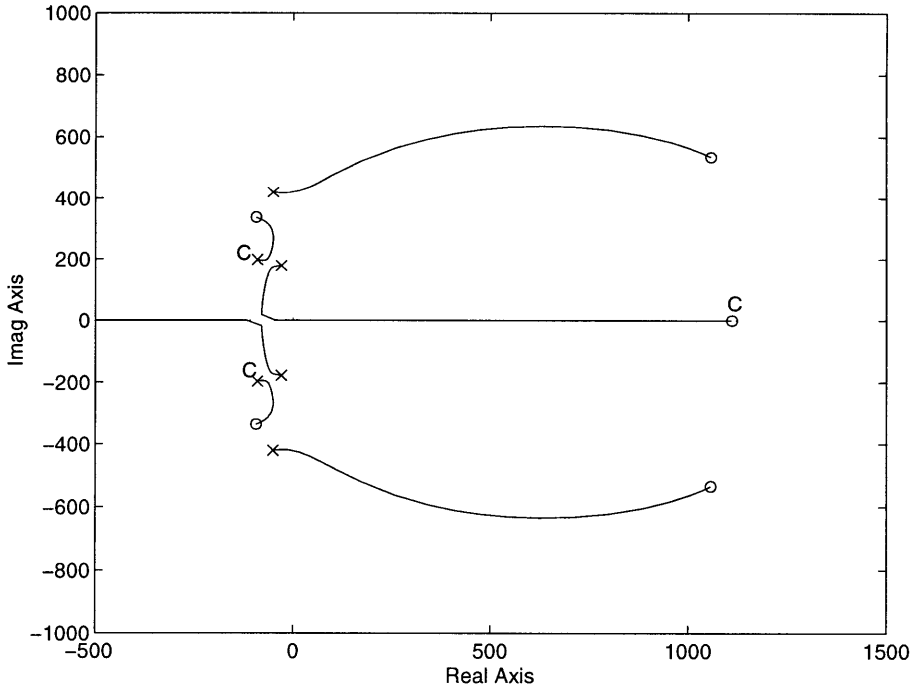

Figure 4.26: H_∞ controller root locus. Control poles and zeros noted with a 'C'

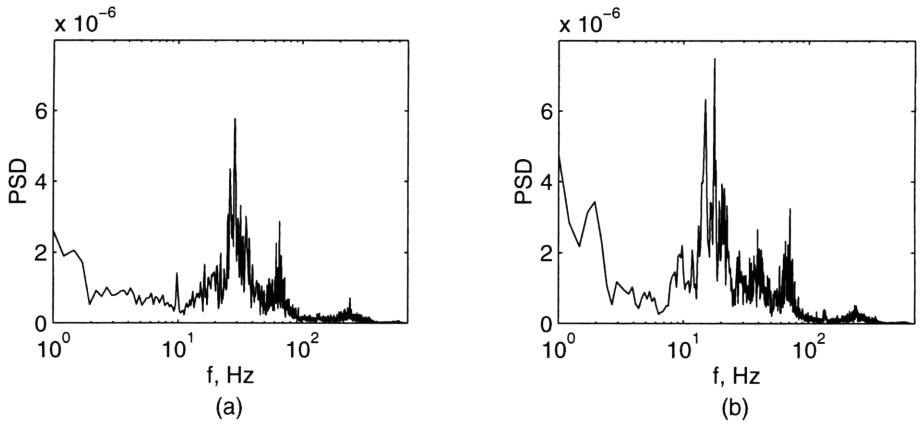

Figure 4.27: Comparison of inlet pressure signal spectrums for (a) no control, $m_{inl,corr}/m_{des}$ = 0.861 and (b) H_∞ compensator control, K = 0.01, $m_{inl,corr}/m_{des}$ = 0.860 (max. f = 700 Hz)

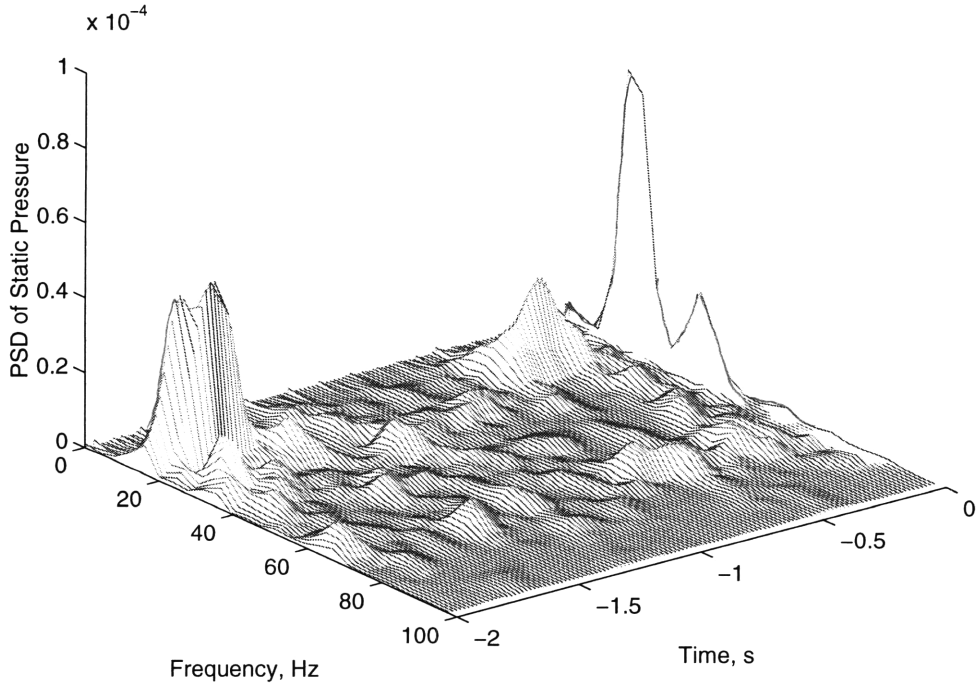

Figure 4.28: Waterfall plot showing transition into surge for engine system under H_∞ control, K = 0.01, $m_{inl,corr}/m_{des}$ = 0.856

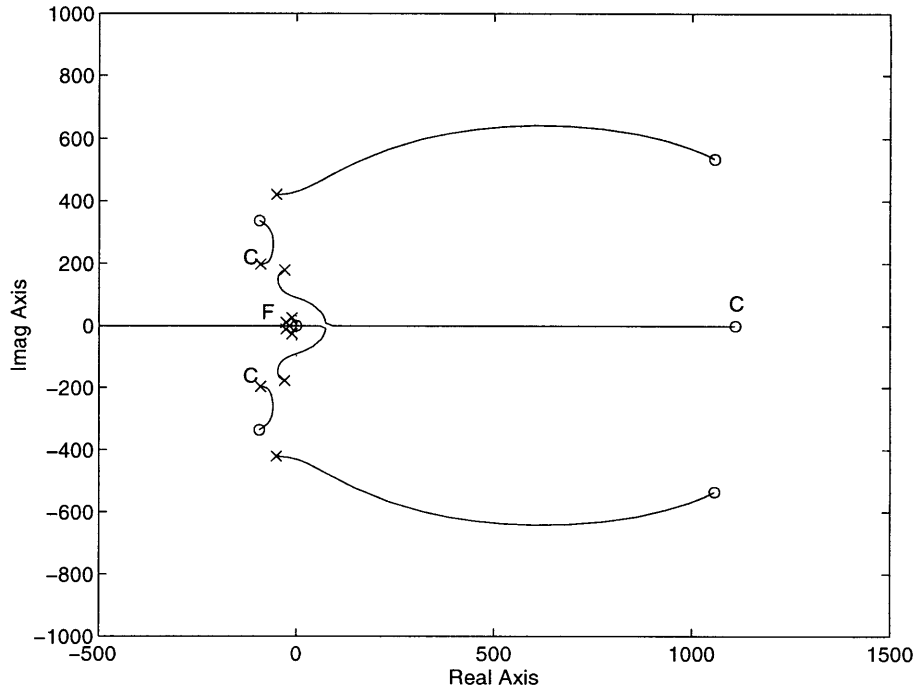

Figure 4.29: H_∞ controller root locus. Control poles and zeros noted with a 'C' and 5-Hz high-pass filter poles and zeros designated by 'F'

Figure 4.30 illustrates that actuation is primarily low frequency and low amplitude at the selected gain. Controller poles roll off the compensator's response to the higher frequency modes. Note that the high frequency modes are not excited by the controller and their natural amplitude remains small. This represents a much more desirable control scheme from the point of view of actuator activity. Therefore, a similar design which takes the high-pass filter dynamics into consideration should be considered for future efforts.

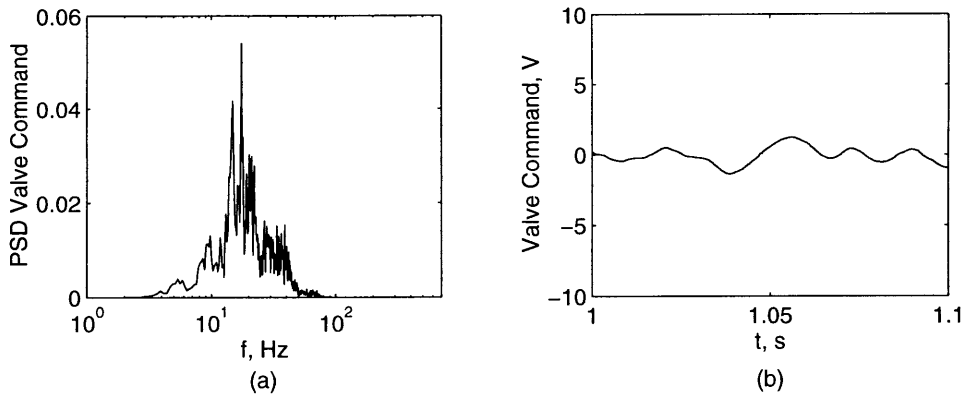

Figure 4.30: (a) Valve command PSD (max. f = 700 Hz) and (b) time trace of typical valve command spectrum for H_∞ compensator control, K = 0.01 $m_{inl,corr}/m_{des} = 0.860$

Several points should be made concerning the control law experimentation. At the time of testing, several of the poles in the system identification were not linked with physical phenomena, in particular the injection plenum interaction mode and inlet tap resonance. Therefore, control law design had to take into consideration higher frequency modes which had uncertain influence on the surge dynamics. Since the origin of these modes is now understood, the obvious conclusion is that a control law design should roll-off the influence of (at least) the tap and valve resonant modes. Unless excited by injection, these modes do not play a roll in the engine system dynamics. Inherent in the design of the H_∞ controller was a attenuation of the higher frequency signals. Note that neither of these modes increased in magnitude as the engine was throttled. Rolling off the influence of the 68 Hz mode might also be a valid approach. Although the model of Appendix B suggests that this mode migrates toward instability, none of the control laws demonstrated were successful in damping it. It also does not exhibit high magnitude behavior at operating points near the onset of deep surge. Therefore, some degree of flow range extension may be achieved by only controlling the mild surge mode. Such an approach has the added benefit of low frequency actuation requirements.

4.3 Summary and Conclusions

Forced response estimates between averaged axial station pressures and the valve command signal were generated for the helicopter gas producer. Discrete frequency sine waves were employed to generate an estimate with reasonable coherence. The frequency associated with the mild surge oscillations of the natural engine dynamics appeared as a complex pole pair in the results for each sensor. Evidence of the injection plenum interaction mode appeared at the inlet, diffuser throat, and vane plenum taps. This frequency did not appear in the diffuser exit or combustor taps. Since it had previously been detected at these sensors in the naturally excited dynamics, it was thought the forced response was beneath the noise level of the system, indicating a lack of controllability. Other documented peaks were associated with tap and valve dynamics.

The inlet static pressure taps in conjunction with the diffuser throat air injection were chosen for use in control because of this scheme's observability of and apparent control authority over the naturally excited resonant modes. A transfer function representation consisting of 5 complex pole pairs and 2 zero pairs was fit to the frequency response estimation, and the estimate was utilized for control design.

Four control laws were examined: proportional gain, lead-lag compensator, a classical bode design, and an H_∞ control law. These control laws were tuned experimentally by observing inlet pressure modal activity on a spectrum analyzer as an indicator of decreased damping and likelihood of surge. Their effectiveness was evaluated in much the same manner. A common characteristic of the first three control laws was high amplitude, high frequency valve activity. Although none yielded a significant extension in stable operating flow range, the actuator and sensor combination successfully demonstrated the capability of modifying system dynamics. Only the classical bode design increased the damping of the mild surge mode, which is thought to be responsible for inducing surge through large excursions in mass flow and pressure. The H_∞ control shifted this large amplitude to a lower frequency, which appeared to precede surge in this case. However, it appears that the system dynamics were entangled with those of the high-pass filter.

Since the physical mechanisms of the prominent modes appearing in the forced response experiments are now known, it is apparent that future control designs can roll off the influence of (at least) the tap acoustic resonance and valve dynamics. In addition to simplifying the control problem, this action would reduce the high frequency oscillation, and thus wear, on the valve actuation system.

Chapter 5: Contributions and Future Work

5.1 Contributions

This thesis describes the near surge behavior of the AlliedSignal LTS-101 gas producer and presents the results from several attempts at active surge control using diffuser throat air injection. It is hoped that the results summarized in this section will be useful in future active control efforts on this engine. The contributions of the research may be summarized as follows:

- Diffuser throat air injection generates two effects: a displacement of inlet mass flow and a slight loss in achievable pressure ratio. The total of injected and inlet flow, when corrected to turbine inlet conditions, remains constant for a given downstream nozzle position. Therefore, inlet mass flow is displaced to satisfy the downstream choking relation. The pressure ratio loss due to injection is lower than predicted by estimates of McNulty [22]. Mixing losses within the diffuser are offset by a slightly elevated pressure ratio exiting the impeller because of reduced flow through this component.

- Injection modifies the peak of the 95% $N_{1,corr}$ speedline characteristic. The speedline with injection exhibits a large region of near zero slope at the peak and also includes a small region of surge-free operation with positive slope. Experimental fits of the characteristic peaks, both with and without injection, are presented.

- Air injection extends surge-free operation to lower corrected turbine inlet flow. The axial stage and centrifugal rotor remain stable at compressor inlet flows where surge normally occurs in the engine without injection. The stable operation of the rotating components indicates the diffuser limits the stability of the system. The fluid dynamic effect of injection stabilizes this component in some manner, possible delaying flow breakdown within individual vane passages.

- Mean injection modifies the pre-surge behavior of the gas producer. Zero-injection cases exhibit virtually no coherent frequency growth prior to surge. With mean injection, fre-

quency growth is noted near 27 Hz and 68 Hz, and the average amplitude of these modes increases as mass flow is throttled. Additional observed frequencies are acoustic resonances associated with instrumentation taps.

- The 27 Hz mode of pressure oscillation is evident at all unsteady pressure taps. An unsteady mass flow estimation technique enables the operating point oscillation cycles to be plotted on a compressor map. The resulting counter-clockwise motion indicates mild surge, a dynamic instability of fluctuating mass flow and pressure ratio. Large amplitude mild surge was found to precede deep surge, but the oscillations do not grow steadily from small displacement disturbances. The mode grows and decays in a random fashion as compressor mass flow is throttled, exhibiting typical behavior of a lightly-damped mode.

- A non-linear simulation of compression system dynamics attributes mild surge to the region of surge-free positive compressor characteristic slope. Simulation cycles grow steadily into surge, however, and do not exhibit the random growth and decay observed in experiment.

- A linear, lumped parameter model attributes the 68 Hz mode to the interaction of the injection plenum upon the compression system dynamics. Although the model is incapable of matching either the mild surge or injection plenum interaction frequencies, it closely matches the phase relationship between compressor inlet static and combustor pressure fluctuations at each mode.

- Open-loop forced response testing was performed at near surge mass flows on the engine, and sensors at all axial locations were examined for coherent responses to forcing. Not surprisingly, since inlet flow displacement is the primary effect of injection, the inlet static pressure taps exhibit the greatest response to actuation and excellent visibility of excited system modes. Therefore, inlet static pressure was chosen to be the regulated variable in linear surge control law design.

- A 10-pole and 4-zero transfer function was fit to the frequency response results of valve command forcing to average inlet static pressure. This identification was utilized by team members for linear control law development.

- Proportional, lead-lag, H_∞, and classical bode controller designs were tested on the engine plus mean-injection system. The lead-lag controller resulted in the lowest $m_{inl,corr}$ recorded during testing. However, it is questionable if the result was a significant flow extension because the engine was not throttled to surge at similar conditions. The H_∞ control law was unsuccessful because of an apparent interaction between controller dynamics and a digital high-pass filter, which processes the pressure feedback variables. The classical bode design exhibited the greatest promise of successful closed-loop operation, for it added substantial damping to the mild surge mode. However, engine damage prevented testing the system to surge.

- The capability of a linear controller to modify the engine's system dynamics was demonstrated. The pressure signal spectrums exhibited damping and shifts in the 27 Hz mild surge mode. However, much control effort was focused at controlling high frequency modes. After testing was completed, it was realized that these modes pertained only to tap acoustics.

5.2 Suggestions for Future Work

The following items are suggestions for future efforts toward understanding the LTS-101's system dynamics and demonstrating active surge control:

- The previous section indicates that sufficient control authority exists to modify the engine system dynamics. The classical bode design should be further investigated, as well as other linear control laws designed to roll-off response to modes above 68 Hz. Since the linear, lumped-parameter model suggests that the 68 Hz mode goes unstable at lower flow than mild surge, a successful closed-loop demonstration may depend only upon damping 27 Hz oscillations.

- One of the shortcomings of control law testing was an inadequate method of comparing operating points between experiments. Injection inlet conditions and mass flow varied only slightly during experiments, but gas path pressure and temperature at the point of injection could vary widely depending upon ambient conditions. The variation in conditions leverages the effect of equivalent amounts of injection. Since the diffuser is the stability limiting device in this gas generator, compressor exit corrected flow is a more appropriate measure of its operating point with respect to the surge line. Time-resolved measurements of injection flow should be made to facilitate this calculation.

- Tuning the unsteady calibration of inlet pressure to mass flow could be accomplished by comparing mass flow fluctuation estimates to hot wire measurements. The results of this correction would provide an experimental estimate of upstream inertia, a side benefit for system modeling.

- Historically, modeling has inadequately predicted the modal frequencies and behavior of this engine. Experiments which might shed light upon modeling issues should be attempted, particularly efforts which might elucidate the behavior and origin of the 68 Hz mode. For example, if the 27 Hz mode could be damped by a control law, it would be useful to see if the 68 Hz migrates toward instability.

References

1 Cumpsty, N. A., *Compressor Aerodynamics*, Longman Scientific and Technical, Essex, U.K., 1989.

2 Emmons, H. W., C. E. Pearson, and H. P. Grant, "Compressor Surge and Stall Propagation," *Trans. of the ASME*, Vol. 79, April 1955, pp. 455-469.

3 Greitzer, E. M., "Surge and Rotating Stall in Axial Flow Compressors, Part I: Theoretical Compression System Model," *ASME J. for Eng. for Power*, Vol. 98, April 1976, pp. 190-198.

4 Greitzer, E. M., "Surge and Rotating Stall in Axial Flow Compressors, Part II: Experimental Results and Comparison with Theory," *ASME J. for Eng. for Power*, Vol. 98, April 1976, pp. 199-217.

5 Moore, F. K. and E. M. Greitzer, "A Theory of Post-Stall Transients in Axial Compression Systems: Part I -- Development of Equations," *ASME J. of Eng. for Gas Tubines and Power*, Vol. 108, January 1986, pp. 68-76.

6 Moore, F. K. and E. M. Greitzer, "A Theory of Post-Stall Transients in Axial Compression Systems: Part I -- Application," *ASME J. of Eng. for Gas Tubines and Power*, Vol. 108, January 1986, pp. 231-239.

7 Toyama, K., P. W. Runstadler, Jr., and R. C. Dean, Jr., "An Experimental Study of Surge in Centrifugal Compressors," *ASME J. of Fluids Eng.,* Vol. 99, March 1977, pp. 115-131.

8 Dean, R. C., Jr., "The Time Domain of Centrifugal Compressor and Pump Stability and Surge," *ASME J. of Fluids Eng.*, Vol. 99, March 1977, pp. 53-63.

9 Ribi, B., and G. Gyarmathy, "Impeller Rotating Stall as a Trigger for the Transition from Mild to Deep Surge in a Subsonic Centrifugal Compressor," ASME Paper 93-GT-234.

10 Oaks, W. C., et al., "High Speed Centrifugal Compressor Surge Initiation Characterization," AIAA Paper 96-2577.

11 Fink, D. A., N. A. Cumpsty, and E. M. Greitzer, "Surge Dynamics in a Free-Spool Centrifugal Compressor System," ASME Paper 91-GT-31.

12 Epstein, A. H., J. E. Ffowcs Williams, and E. M. Greitzer, "Active Suppression of Aerodynamic Instabilities in Turbomachines," *AIAA J. of Propulsion and Power*, Vol. 5, March-April 1989, pp. 204-211.

13 Day, I. J., "Active Suppression of Rotating Stall and Surge in Axial Compressors," *Trans. of the ASME*, Vol. 115, January 1993, pp. 40-47.

14 Paduano, J. D., et al., "Active Control of Rotating Stall in a Low-Speed Axial Compressor," *ASME J. of Turbomachinery*, Vol. 115, January 1993, pp. 48-56.

15 Haynes, J. M., G. J. Hendricks, and A. H. Epstein, "Active Stabilization of Rotating Stall in a Three-Stage Axial Compressor," *ASME J. of Turbomachinery*, Vol. 116, April 1994, pp. 226-239.

16 Gysling, D. L., et al., "Dynamic Control of Centrifugal Compressor Surge Using Tailored Structures," *ASME J. of Turbomachinery*, Vol. 113, October 1991, pp. 710-722.

17 Pinsley, J. E., "Active Stabilization of Centrifugal Compressor Surge," *ASME J. of Turbomachinery*, Vol. 113, October 1991, pp. 723-732.

18 Gysling, D. L., "Dynamic Control of Centrifugal Compressor Surge Using Tailored Structures," *ASME J. of Turbomachinery*, Vol 113, October 1991, pp. 710-722.

19 Ffowcs Williams, J. E., and W. R. Graham, "An Engine Demonstration of Active Surge Control," ASME Paper 90-GT-224.

20 Ffowcs Williams, J. E., M. F. L. Harper, and D. J. Allwright, "Active Stabilization of Compressor Instability and Surge in a Working Engine," *Trans. of the ASME*, Vol. 115, January 1993, pp. 68-75.

21 Bell, J. T., "Measurements of Forced and Unforced Aerodynamic Disturbances in a Turbojet Engine," M.S. Thesis, Department of Aeronautics and Astronautics, Massachusetts Institute of Technology, May 1993.

22 McNulty, G. S., "A Study of Dynamic Compressor Surge Control Strategies for a Gas Turbine Engine," M.S. Thesis, Department of Aeronautics and Astronautics, Massachusetts Institute of Technology, September 1993.

23 Simon, J. S., et al., "Feedback Stabilization of Compression Systems," MIT Gas Turbine Laboratory Report No. 216, March 1993.

24 Borror, S L., "Natural and Forced Response Measurements of Hydrodynamic Stability in an Aircraft Gas Turbine Engine," M.S. Thesis, Department of Aeronautics and Astronautics, Massachusetts Institute of Technology, May 1994.

25 Berndt, R. G., "Actuation for Rotating Stall Control of High Speed Axial Compressors," M.S. Thesis, Department of Aeronautics and Astronautics, Massachusetts Institute of Technology, February 1995.

26 Runstadler, P.W., Jr., F.X. Dolan, and R.C. Dean, Jr., "Diffuser Data Book," Creare Technical Note TN-186, May 1975.

27 Tryfonidis, M., et al., "Prestall Behavior of Several High-Speed Compressors," *Trans. of the ASME*, Vol. 117, January 1995, pp. 62-80.

28 Bendat, J. S. and A.G. Piersol, *Random Data Analysis and Measurement Procedures*, John Wiley and Sons, New York, 1986.

Appendix A: Estimate of Unsteady Compressor Mass Flow

A method for estimating unsteady compressor mass flow on the LTS-101 gas generator was devised for examining 1-D flow oscillations and use in future non-linear control laws. High-frequency pressure signals are filtered to attenuate response to fluid inertial effects, accelerations and decelerations of the flow. The filtered output then serves as input into a steady-state mass flow calibration.

Four high-frequency response pressure taps, located upstream of the axial rotor (refer to Chapter 2 for further details), were calibrated to referred mass flow. Referred mass flow was determined by an inlet bellmouth calibrated to steady, inlet static pressure depression. 10 15-second mass flow averages were fit with 6th-order polynomials of static pressure depression at the high-frequency taps. Differences in tap geometry and suspected flow asymmetry near these locations mandated that a separate curve, such as shown in Figure A-1, be generated for each tap. Differences between the 5 psig Kulite transducers attached to the taps was eliminated as a source of variation by examining several transducer/tap combinations.

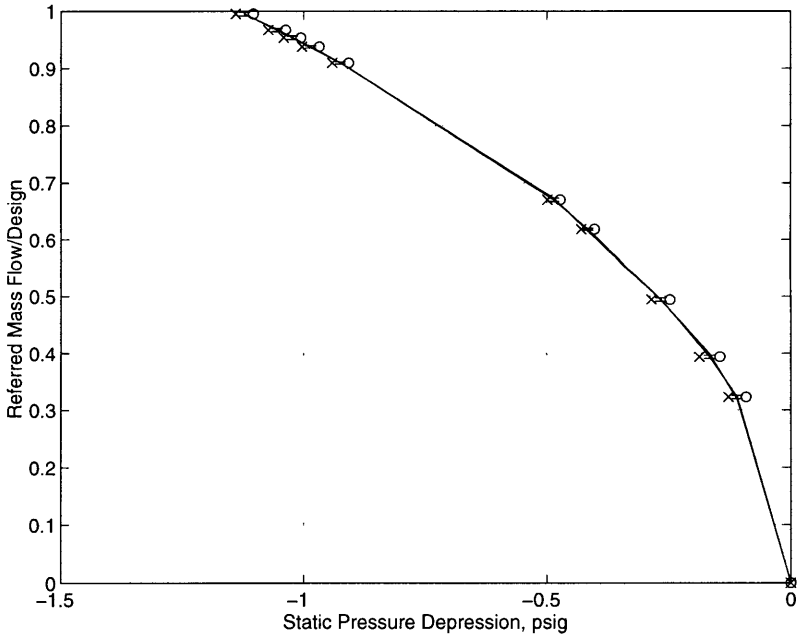

Figure A-1: Example inlet pressure tap calibration to referred compressor mass flow. "x" and "o" bound ± 1σ pressure scatter at calibration points.

The basis of the steady-state calibration is the steady, incompressible Bernoulli relationship. However, its validity in capturing unsteady mass flow fluctuations had to be examined. In other words, in the frequency range of interest (generally < 100 Hz), does the steady-state tap calibration accurately predict the magnitude of unsteady fluctuations, and is the phase difference between pressure signals and actual mass flow negligible? Figure A-2 is a schematic of the geometry analyzed.

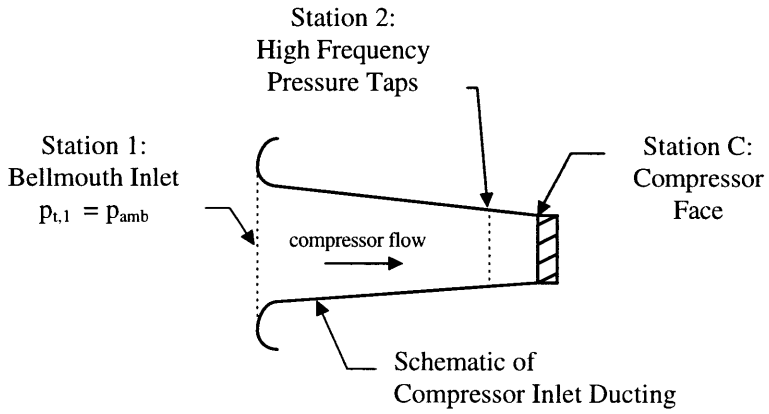

Figure A-2: Schematic of compressor inlet and flow stations

Equation A.1 is the unsteady, incompressible Bernoulli equation for flow with constant p_t at the bellmouth inlet. This formulation assumes negligible unsteady effects between the large diameter inlet ducting and bellmouth entrance. The variable of integration, x is measured along a streamline.

$$p_{t,1} = p_{amb} = \int_1^2 \frac{dv(x)}{dt} \cdot dx + \frac{\rho v_2^{\,2}}{2} + p_2 \qquad (A.1)$$

Expressing velocities in terms of compressor face conditions (subscript c), assuming incompressible continuity, and rearranging, A.1 becomes:

$$p_{amb} - p_2 = -p_{dep} = \rho A_c \frac{dv_c}{dt} \int_1^2 \frac{dx}{A(x)} + \frac{\rho v_c^{\,2}}{2} \left(\frac{A_c}{A_2} \right)^2 \qquad (A.2)$$

Linearizing this equation and expressing it in the Laplace domain yields:

$$-\tilde{p}_{dep} = \rho A_c \tilde{v}_c s \int_1^2 \frac{dx}{A(x)} + \rho \bar{v}_c \tilde{v}_c \left(\frac{A_c}{A_2} \right)^2 \tag{A.3}$$

The definition of referred mass flow yields:

$$v_c = \frac{\dot{m}_{ref} \delta}{\rho A_c \sqrt{\theta}} \tag{A.4}$$

Substituting A.4 into A.3 and solving for the resulting transfer function yields:

$$\frac{\tilde{\dot{m}}_{ref}(s)}{\tilde{p}_{dep}(s)} = -\frac{1}{\int_1^2 \frac{dx}{A(x)}} \left[\frac{1}{s + \left(\frac{\frac{\bar{\dot{m}}_{ref}}{\rho} \frac{\delta}{\sqrt{\theta}} \frac{1}{A_2^2}}{\int_1^2 \frac{dx}{A(x)}} \right)} \right] \tag{A.5}$$

A.5 describes the magnitude and phase relationship between m_{ref} and p_{dep} in terms of the unsteady Bernoulli relation. However, for zero frequency (steady-state, s = 0), the magnitude of the relationship is defined at each tap by its calibration curve, which does not necessarily agree with the magnitude predicted by A.5. A solution to this problem is to process p_{dep} values through a filter with identical frequency response characteristics as A.5 but unit magnitude when s = 0. The output of this filter would then be multiplied by $\frac{d\dot{m}_{ref}}{dp_{filt}}$ at the given operating point, the derivative of the calibration curve for the appropriate high-frequency tap. This approach is justified by the small amplitude (< 5% m_{des}) of mass flow oscillations, so $\frac{d\dot{m}_{ref}}{dp_{filt}}$ is nearly constant at a given mean operating point.

$$\frac{\tilde{\dot{m}}_{ref}(s)}{\tilde{p}_{dep}(s)} = \frac{\tilde{p}_{filt}(s)}{\tilde{p}_{dep}(s)} \cdot \frac{\tilde{\dot{m}}_{ref}(s)}{\tilde{p}_{filt}(s)} \approx \frac{\tilde{p}_{filt}(s)}{\tilde{p}_{dep}(s)} \cdot \left. \frac{d\dot{m}_{ref}}{dp_{filt}} \right|_{\substack{\text{operating} \\ \text{point}}} \tag{A.6}$$

Where:

$$\frac{\tilde{p}_{filt}(s)}{\tilde{p}_{dep}(s)} = \frac{\tilde{\dot{m}}_{ref}(s)}{\tilde{p}_{dep}(s)} \cdot -\left[\frac{\overline{\dot{m}}_{ref}}{\rho}\frac{\delta}{\sqrt{\theta}}\frac{1}{A_2^{\,2}}\right] \tag{A.7}$$

The geometric inputs into the filter relation are shown below. Validation of these parameters should be performed by correlating mass flow estimates from hot-wire anemometry and the algorithm discussed above. However, it is believed that the unsteady correction is qualitatively accurate. $\dot{m}_{ref}$, ρ, δ, and θ are determined by operating point and atmospheric conditions.

$$\int_1^2 \frac{dx}{A(x)} = 8.8643 \ \frac{1}{ft} \tag{A.8}$$

$$A_2 = 0.1444 \ ft^2 \tag{A.9}$$

Figure A-3 shows the frequency response characteristics of the pressure/mass flow filter. With a corner frequency of approximately 45 Hz, within the range of interest, it is apparent that the influence of inertial effects corrupts an estimate of unsteady mass flow based solely on a steady-state calibration. Therefore, the filter shown in Figure A-3 must be included in the estimation algorithm.

For implementation, the filter relationship was converted to its discrete time equivalent using Matlab utilities. Discrete, filtered pressures were input into the appropriate steady-state mass flow calibration, and the output mass flows were averaged. This method avoids the computation of derivatives at each operating point for each tap, and can be justified, again, by the small magnitude of the mass flow fluctuations present. Unsteady mass flow estimates in this thesis were averages of 3 individual tap calculated values.

Figures A-4 and A-5 compare unfiltered and filtered mass flow estimates in plots of mild surge oscillations. For the filtered case, mass flow fluctuations are reduced slightly and lag pressure ratio oscillations, creating a slight tilt in the phase trajectory. The filtered traces also appear smoother because of high frequency signal attenuation.

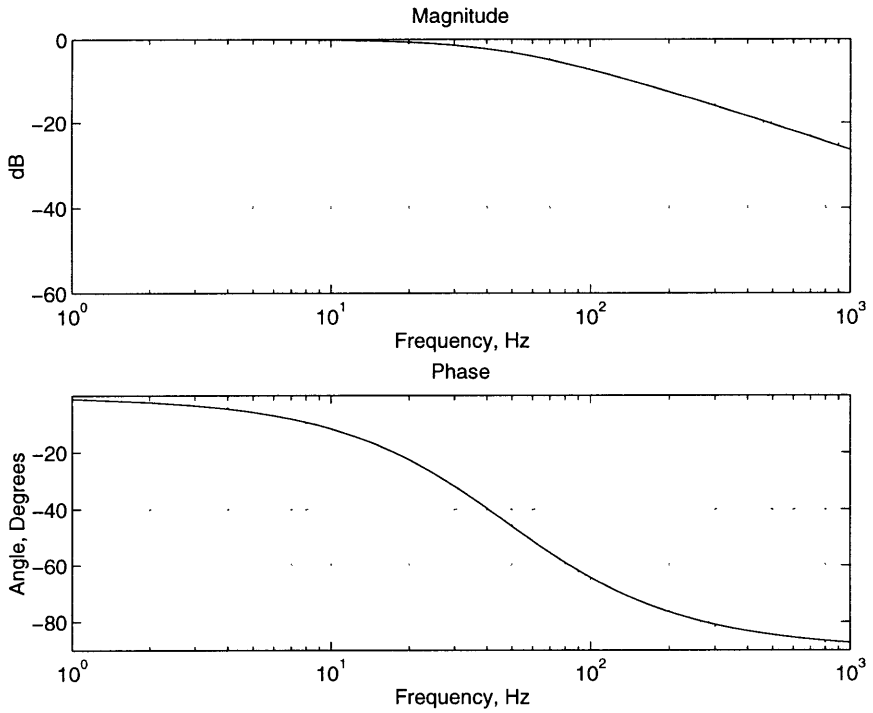

Figure A-3: Bode plot of filter for pressure signals used in unsteady mass flow calculations

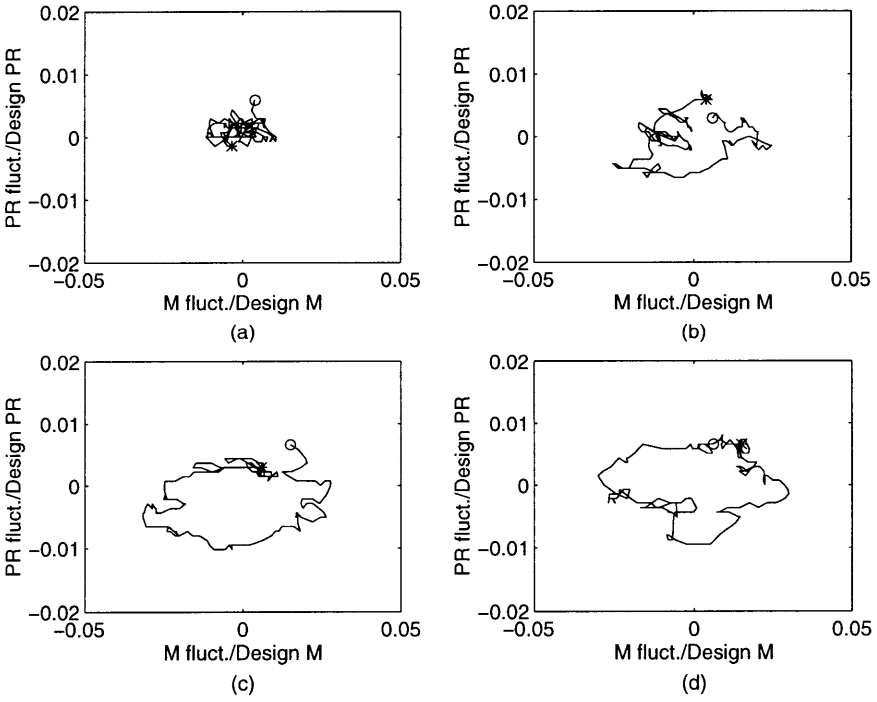

Figure A-4: Progression of mild surge cycle in 0.04 s increments with mass flow estimate not corrected for unsteadiness. "*" represents beginning of segments and "o" represents end.

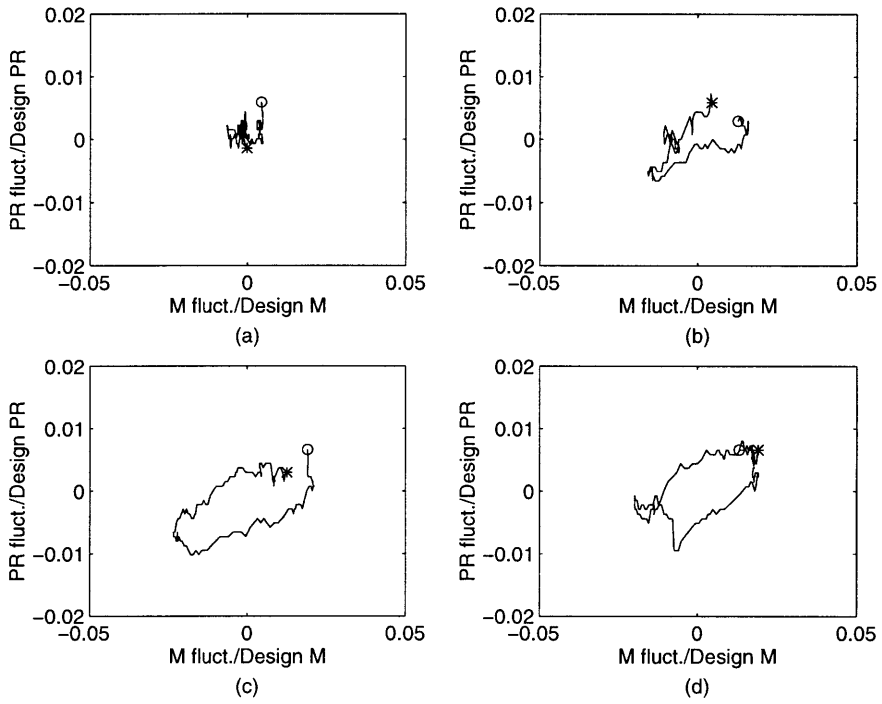

Figure A-5: Progression of mild surge cycle in 0.04 s increments with mass flow estimate corrected for unsteadiness. "*" represents beginning of segments and "o" represents end.

Appendix B: Gas Turbine System Model With Injection Plenum

A challenge in analyzing the LTS-101 stability experiments was determining the origin of 68 Hz oscillations which appeared near surge with mean injection. Initially thought to be acoustic, attempts to estimate frequencies of equivalent duct geometry and resonator volumes were not conclusive. Correcting engine-off forced response results to "hot" engine conditions was also attempted. It was noted in Chapter 3 that the 68 Hz signal was amplified when a certain phase relationship was established between the inlet, diffuser throat, vane plenum, diffuser exit, and combustor taps. When this phase relationship deteriorated, the amplitude decreased. A discontinuity between oscillations at the compressor inlet and diffuser exit appeared at the throat of the diffuser, the location of air injection. Therefore, the 68 Hz oscillations were hypothesized to be interaction of the injection feed plenum with the engine's dynamics. This appendix develops a linearized, lumped-parameter surge model based upon McNulty's work [22] but modified to include an injection plenum. Several relationships in the model are simplified during the mathematical development to make the level of effort consistent with the objective of explaining the 68 Hz mode's origin. The goal is not to produce a high-fidelity tool for engine simulation.

Figure 5-1 shows a schematic of the model, identical to McNulty's except for the injection plenum and throttle. Mass flow from the high-frequency valve, m_{valve}, enters the injection plenum where it feeds into the downstream compressor ducting. The downstream ducting and injection throttle represent the vaned diffuser and the slots in the vane walls, respectively. The throttle is modeled as an orifice with an equivalent C_dA. The two methods of "forcing" the model for frequency response computations, m_{valve} and $p_{b,noise}$, are shown in the location of their influence. The mathematical development of the model follows.

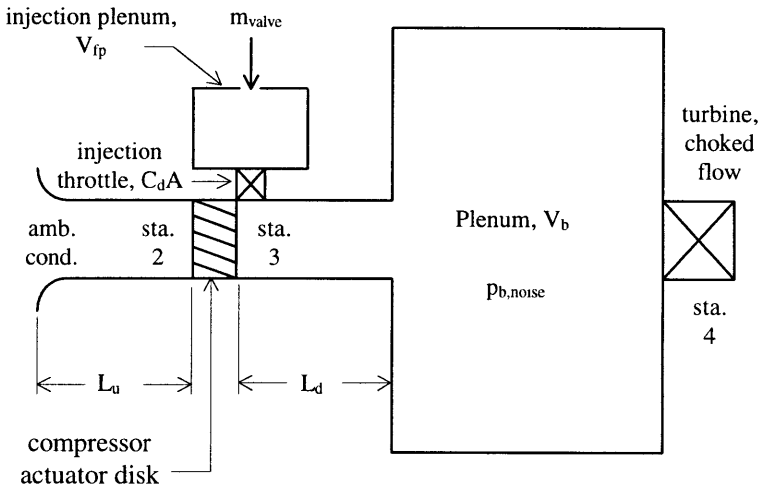

Figure B-1: Schematic of compression system with injection plenum

Upstream compressor duct momentum equation (in total pressure form, McNulty [22]):

$$\frac{d\dot{m}_u}{dt} = \frac{A_c}{L_u}\left(p_{amb} - p_{t,2}\right); \qquad p_{amb} = \text{constant} \tag{B.1}$$

Compressor actuator disk (note all computations assume constant $N_{1,corr}$):

$$p_{t,3} = \pi_c\left(\dot{m}_{u,corr}, N_{1,corr}\right)\cdot p_{t,2}; \qquad N_{1,corr} = \text{constant} \quad \text{and} \quad \dot{m}_{u,corr} = \dot{m}_u \cdot \frac{\sqrt{T_{amb}}\cdot p_{std}}{\sqrt{T_{std}}\cdot p_{amb}} \tag{B.2}$$

Downstream compressor duct momentum equation including combustor pressure noise:

$$\frac{d\dot{m}_d}{dt} = \frac{A_c}{L_d}\left(p_{t,3} - \left(p_b + p_{b,noise}\right)\right) \tag{B.3}$$

Combustor plenum continuity equation, isentropic plenum assumption:

$$\frac{dp_b}{dt} = \frac{a_b^2}{V_b}\left(\dot{m}_d - \dot{m}_4\right) \tag{B.4}$$

Turbine constant corrected flow condition (choked NGVs):

$$\dot{m}_4 = \dot{m}_{4,corr} \cdot \frac{\sqrt{T_{std}} \cdot \left(p_b + p_{b,noise}\right)}{\sqrt{T_b} \cdot p_{std}}; \qquad \dot{m}_{4,corr} \cdot \frac{\sqrt{T_{std}}}{p_{std}} = \text{constant} \tag{B.5}$$

Injection feed plenum continuity equation, isentropic plenum assumption:

$$\frac{dp_{fp}}{dt} = \frac{a_{fp}^2}{V_{fp}}\left(\dot{m}_{valve} - \dot{m}_{inj}\right) \tag{B.6}$$

Injection throttle orifice relation:

$$\dot{m}_{inj} = C_d A \cdot \sqrt{2\rho_{fp}\left(p_{fp} - p_{s,3}\right)}; \qquad \rho_{fp} = \text{constant} \tag{B.7}$$

In order to simplify the mathematics of the model, this throttle relation is linearized and assumed valid for flow into and out of the feed plenum. It is also assumed to be quasi-steady because of the small inertia in the diffuser vane injection slots it represents. The throttle slope is expressed as follows:

$$\frac{d\dot{m}_{inj}}{d\Delta p_s} = C_d A \cdot \sqrt{\frac{\overline{p}_{fp}}{2 \cdot RT_{fp}\left(\overline{p}_{fp} - \overline{p}_{s,3}\right)}} \tag{B.8}$$

So:

$$\dot{m}_{inj} = \frac{d\dot{m}_{inj}}{d\Delta p_s} \cdot \left(p_{fp} - p_{s,3}\right) \tag{B.9}$$

Note from B.7 and B.9 that the static pressure difference between the feed plenum and station 3 drives the flow across the throttle. Since total pressures are used in the duct momentum equations, pressure at station 3 must be converted to static pressure. Given the flow area, mass flow, total pressure, and total temperature, the throat Mach number is computed. Static pressure is then be computed by compressibility relations. The model assumes that for small perturbations of inlet mass flow, Mach number does not change at the throat. This simplification eliminates the need to compute a new total to static pressure relation for each flow and compressor exit condition.

$$p_{s,3} = p_{t,3} \cdot f\left(M_{th}, \gamma\right) = p_{t,3} \cdot \left(1 + \frac{\gamma - 1}{2} M_{th}^2\right)^{\frac{-\gamma}{\gamma - 1}} \tag{B.10}$$

In order to reduce the system to functions of variables appearing in time derivatives (state variables), an additional algebraic relation is required. This equation represents the continuity of mass flow in the downstream compressor duct. It utilizes the previously developed throttle characteristic slope, and is used to eliminate $p_{t,3}$ and $p_{t,2}$ from the state equations.

$$\dot{m}_d = \dot{m}_u + \dot{m}_{inj} = \dot{m}_u + \frac{d\dot{m}_{inj}}{d\Delta p_s} p_{fp} - f\left(\overline{M}_{th}, \gamma\right) \frac{d\dot{m}_{inj}}{d\Delta p_s} p_{t,3} \tag{B.11}$$

$$p_{t,3} = \frac{\left(\dot{m}_u - \dot{m}_d + \frac{d\dot{m}_{inj}}{d\Delta p_s} p_{fp}\right)}{f\left(\overline{M}_{th}, \gamma\right) \frac{d\dot{m}_{inj}}{d\Delta p_s}} \tag{B.12}$$

$$p_{t,2} = \frac{\left(\dot{m}_u - \dot{m}_d + \frac{d\dot{m}_{inj}}{d\Delta p_s} p_{fp}\right)}{\pi_c \cdot f\left(\overline{M}_{th}, \gamma\right) \frac{d\dot{m}_{inj}}{d\Delta p_s}} \tag{B.13}$$

So, the state equations become:

$$\frac{d\dot{m}_u}{dt} = \frac{A_c}{L_u} \left(p_{amb} - \frac{\left(\dot{m}_u - \dot{m}_d + \frac{d\dot{m}_{inj}}{d\Delta p_s} p_{fp}\right)}{\pi_c \cdot f\left(\overline{M}_{th}, \gamma\right) \frac{d\dot{m}_{inj}}{d\Delta p_s}} \right) \tag{B.14}$$

$$\frac{d\dot{m}_d}{dt} = \frac{A_c}{L_d} \left(\frac{\left(\dot{m}_u - \dot{m}_d + \frac{d\dot{m}_{inj}}{d\Delta p_s} p_{fp}\right)}{f\left(\overline{M}_{th}, \gamma\right) \frac{d\dot{m}_{inj}}{d\Delta p_s}} - \left(p_b + p_{b,noise}\right) \right) \tag{B.15}$$

$$\frac{dp_{fp}}{dt} = \frac{a_{fp}^2}{V_{fp}} \left(\dot{m}_u - \dot{m}_d + \dot{m}_{valve}\right) \tag{B.16}$$

$$\frac{dp_b}{dt} = \frac{a_b^2}{V_b}\left(\dot{m}_d - \left(\dot{m}_{4,corr} \cdot \frac{\sqrt{T_{std}} \cdot \left(p_b + p_{b,noise}\right)}{\sqrt{T_b} \cdot p_{std}}\right)\right) \tag{B.17}$$

Equations B.14-17 were left in dimensional form and linearized to form a state-space system of the following form:

$$\dot{\tilde{\mathbf{x}}} = \mathbf{A}\tilde{\mathbf{x}} + \mathbf{B}\tilde{\mathbf{u}} \tag{B.18}$$

$$\tilde{\mathbf{y}} = \mathbf{C}\tilde{\mathbf{x}} + \mathbf{D}\tilde{\mathbf{u}} \tag{B.19}$$

where:

$$\tilde{\mathbf{x}} = \begin{bmatrix} \tilde{\dot{m}}_u \\ \tilde{\dot{m}}_d \\ \tilde{p}_{fp} \\ \tilde{p}_b \end{bmatrix} \qquad \tilde{\mathbf{u}} = \begin{bmatrix} \tilde{\dot{m}}_{valve} \\ \tilde{p}_{b,noise} \end{bmatrix} \qquad \tilde{\mathbf{y}} = \begin{bmatrix} \tilde{p}_b \\ \tilde{p}_{fp} \\ \tilde{p}_{s,2} \\ \tilde{\dot{m}}_u \end{bmatrix} \tag{B.20}$$

The outputs, **y**, were chosen for comparison to engine data. The elements of the state-space matrices are shown below:

$$\mathbf{A} = \begin{bmatrix} A(1,1) & A(1,2) & A(1,3) & 0 \\ A(2,1) & A(2,2) & A(2,3) & A(2,4) \\ A(3,1) & A(3,2) & 0 & 0 \\ 0 & A(4,2) & 0 & A(4,4) \end{bmatrix} \tag{B.21}$$

$$A(1,1) = \frac{\partial\left(\frac{d\dot{m}_u}{dt}\right)}{\partial \dot{m}_u} = -\frac{A_c}{L_u \cdot \overline{\pi}_c \cdot f\left(\overline{M}_{th}, \gamma\right)\frac{d\dot{m}_{inj}}{d\Delta p_s}} + \frac{A_c}{L_u \cdot \overline{\pi}_c^2 \cdot f\left(\overline{M}_{th}, \gamma\right)} \cdot$$

$$\left[\left(\frac{\overline{\dot{m}}_u}{\frac{d\dot{m}_{inj}}{d\Delta p_s}} - \frac{\overline{\dot{m}}_d}{\frac{d\dot{m}_{inj}}{d\Delta p_s}} + \overline{p}_{fp}\right) \cdot \frac{d\pi_c}{dm_{u,corr}} \cdot \frac{\sqrt{\overline{T}_{amb}}}{\sqrt{T_{std}}} \cdot \frac{P_{std}}{\overline{P}_{amb}}\right] \tag{B.22}$$

$$A(1,2) = \frac{\partial\left(\frac{d\dot{m}_u}{dt}\right)}{\partial\dot{m}_d} = \frac{A_c}{L_u \cdot \overline{\pi}_c \cdot f\left(\overline{M}_{th},\gamma\right)\frac{d\dot{m}_{inj}}{d\Delta p_s}} \tag{B.23}$$

$$A(1,3) = \frac{\partial\left(\frac{d\dot{m}_u}{dt}\right)}{\partial p_{fp}} = \frac{A_c}{L_u \cdot \overline{\pi}_c \cdot f\left(\overline{M}_{th},\gamma\right)} \tag{B.24}$$

$$A(2,1) = \frac{\partial\left(\frac{d\dot{m}_d}{dt}\right)}{\partial\dot{m}_u} = \frac{A_c}{L_d \cdot f\left(\overline{M}_{th},\gamma\right)\frac{d\dot{m}_{inj}}{d\Delta p_s}} \tag{B.25}$$

$$A(2,2) = \frac{\partial\left(\frac{d\dot{m}_d}{dt}\right)}{\partial\dot{m}_d} = -\frac{A_c}{L_d \cdot f\left(\overline{M}_{th},\gamma\right)\frac{d\dot{m}_{inj}}{d\Delta p_s}} \tag{B.26}$$

$$A(2,3) = \frac{\partial\left(\frac{d\dot{m}_d}{dt}\right)}{\partial p_{fp}} = \frac{A_c}{L_d \cdot f\left(\overline{M}_{th},\gamma\right)} \tag{B.27}$$

$$A(2,4) = \frac{\partial\left(\frac{d\dot{m}_d}{dt}\right)}{\partial p_b} = -\frac{A_c}{L_d} \tag{B.28}$$

$$A(3,1) = \frac{\partial\left(\frac{dp_{fp}}{dt}\right)}{\partial\dot{m}_u} = \frac{a_{fp}^2}{V_{fp}} \tag{B.29}$$

$$A(3,2) = \frac{\partial\left(\frac{dp_{fp}}{dt}\right)}{\partial\dot{m}_d} = -\frac{a_{fp}^2}{V_{fp}} \tag{B.30}$$

$$A(4,2) = \frac{\partial\left(\frac{dp_b}{dt}\right)}{\partial \dot{m}_d} = \frac{a_b^2}{V_b} \tag{B.31}$$

$$A(4,4) = \frac{\partial\left(\frac{dp_b}{dt}\right)}{\partial p_b} = -\frac{a_b^2}{V_b} \cdot \dot{m}_{4,corr} \cdot \frac{\sqrt{T_{std}}}{\sqrt{T_b} \cdot p_{std}} \tag{B.32}$$

The **B** matrix can be expressed with coefficients of the **A** matrix.

$$\mathbf{B} = \begin{bmatrix} 0 & A(1,4) \\ 0 & A(2,4) \\ -1 \cdot A(3,2) & 0 \\ 0 & A(4,4) \end{bmatrix} \tag{B.33}$$

$$\mathbf{C} = \begin{bmatrix} 0 & 0 & 0 & 1 \\ 0 & 0 & 1 & 0 \\ C(3,1) & C(3,2) & C(3,3) & 0 \\ 1 & 0 & 0 & 0 \end{bmatrix} \tag{B.34}$$

Static pressure at station 2 is defined by the following equation:

$$p_{s,2} = p_{t,2} - \frac{\dot{m}_u^2}{2\rho A_c^2} \tag{B.35}$$

Combining B.13 and B.35 and linearizing yields:

$$C(3,1) = \frac{\partial p_{s,2}}{\partial \dot{m}_d} = \frac{A_c}{L_u \cdot \bar{\pi}_c^2 \cdot f\left(\bar{M}_{th}, \gamma\right)} \left[\left(-\frac{\bar{\dot{m}}_u}{\frac{d\dot{m}_{inj}}{d\Delta p_s}} + \frac{\bar{\dot{m}}_d}{\frac{d\dot{m}_{inj}}{d\Delta p_s}} - \bar{p}_{fp} \right) \cdot \frac{d\pi_c}{dm_{u,corr}} \cdot \frac{\sqrt{\bar{T}_{amb}}}{\sqrt{T_{std}}} \cdot \frac{P_{std}}{\bar{P}_{amb}} \right] -$$

$$\frac{A_c}{\bar{\pi}_c \cdot f\left(\bar{M}_{th}, \gamma\right) \frac{d\dot{m}_{inj}}{d\Delta p_s}} - \frac{\bar{\dot{m}}_u}{\rho A_c^2} \tag{B.36}$$

$$C(3,2) = \frac{\partial p_{s,2}}{\partial \dot{m}_d} - \frac{1}{\overline{\pi}_c \cdot f\left(\overline{M}_{th}, \gamma\right) \frac{d\dot{m}_{inj}}{d\Delta p_s}} \tag{B.37}$$

$$C(3,3) = \frac{\partial p_{s,2}}{\partial \dot{m}_d} \frac{1}{\overline{\pi}_c \cdot f\left(\overline{M}_{th}, \gamma\right)} \tag{B.38}$$

$$\mathbf{D} = \begin{bmatrix} 0 & 1 \\ 0 & 0 \\ 0 & 0 \\ 0 & 0 \end{bmatrix} \tag{B.39}$$

Note that in the linearization, certain functional relationships were omitted for simplicity, particularly relationships dependent upon temperature variations. T_b fluctuations were assumed to be of longer time scale than plenum pressure disturbances, so they were neglected. $T_{t,3}$ variation with operating point was also omitted. Evaluating its effect on T_b would require a model of plenum heat release, a level of detail deemed unnecessary for this study.

The linear model examines state variable perturbations around an engine operating point. After an inlet mass flow is chosen, mean engine performance, pressures, and temperatures are evaluated for use in the partial derivatives of the state-space matrices. A compressor speedline is used to determine π_c and the characteristic slope for a given mass flow. For calculations in this thesis, the fit of the 95% $N_{1,corr}$ speedline with 2.14% m_{des} injection was utilized. Empirically-based compressor efficiency is then used to determine $T_{t,3}$. Using an effective turbine area from experimental data, P_b, and total mass flow, $T_{t,4}$ is determined from the constant corrected flow relationship of the choked NGVs. p_{fp} is calculated from the injection throttle C_dA, mean injection flow, and the diffuser throat static pressure. These parameters, in addition to several intermediate values, are used to generate the state-space matrices defined above. Frequency response and system eigenvalue information is then evaluated utilizing the linear system functions of Matlab.

Attempts to use engine geometric parameters in the model were unsuccessful in matching the frequency behavior of the engine. Liberally modifying L_u/A_c, L_d/A_c, V_b, V_{fp}, and

C_dA could not match the observed frequencies nor the correct ratio between the two. However, it was decided to tune the computational "geometry" such that the model poles qualitatively resembled the poles of the forced response experimentation in Chapter 4: a lightly damped mild surge pair and a highly damped pair representing the 68 Hz mode. Figure B-2 shows the pole and zero locations for the computational system at the operating point shown in B-3. Note the slightly positive compressor characteristic slope and the nearly unstable mild surge poles. Table B-1 shows a comparison of actual engine geometry and the empirical throttle C_dA to the parameters chosen for the computation. Despite its misses in frequency, the model was capable of examining phase relationships between the various outputs.

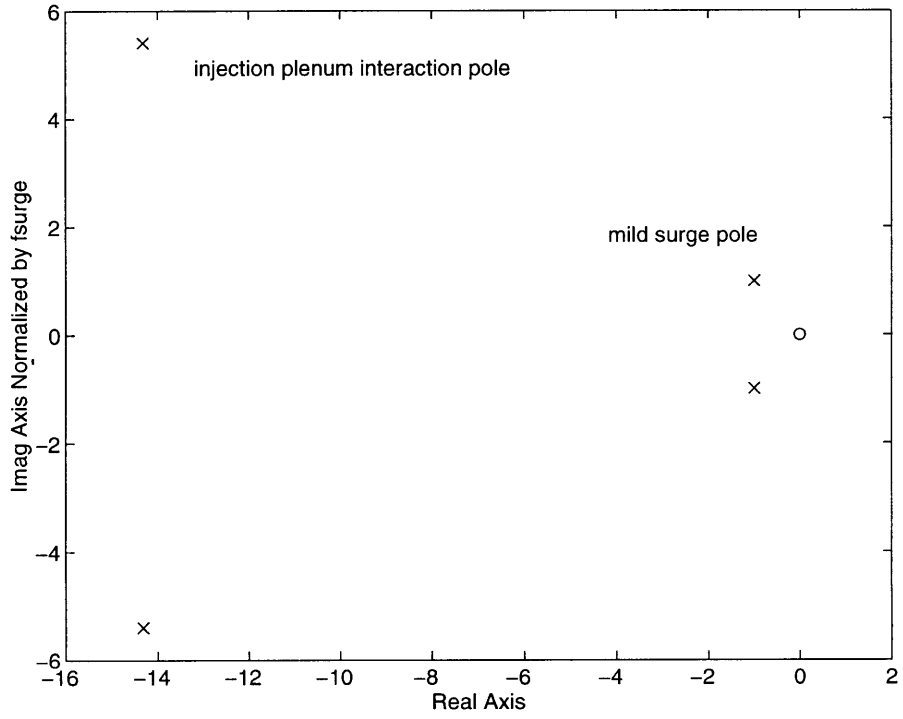

Figure B-2: Pole-zero plot of system with chosen geometric parameters at operating point in Figure B-3

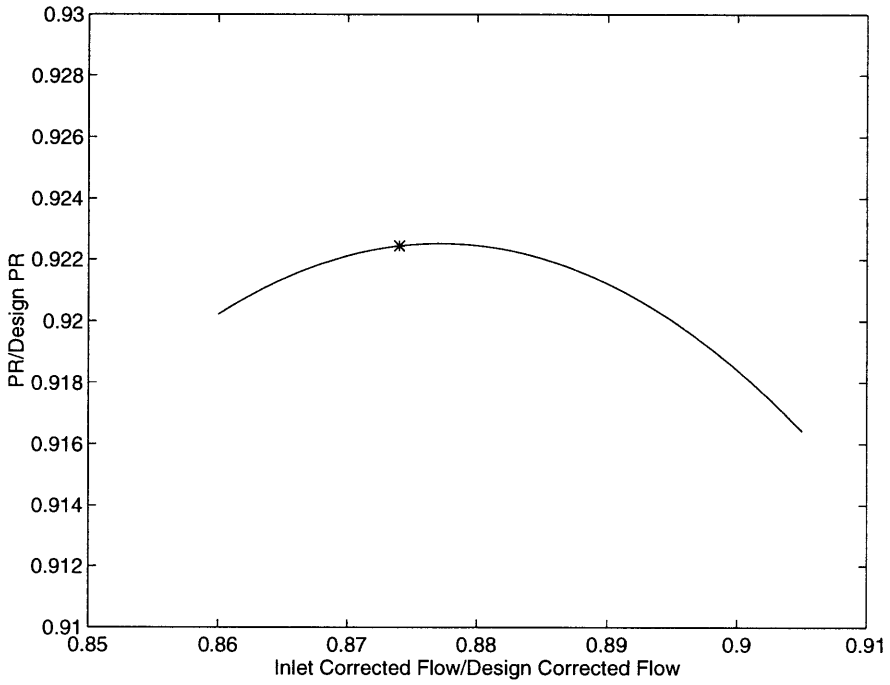

Figure B-3: Operating point used in calculations for Figures 3.32 and 3.33 shown on the 95% $N_{1,corr}$ compressor characteristic fit with 2.14% m_{des} mean injection

Parameter	Geo. or Empirical	Simulation
L_u/A_c	0.544 1/in	1.360 1/in
L_d/A_c	1.245 1/in	3.113 1/in
V_{fp}	18.317 in^3	183.17 in^3
V_b	616 in^3	1540 in^3
C_dA	0.346 in^2	3.46 in^2

Table B-1: Comparison of engine geometry and chosen calculation parameters

The results shown in Figures 3.32 and 3.33 were computed at the operating point indicated in Figure B-3. These results were generated using the transfer functions of output variables to $p_{b,noise}$ forcing. Since the 68 Hz mode was observed in the natural response of the engine, it was hypothesized that the energy supply for the oscillations may originate in the combustion process. m_{valve} forcing was not investigated in this thesis.

The coefficients of the state-space matrices change with operating point. Therefore, the migration of system poles and zeros can be tracked for changes in operating condition.

The results shown in Figure 4.8 show the migration of the poles toward instability as the mass flow decreases along the characteristic in Figure B-3.